# 3D INKJET PRINTING METHOD WITH FREE SPACE DROPLET MERGING FOR LOW VISCOSITY AND HIGHLY REACTIVE MATERIALS

# 3D INKJET PRINTING METHOD WITH FREE SPACE DROPLET MERGING FOR LOW VISCOSITY AND HIGHLY REACTIVE MATERIALS

By

MONIKA SLIWIAK, B. Sc.

A Thesis

Submitted to the School of Graduate Studies

in Partial Fulfillment of the Requirements

for the Degree

of Master of Applied Science

McMaster University

MASTER OF APPLIED SCIENCE (2018) McMaster University

(Mechanical Engineering) Hamilton, Ontario

TITLE: 3D INKJET PRINTING METHOD WITH FREE SPACE DROPLET MERGING FOR LOW VISCOSITY AND HIGHLY REACTIVE MATERIALS

AUTHOR: Monika Sliwiak, B. Sc. (Warsaw University of Technology)

SUPERVISOR: Dr. Ponnambalam (Ravi) Selvaganapathy

NUMBER OF PAGES: XVII, 152

# Abstract

Silicones are industrially important polymers characterized by a wide spectrum of chemical and physical properties with a number of important applications including automotive components, construction materials, isolating parts in electronic devices, flexible electronics, and medical products. Development of additive manufacturing methods for silicones enable production of complex and custom designed shapes and structures at both the micro- and macro-scale, economically feasible. In general, such materials can be fabricated using stereolithographic, extrusion-based, or inkjet printing techniques, in which silicones are polymerized using either photo- or heat-initiators. Silicones can also be crosslinked based on chemical reactions. Although this approach is supposedly the simplest, it has not been widely applied in additive manufacturing, as suitable technology for mixing and curing reactive inks without clogging nozzles has not be developed yet. To address this issue, a new 3D printer, that enables the fabrication of highly reactive and low viscous materials, has been developed and tested experimentally.

The proposed fabrication method involves the ejection of two reactive droplets simultaneously from individual dispensers, merging and mixing them in free space outside the nozzle followed by deposition of the merged drop in a patterned format on a substrate. It was shown that the printing process is robust and stable more than 4 hours and it can be used on demand. By incorporating an XYZ positioner, it was possible to deposit droplets in an overlapping fashion to print any programmable shape featuring homogeneous structure, with a small number of pores. Moreover, due to the almost instantaneous reaction between two components ($< 10$s), the fabrication of very high aspect ratio (AR $> 50$) objects is possible. Lastly, the presented method can be easily adapted to print in free space without the use of

support materials.

# Acknowledgments

Undoubtedly, my journey as a master's student at McMaster University belongs to one of the most fruitful chapters of my life. I spent countless hours with my fellow students and faculty members on casual conversations and scientific deliberations, thanks to which I learned not only how to be a good researcher, but, most importantly, how to become a better person.

First of all, I want to express my sincere gratitude to my supervisor, Dr. P. Ravi Selvaganapathy, for his trust and giving me the opportunity to work in his research group on very exciting problems. Thanks to his help and guidance, I was able to consider nonintuitive solutions and implement innovative ideas in my experiments, which significantly improved the quality of my thesis. Again, I very grateful to Dr. Ravi for all his efforts in mentoring me in my scientific endeavors.

Secondly, I would like to thank Dr. Michael A. Brook and his student Robert Bui, who with their great knowledge about silicones, contributed to the progress of this project. Without their support on the material side, I would not be able to obtain the significant results in my experiments.

Thirdly, I would like to thank those who contributed to the successful completion of my experiments. In particular, I am grateful to Dr. Chan Y. Ching and Dr. David Nakhla, who made the high-speed camera available, and offered their help in teaching me how to use it. If it had not been for them, the beautiful pictures of droplets would have never been taken. I am also grateful to Dr. Shiping Zhu and Dr. Darko Ljubic, who taught me how to measure the rheological properties of different materials. Many thanks go to the students and researchers from the Center for Advanced Micro-Electro-Fluidics who always supported me, inspired me to explore challenging ideas. I will never forget the friendly atmosphere in the lab-

oratory, where I could fulfill my passion.

Finally, I am very grateful to my parents, sister and in particular, to my dear husband, Adam Sliwiak. He encouraged me to fulfill the dream of studying at McMaster University and never allowed me to doubt my talent. I would like to thank Adam for his love, support, and patience. Without him, I would not be where I am.

# Contents

# List of Figures

# List of Tables

# 1 Motivation and Chapter Organization

## 1.1 Motivation

Silicones feature an exceptional range of chemical and physical properties, in particular, biocompatibility, flexibility, and resistance to moisture, chemicals, heat, cold, and ultraviolet radiation. Therefore, they are applicable in a number of different applications such as automotive and aviation components, isolating materials in electronic devices, flexible electronics, solar panels, medical products, membranes and microfluidic devices, and many more. A number of techniques exist for the manufacture of silicone objects, such as extrusion, injection molding or compression molding. However, these methods are suited for mass production and newer Additive Manufacturing (AM) techniques, have been developed to enable rapid and precise fabrication of custom designed parts and objects in silicone. There are essentially three popular methods of AM suitable for silicones, namely the stereolithography, extrusion-based and inkjet printing. They all differ in terms of the resolution and size of the fabricated objects. Despite the difference, all of them are suited for the same polymerization approach, in which two silicone components react together under the influence of either UV-radiation or elevated temperature. However, the light and heat sources make the fabrication process more complex and increase the cost of the device. On the other hand, the cross-linking using chemical initiators is simple, does not require additional equipment and can be cost effective. This approach, however, has not been widely implemented in the 3D printing, as the instant polymerization upon mixing leads to the problem of the printhead clogging, which is unavoidable if highly reactive materials are used. The work presented in this thesis is an attempt to address this challenge by proposing the first efficient

3D printer for highly reactive and low viscous materials. The fabrication is based on the simultaneous generation of two drops made of different substances from two independent dispensers, merging them in free space outside the nozzles and depositing them on a substrate in a patterned format. The proposed printhead does not clog, and, moreover, it guarantees continuous and stable printing over several hours, with multiple start-stop cycles.

## 1.2 Sequence of Chapters

The thesis is divided into six chapters. The first one includes the motivation of the research, as well as brief descriptions of all the remaining chapters.

Chapter 2 introduces silicone materials, their properties, applications and polymerization approaches. Additionally, it outlines all of the popular Additive Manufacturing techniques and reviews in detail those used for the fabrication of silicones.

Chapter 3 presents the new 3D inkjet printer design with an integrated free space mixing module. In particular, it provides a detailed description of the printhead design. Next, it details the specifications of the proposed printing method and utilized materials. The methods used for the optical measurement, positioner calibration, and other experimental details are discussed.

Chapter 4 describes the characterization of the printhead. It discusses the critical printing parameters that control the droplet ejection phenomenon, which are carefully analyzed and compared with theoretical results. The chapter also focuses on the droplet coalescence in free space and characterizes this phenomenon for the inks used in this thesis. Finally, the capabilities of the proposed method are presented.

Chapter 5 shows various applications of the designed 3D printer. Different examples of printed objects, starting from a one-dimensional dot, through two-dimensional structures, to three-dimensional parts are demonstrated. Moreover, the analysis of

the results, as well as the calibration and optimization of the printing process, is described in detail. Lastly, the capabilities of free space printing are described.

Chapter 6 provides the conclusion of this thesis and summarizes the key findings of the thesis. It describes the major contribution that this this made to the body of knowledge in 3D printing. It also discusses potential future directions that this research could take.

# 2 Introduction

## 2.1 Silicone

After oxygen, silicon is the second most abundant element in Earth's crust and accounts for around 25 percent of its total mass. Nevertheless, its pure form can very rarely be found in the nature. On the other hand, the oxidized forms, such as silicon dioxide or silicates, are plentiful in sand, clay, and many other places on the Earth. In 1824, Jons Jacob Berzelius managed to isolate pure silicon and, thanks to this spectacular breakthrough in the chemistry the pure silicon has become the essential component of inorganic materials.

The term "silicone" was coined by F. S. Kipping in 1901 to describe a substance that contains silicon atoms together with oxygen, carbon, hydrogen, and other elements. However, the actual "silicone revolution", that initiated the global boom in the industrial manufacturing, happened a few decades later. In 1941, two professors, Muller and Rochow, independently discovered a reaction of silicon and methyl chloride, whose products are silanes. Silanes are inorganic compounds which are core building blocks of silicones. Thus, silicones, also known to chemists as polysiloxanes, consist of an inorganic backbone made of alternating silicon and oxygen atoms. The remaining bonds of tetravalent silicon are attached to the organic group such as an alkyl (methyl, ethyl) or phenyl group. The most common polysiloxane is linear polydimethylsiloxane (PDMS), whose chemical structure is illustrated in Figure 2.1.

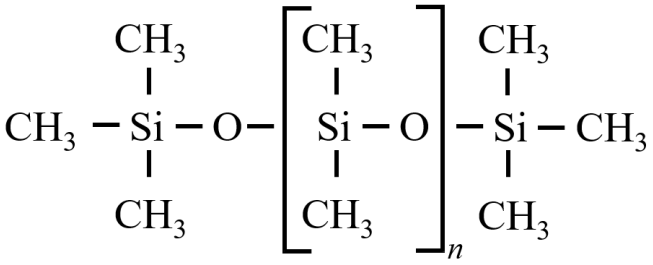

Figure 2.1: PDMS molecular structure in which n is a number of repeating monomer [SiO$(CH_3)_2$] unit.

The backbone of PDMS (as well as other silicones), built from Si-O bones, is very strong and stable. Thanks to these properties, silicones feature remarkable resistance to a variety of physical influences. For example, silicones remain stable and flexible in a low (-$50^0$) as well as in high ($300^0$) temperature. They are not sensitive to the variations in the oxygen content, ultraviolet light intensity, particle radiation intensity, and many other chemical, microbial, and electromagnetic factors. Additionally, they feature low thermal conductivity, low toxicity, and high gas permeability. What is more, a proper selection of different functional organic groups attached to the Si bonds enables the incorporation of modifications. Its consistency can vary from liquid, to gel, rubber, or even hard plastic. Therefore, it is possible to modify its state of matter and toughness, according to one's needs.

Thanks to the variations in PDMS structure and its properties, one can find diverse applications of silicones. Due to their universality, they are an integral part of things that we use in our every day life. For example, the liquid form of a silicone is usually added to shampoo to give hair a shine. They are also basic ingredients of many detergents for washing machines, since they reduce foaming and secure smooth surfaces of textiles. The painting emulsion prepared based on silicone resin is water repellent and permeable to oxygen and carbon dioxide. Silicone rubber is used as an isolating material in electronic devices, but also to protect them against

moisture and dirt. Moreover, due to the biocompatibility of many silicones, they can be utilized to manufacture different medical products, such as breast implants, testicle implants, contact lenses, and catheters [1, 2] or cell culture scaffolds [3, 4]. What is more, PDMS is widely used in different subfields of mechanical engineering. Nowadays, scientists are able to make sophisticated microfluidic devices [5], since PDMS perfectly replicates any shape. Others try to fabricate highly stretchable and elastic electronical components [6, 7, 8], or highly permeable sponges and membranes [9, 10]. It seems that the list of application of silicones is unlimited. In general, one can find them in the following sectors: automotive and transport, construction, textiles, leather and fiber, paper and film coatings, life science, elastomers, plastics and composites, coatings and adhesives, electrics and electronic and in chemical industry.

Although there exists a plethora of types of silicones, only elastomers will be considered in this thesis, since they are critical in the 3D printing technology. They consist of long chains of polysiloxanes and crosslinker. During the curing process between those components the strong covalent bonds are created which leads to an irregular three-dimensional chemical structure of a silicone elastomer. Such a silicone can be categorized according to the chosen curing method, curing temperature, and viscosity of components. At a sufficiently high temperature liquid silicone rubbers can be polymerized. They consist of two components, first of them contains a platinum (Pt) catalyst, while the second involves an additional functional curing agent. Due to the relatively low viscosity of the both components in the room temperature, they are free-flowing and can be mixed in different mass ratios which can be used to modify the stiffness of the cured product. It should be emphasized that the uncured-polymer can perfectly fill any mold shape and form to the topography of the mold. The PDMS curing process starts at an elevated temperature and it

does not release any by-products. In the room temperature, however, it is possible to polymerise only liquid silicones, which may consist of a single or two components. In the case of a two-component silicone, the polymerization process can be initiated either chemically or by UV-light. The radical reaction is enabled because one of the components contains a catalyst such as platinum, which does not generate any by-products, or organotin compounds, which leads to the production of alcohol. The total time of the curing process is fully controllable by the radiation intensity and exposure time. The chemically-driven process, on the other hand, does not require any catalysts. When a curing process is initiated chemically, two substrates can react upon mixing, whereas if a one-component silicone is used, the polymerisation is initiated by simple exposure to humidity air. The curing process begins on the outer surface of the deposited silicone and gradually expands towards its center. During the whole process, depending on the amount and type of the used curing agent, different by-products, such as acetic acid, amine, and alcohol, small volume are produced.

Silicone elastomers can be fabricated using various methods, namely extrusion, injection molding, liquid injection molding, compression molding, calendering, and transfer molding. The listed techniques differ in terms of the resolution tolerance of the created part, its dimension, material, and operating parameters. Despite these differences, they feature a few common characteristics. Each of them can be adapted to the mass production which reduces the cost per a manufactured piece. They require special tools, for example a mold, which needs to be changed every time with any change of the fabricated element. Additionally, the machines are expensive, large and require highly qualified workers. Fortunately, to address all these problems, one could consider Additive Manufacturing (AM) methods, which is the focus of the next section.

## 2.2 Additive Manufacturing

Additive Manufacturing (AM) is a term that describes a family of technologies that enable the fabrication of three-dimensional complex objects. These techniques use CAD (Computer Aided Design) software, which facilitates the generation, modification, and optimization of the design of an object, which is then built using a layer-upon-layer approach. Although it is a relatively new method (it was invented in 1980s), it belongs to the one of the fastest growing branches of the manufacturing industry. Compared to other well-known manufacturing techniques, AM features a few unique advantages. First, it enables printing of objects with complex designs and shapes that cannot be constructed by conventional machining. Moreover, since AM does not require additional tooling, it reduces the total time of the product development, from an engineering concept to manufacturing. Therefore, it can be easily customized to individual requirements which is especially important in the medical sector as well as in the prototyping process. Furthermore, cost for fabrication using AM is increasingly affordable for individual customers in terms of the cost. AM-based manufacturing methods have recently become more popular in many fields and, therefore, it is predicted that in 2020 the production and service of AM will exceed 20 billion of U.S Dollars [11]. To achieve such a large market value, AM must be gradually developed incorporating the advanced technology for a wider spectrum of materials. One can distinguish seven categories of the additive manufacturing, namely, powder bed fusion [12], direct energy deposition, sheet lamination, material extrusion, binder jetting, vat photopolymerization, and material jetting.

### 2.2.1 Powder Bed Fusion

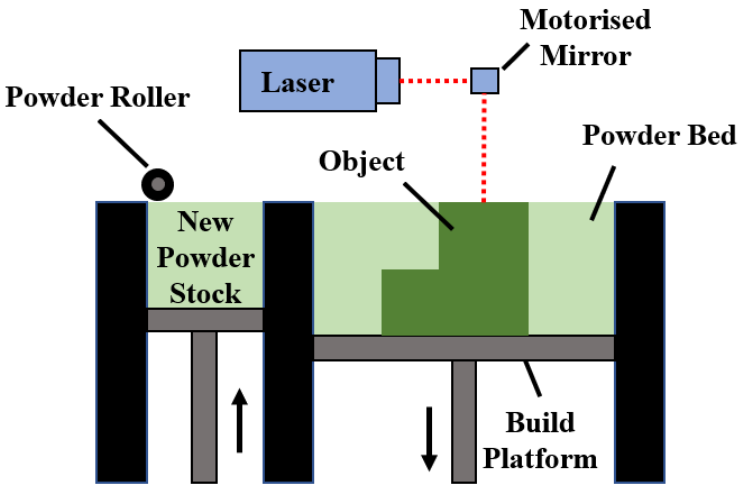


Figure 2.2: Schematic diagram depicting the powder bed fusion technology.

In the powder bed fusion, depicted in Figure 2.2, plastic, metal, ceramic, or glass powder is spread uniformly over the build plate using a roller or blade mechanism. The minimum thickness of the layer can be as small as 20 $\mu$m [13]. Subsequently, some of the particles are melted and fused together under the influence of the laser or electron beam energy. The heat source scans the cross-sectional pattern created in the CAD software and follows it on the powder surface. After each fusion operation, another layer of powder is applied on the top surface, and then the process is being repeated until the desired 3D structure is created. For the process to continue, the temperature is required to exceed the melting point and, to reduce the printing time, the material gathered in the powder bed is preheated slightly below the melting temperature. Clearly, this operation increases the power and time consumption. On the other hand, the powder bed fusion method does not require additional support materials because the created part is always surrounded by unsintered powder. The

above approach allows to print complicated but not hollow parts, since the support material inside the 3D object has to be removed. The powder bed fusion methods can be further divided into many subgroups such as selective laser sintering (SLS), selective laser melting (SLM), direct metal laser sintering (DMLS), direct metal laser melting (DMLM), and electron beam melting (EBM) [14].

### 2.2.2 Directed Energy Deposition

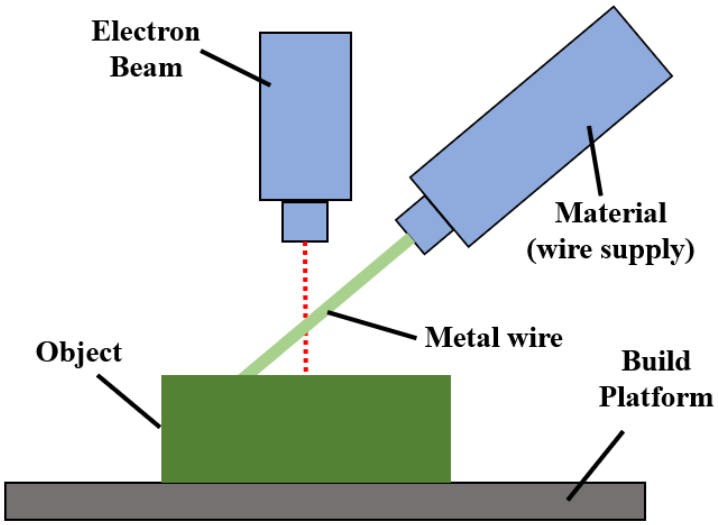


Figure 2.3: Schematic diagram depicting the direct energy deposition technology.

The direct energy deposition (DED) method is designed for polymers, ceramics, and metals. As shown in Figure 2.3, the heating source, which might be a laser, electron beam, or plasma arc, heats and melts a substrate on which an object is printed and it simultaneously melts the deposited material. Subsequently, the printed part solidifies leading to a three-dimensional object featuring strong bonding between its subsequent layers. The material used in DED appears in two forms, namely, in the form a wire, which does not generate material waste, and powder, that guarantees better accuracy. Usually the printing accuracy of a layer thickness ranges from 250

$\mu$m to 500 $\mu$m [14] which leads to some limitations. DED-based methods are not designed to create completely new parts but rather to repair or augment existing objects. Nevertheless, one of its biggest advantages is the possibility to utilize multi-axial nozzles which can move along four or five axes, but also it is proven to work in the case of very complex geometries.

One can further distinguish different subgroups of this method: Laser Engineered Net Shaping (LENS), Directed Light Fabrication (DLF), Direct Metal Deposition (DMD), 3D Laser Cladding, Laser Generation, Laser-Based Metal Deposition (LBMD), Laser Freeform Fabrication (LFF), Laser Direct Casting, LaserCast, Laser Consolidation, LasForm, and others [14].

### 2.2.3 Sheet Lamination

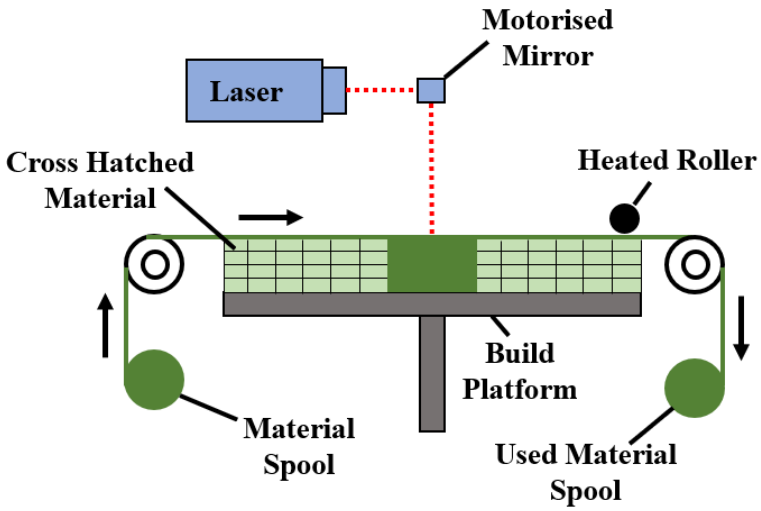


Figure 2.4: Schematic diagram depicting the sheet lamination technology.

Historically, the first developed technique in the family of Sheet Lamination Methods is Laminated Object Manufacturing (LOM), which is illustrated in Figure 2.4. It is based on the lamination of paper sheets where each sheet constitutes one cross-

sectional layer of the manufactured object. Subsequently, after a few laminations cycles the sheets are cut using a laser, and then the procedure is repeated until the desired shape is obtained. Due to the limitation of the cutting tools, only the outer contours can be controlled. Among LOM-based approaches, one can distinguish two different working procedures, first, involving lamination of the sheets and then cutting them or, second, in which cutting precedes the lamination [15]. In addition, over the last couple of decades, different alternative fabrication methods, such as gluing or adhesive bonding, thermal bonding, clamping, ultrasonic welding, as well as the cutting operations have been developed [14]. Nowadays, however, Ultrasonic Additive Manufacturing (UAM) is the most popular. In UAM, two layers of metal foil, featuring a thickness in the range from 100 $\mu$m to 150 $\mu$m [14], made of aluminium, copper, stainless steel, or titanium, are bound together thanks to the normal forces coming from a rotating sonotrode, which generates a uniform oscillation with the frequency of 20 $kHz$ transversely to motion. Subsequently, CNC milling is utilized to form the required shape of the object. The cutting process can be applied after each cross-sectional layer or at the end of the whole procedure and it depends on the design complexity. Additionally, the CNC milling head features more degrees of freedom than the laser, which means it can operate in different planes. UAM-based approaches feature many advantages, for example, they are usually faster than the other methods, especially with respect to the deposition time of a material layer. What is more, the low-temperature ultrasonic bonding with additive and subtractive processing enable the fabrication of complex multi-material components. Moreover, UAM's dimensional accuracy is dependent only on the CNC machining precision and not on the foil nor layer thickness, which is the case in other methods. However, among a few disadvantages of UAM, one could emphasize the shortage of support materials.

### 2.2.4 Material Extrusion

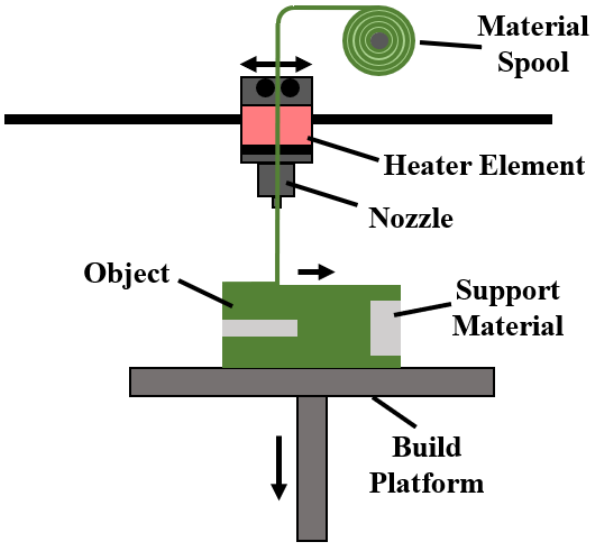


Figure 2.5: Schematic diagram depicting the material extrusion technology.

Extrusion-based methods are currently the most widely used method of AM. In this method, whose working principle is sketched in Figure 2.5, a material, such as a thermoplastic and amorphous polymer, is extruded via a feed system into a compact portable chamber. In the chamber, the material is heated and pushed out of the nozzle due to the constant inner pressure, which guarantees a uniform cross-sectional area of the extruded filament. The accuracy of this technique depends on the diameter of the nozzle and, to a lesser extent, on the speed of nozzle movement. The structure is built in the layer-by-layer manner. The main requirement of this method is that the material leaving the nozzle must be in the semi-solid state, but when deposited on the platform it must be bound to the previously printed material and then fully solidify to obtain the required shape. There exist essentially two approaches which allow to achieve this goal. First of them is based on the temperature control of the state of matter. One of the best examples of this approach

is the fused deposition modeling (FDM). The second method, on the other hand, relies on chemical reactions in which a highly viscous liquid after the deposition solidify as the result of the reaction with a curing agent, residual solvent, moisture, or because of drying. Among the advantages of the extrusion-based techniques are: low cost of printing, a wide range of thermoplastic and polymeric materials, possibility to use support materials. However, among its drawbacks one could emphasize the limitation of the nozzle diameter, which imposes limits on the method accuracy and thus the quality of the product. The resolution is determined by the layer thickness which varies from 0.178 mm to 0.356 mm [16], but under special conditions it can achieve 140 $\mu$m [17]. Moreover, this method requires a precise feeding system in order to secure a constant pressure.

### 2.2.5 Binder Jetting

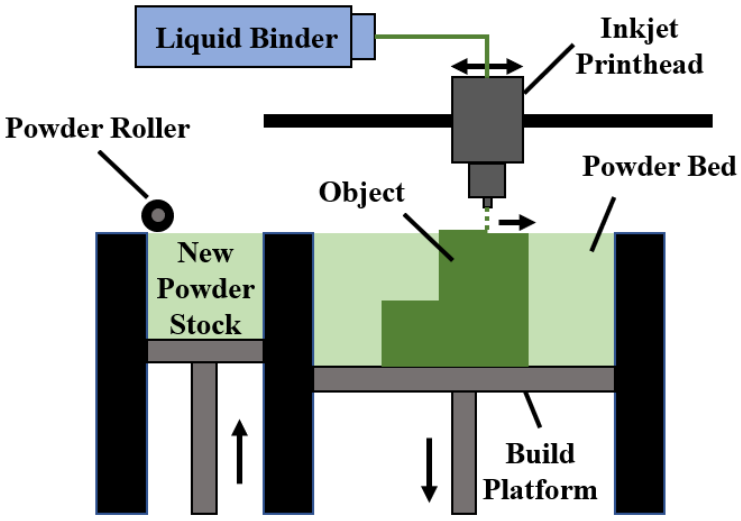


Figure 2.6: Schematic diagram depicting the binder jetting technology.

In a binder jetting (BJ) method, which is illustrated in Figure 2.6, two materials are used, powder and binder. The latter acts as an adhesive between powder particles

and, therefore, it is similar is some way to powder bed fusion method in which laser melts the powder particles. The binder droplets, typically featuring a diameter of 80 $\mu$m [14], are generated on the top of a powder bed by a multi-nozzle print head, whereas the powder of metals or ceramics is spread on the bed by a rolling mechanism. Hence, both the components are deposited using a very fast approach. BJ method enable the printing of complex shapes, since the powder itself is an ingredient of the built object, it also acts as a support material. In addition to that, thanks to the fact that one can combine different kinds of materials such as metals, ceramics, and polymers, BJ methods allow us to print materially inhomogeneous objects. Nevertheless, at the end of the printing process the post-processing is necessary, which extends the fabrication time. At the post-processing stage, the unbound powder is removed using pressurized air and then the part is cooled to fully solidify and achieve desired mechanical properties.

### 2.2.6 VAT Photopolymerisation

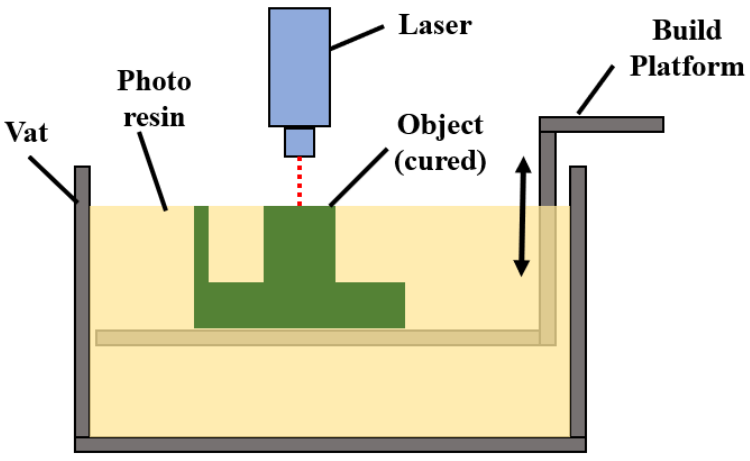


Figure 2.7: Schematic diagram depicting the vat photopolymerisation technology.

Methods based on photopolymerization enable fabrication of objects made of photocurable resins, which are chemically excited by a radiation source. Indeed, there exist a few different sources of radiation, including gamma rays, X-rays, electron beams, UV, and visible light, of which the last two are the most popular. As illustrated in Figure 2.7, the object is built in a layer-by-layer fashion, where the cured part is immersed in or ascends from a container of photosensitive liquid, whose thickness is the same as a single layer of the printed part. As a consequence of the exposure to the high energy light, a new layer of liquid chemically reacts and solidifies. The parts fabricated using this method feature high resolution, due to the capabilities of the illumination technology used. One can categorize then into three types, namely: the vector scan, mask projection, and two-photon approaches. The vector scan enables point-wise exposure and its resolution depends on spot size of the illumination beam. Its diameter typically reaches the value of 150 $\mu$m [18], but in the micro vector scan technique it can be reduced to 10 $\mu$m [19]. In the mask projection technique, the modulator chips generate a dynamic photomask on a material surface and, simultaneously, polymerizes it. Undoubtedly, the speed of this method is its main advantage, and the accuracy of printed objects varies dependently on the illumination system. In specific cases, thanks to this method, it is possible to generate pixels with the diameter lower that 10 $\mu$m [14, 20], but for typical printer, however, its values ranges between 80 $\mu$m and 140 $\mu$m in the standard fabrication [14], and between 40 $\mu$m and 70 $\mu$m in the high-resolution mode [14]. The third process, called two-photon vat photopolymerization (2p-VP), is also a point-wise exposure method and is designed such that it allows cure of only those molecules which are struck simultaneously by two photons with high energy. Two beams of light at an angle are used and the core of intersection point is where the intensities are high enough that two photon polymerizations can occur. This re-

quirement increases the resolution of this method to about 100 nm [21]. Depending on the choice of scanning techniques and light system, one can distinguish essentially five different vat photopolymerisation methods, Stereolithography (SL, SLA) [22], which is the most popular, Digital Light Processing (DLP) [23], Scan, Spin and Selectively Photocure (3SP), Continuous Light Interface Process (CLIP) [24], Digital Light Synthesis (DLS) [25]. Regardless of the particular choice, the fabricated object requires post processing.

### 2.2.7 Material Jetting

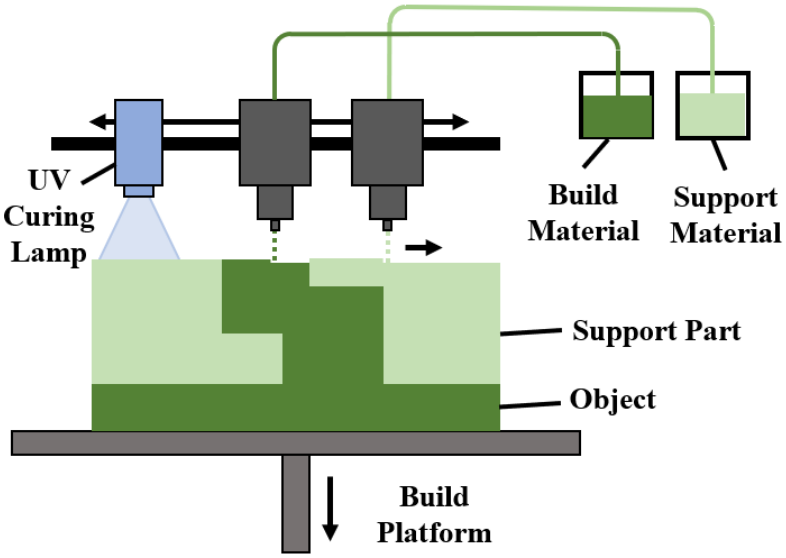


Figure 2.8: Schematic diagram depicting the material jetting technology.

Material jetting is very similar to the 2D ink jet printing and its working principle is visualized in Figure 2.8. The droplets of a material are ejected from a printhead at specific locations on the print bed where they solidify in order to build one layer of a 3D structure. Subsequently, another layer is deposited on the top of it and the 3D object is fabricated in the layer-by-layer manner. There are two techniques to eject a material, using either the continuous (CIJ) or Drop-on-Demand (DOD) approach

[26]. In the CIJ system, the droplets are formed by an ultrasonic vibrated nozzle and deposited using either a charged deflection platform, when printing conductive materials, or air current flow, when the material is uncharged. In this method, a material is constantly being ejected and, therefore, the unused droplets are recycled back to the system and used in the consecutive process. In contrast to the continuous printing approach, in the DOD system the ejection occurs only when needed. The drop is produced in response to the time-dependent pressure pulses generated by actuation mechanisms inside dispenser's chamber. One can distinguish four actuation methods: thermal, piezoelectric, electrostatic, and acoustic. Nevertheless, most of modern printers are designed based on the first two of them. The DOD-based methods impose limitations on the choice of a material, in terms of viscosity and ability to form a drop (which is depends on the surface tension). Therefore, few types of polymers, wax, or plastic can be applied. In general, using material jetting methods one can create object featuring high dimensional accuracy and a very smooth surface finish. The typical thickness of a layer varies between 16 $\mu$m and 32 $\mu$m, while the dimension accuracy is around 100 $\mu$m [27], however, in some particular cases, can be reduced to even to 0.7 $\mu$m [28].

In summary, additive manufacturing is a rapidly emerging area in manufacturing that consists of many techniques dedicated to different types of materials and resolution requirements. Nevertheless, only three of the main methods, namely vat polymerisation, material extrusion and jetting, are typically used the fabrication process of silicones.

## 2.3 3D printing methods for silicones

Silicones are industrially important polymers due to the broad spectrum of physical and chemical properties, and, thanks to suitable 3D printing methods, they can be used to fabricate objects of arbitrary shapes in a quick manner. Although there essentially exist seven main categories of additive manufacturing, only three of them, namely the extrusion, jetting, and vat polymerisation can be deployed in silicone fabrication process.

### 2.3.1 Extrusion-base methods used in silicone printing

The extrusion method is the most popular, as it can be applied to a wide range of thermoplastic, elastomeric, and other types of materials that can be pushed through a nozzle. Among the most popular extrusion materials are ABS (Acrylonitrile butadiene styrene) and PLA (Polylactic acid), however, there also exist other materials, featuring completely different physical properties, such as cement [29], chocolate [30], and silicones. Extrusion printing of silicones can be further categorized into three groups, depending on the used initiator, which directly affects the chemical reaction between the reactants and therefore, determines the type of an extrusion printing technique.

#### 2.3.1.1 Chemically initiated one-component silicone resin

Silicone curing can be initiated using moisture in the environment as a curing agent [31]. In this method, the silicone pre-polymer is pumped through the print head and deposited on the platform in patterned format using the direct writing method. As only a one-component substance with constant physical properties is used, the printing process requires a simple calibration process at the very beginning of the

printing process. Once the flow rate of the material is properly adjusted to the feed rate (which can be intuitively understood as speed) of the printer, these values remain unchanged during the whole fabrication process. After the deposition stage, the material cures beginning from the outside layers, which have direct contact with air, to the center. The curing process is long, it usually takes a few hours, and, therefore, it requires materials with certain properties. The most important of them is viscosity because the extruded silicone must maintain the required shape before and during the polymerization. The value of the dynamic viscosity should be sufficiently large, usually of the order of a few Pa·s, therefore it is a highly viscous material compared to water. Using this type of materials also has some limitations. A more viscous liquid requires a greater extrusion pressure and/or larger diameter of a nozzle. Therefore, it is difficult to achieve a high-resolution of printing. Moreover, due to the high viscosity, consecutive layers retain their extruded cylindrical shape that can cause additional rough surface structures. What is more, printing tall objects, made of a several layers, in combination with the extended curing time causes compression and small deformation of the lower layers. Therefore, the dimension of the printed object in the vertical direction can be affected. In conclusion, the main drawback of the described method for moisture-cured silicones is poor resolution. Nonetheless, it does not require additional equipment for initializing the chemical reactions, and, neglecting the vulcanization time, the method is fast compared to other AM methods.

#### 2.3.1.2 Chemically initiated two-component silicone resin

It is also possible to fabricate a 3D object made of a two-component silicone resin with a chemically initiated reaction. One of the components is placed in a bath, while the other one is extruded into the former through a nozzle [32]. The substance in a

bath should be highly viscous and remain in the gel state because it cannot deform during the movement of the positioner. Moreover, it ensures that the extruded substance remains in the required position and, therefore, the gel is used as a support material. The viscosity of the extruded component is less important in the deposition process, however the lower values guarantee better resolution. Because the nozzle is submerged in the gel during the whole printing process, the polymerisation reaction must be very slow; it typically takes hours or even days to complete the solidification. Thanks to the slow pace of this chemical phenomenon, the polymerization does not affect the nozzle dimension and, therefore, both the diameter of the extruded material and feed rate remain constant. Although the curing process is independent on the external source, one can use an ultrasonic device to excite local mixing of the component. Once the vulcanization process is finished, the object is taken out from the bath, while in the post processing stage the gel is removed.

#### 2.3.1.3 Thermally initiated silicone resin

Another group of silicones can be crosslinked using a heat initiator. From the additive manufacturing perspective, those materials are very challenging because silicones are thermal insulators. Thus, a traditional 3D printer with a heat source in the print bed, is not sufficient. Therefore, a thermally-initiated silicone is printed in a bath filled with the support material, through which the heat is transferred [17]. The support material features a gel-like consistency and, during the printing process, it behaves like Bingham plastic which enables unconstrained movement of the nozzle. The gel, however, acts as a solid for the material extruded in which completely blocks its movement. It is important to note that the gel should be hydrophilic to eliminate any miscibility with a hydrophobic silicone. The chosen silicone consists of two components, which start to cure at an elevated temperature.

Therefore, at the room temperature they can be premixed and extruded together from the nozzle as a liquid material. What is more, due to the presence of the support gel, one can decrease the viscosity of the silicone and achieve higher resolution. The method of providing heat can be in two distinct ways. In the first approach, the heat source is turned on once the printing process is finished and, in the second, elevated temperature is maintained during the extrusion. In the latter there is a possibility that the nozzle will be clogged which will eventually stop the printing process. Thus, the choice of a method depends on the time the nozzle remains in the gel. If the time is relatively short, either approach can be chosen. However, if the printing process is long, the first solution is preferred. The vulcanization process can take even up to 72h because for such period of time the gel structure remains unchanged. Subsequently, the support gel is dissolved using phosphate buffered saline solution and, finally, the printed element is released. As mentioned above, the two components of PDMS can be premixed and poured in the printer tank as a single component or, alternatively, they might be delivered separately to a specially designed print head [33]. In the print head there is a T-junction connector to which the two substances, controlled independently by two pumps, flow from both the left- and right-hand side. Subsequently, the materials are mixed together in a planetary centrifugal mixer and extruded through the nozzle. Depending on the flow rate of each component, their volumetric ratio can be changed and, therefore, one can obtain the final product with different rheological properties.

#### 2.3.1.4 UV curable silicone resin

The last group of liquid silicone rubbers, that will be considered in this thesis, are radical-cured materials. The most popular radical source in the extrusion type of printing is UV light [34, 35]. UV sources are usually utilized in two situations, first,

when the fabrication is in progress and, second, at the very end of the process, in the post processing stage. In the first case, the UV initially polymerizes a silicone to prevent it from extensive spreading, but also to enable the deposition of another layer on top of it without causing unwanted deformation. Usually the time of exposure to UV during the process is significantly shorter compared to the one in the post processing stage. During the fabrication, the light can be turned on after each layer once the print head moves to a safe and shadowed position to avoid the nozzle clogging problem which in result elongates the total fabrication time. However, the silicone can be irradiated during its deposition provided the light source is placed within a suitable distance from a properly protected nozzle. The curing process of this silicone depends on the properties of resin, for example, on monomer reactivity, optical absorbance, and photochemical efficiency, and on the exposure time and UV intensity. Controlling the UV light parameters, one can obtain an object in either a gel or solid state. Moreover, high intensity of the UV light leads to decrease of the curing time. Hence, one could utilize a low viscous silicone to improve the accuracy. The roughness of a printed surface is also controllable by UV parameters. By setting appropriate UV intensity, one can calibrate the polymerization time such that the consecutive layers of the material overlap uniformly. Apart from the option of building an object in free space, there is a possibility to print it inside a shear thinning support material in a bath [36]. The support material, however, must be transparent with respect to the UV light, which is exposed after the extrusion process. Moreover, its yield stress should be easily reduced under the influence of an aqueous solvent. In extrusion-based printing, two components of a photoinitiated silicone can be premixed and printed from a single nozzle provided the tank is appropriately protected against the light source. Alternatively, a print head with an integrated mixer also can be applied.

It should be noted that both thermally- and radical-initiated silicones fabricated in an extrusion-based 3D printer require additional components, such as heat and UV light generators. Therefore, compared to printing methods for chemically crosslinked materials, these systems are more expensive and slightly more complicated.

#### 2.3.1.5 Systems regulating flow rate in extrusion printing

Extrusion-based printing methods for silicones can be categorized with respect to either the material type, which was described above, or the kind of a feed system, which is responsible for the delivery a material to a printhead and regulates the flow rate. In general, one can distinguish two types of such systems. First of them involves a syringe pump in which a silicone is moved by a plunger, from the syringe, through the tubing, to the print head. This system is inexpensive and easy to use, nevertheless, due to the relatively long connection between the tank and print head, additional volume of material is required which can be treated as waste in the fabrication process. Additionally, due to the same reason, overpressure is constantly maintained in the system which leads to the deposition of material even if the syringe pump is turned off. The other type, known as the pneumatic system, is more expensive and more accurate. In this case, a tank with silicone is directly connected with its print head which eliminates the "dead volume", and the tank is connected to the pneumatic system from the top. This solution allows to more precisely control the deposition introducing many stops during which no material is extruded and, therefore, the amount of waste is reduced almost to zero.

### 2.3.2 Stereolithography method for silicones

Extrusion-based printing methods typically have low resolution but can be adapted easily to work with a diverse type of silicones. An alternative approach known

as stereolithography (SL) which uses light patterning can be used to increase the resolution but is limited only to UV-cured materials. In all SL methods, a premixed photosensitive silicone is poured into a bath, in which a base platform moves in the vertical direction. The features in this layer are exposed using a variety of irradiation methods which polymerizes the silicones in those regions. Once a layer is polymerized, the platform with cured PDMS descends into or ascents from the bath by the amount equivalent to the thickness of a layer and, subsequently, another layer of the material is exposed. The family of SL-based methods can be further divided based on the method used for patterning the exposure, e.g.a vector scan, two-photon, or mask projection approach.

#### 2.3.2.1 Vector scan

Firstly, one can distinguish the direct laser writing approach (DLW), in which the spot of a laser gradually moves along the resin surface, row by row, until the desired layer if fully cured. To initiate the subsequent layer, the platform with the printed object descends into the vat by the value of the thickness of a single layer, and then the curing process is repeated. Thanks to the proper calibration of laser parameters, such as intensity, distance from the liquid surface, and feed rate in the X and Y direction, the molecules of the PDMS polymerize at the focal spot. Therefore, the diameter of the spot determines resolution.

#### 2.3.2.2 Two-photon approach

A more precise variation of DLW is the two-photon [37, 38] approach. In this method, two photons are required to strike the photoinitiator molecule, and, simultaneously initiate the polymerisation. Because the molecule needs a high photon density to be cured, the process can start only in the core of intersection of two

lasers, where the irradiance is the highest. Thus, two beams of light can separately penetrate the vat, not causing any changes in the photopolymers except at the intersecting points. Therefore, the object can be fabricated inside the resin vat which eliminates the necessity for recoating. To secure a high resolution of this method, the light is not delivered continuously, but rather in ultrashort pulses generated every 10ps or even faster. The resolution ranges between 1 $\mu$m and 5 $\mu$m [37, 38], but, under special conditions, it can be even as small as 100 nm [21]. This method, however, turns out to be time consuming when used to print a centimeter-sized object. Moreover, DLW methods cannot be classified as cheap methods, as the precise laser setup is very expensive, especially in the two-photon approach.

#### 2.3.2.3 Mask projection

In order to fabricate larger-scale objects another method is widely utilized, namely Digital Light Processing (DLP) [39, 40], which is based on an optical micro-electro-mechanical technology. The platform with a substrate is submerged in a photopolymer bath and an entire layer of the object is simultaneously exposed to light. The pattern of exposed light is created by a digital micromirror device which reflects the laser light. This device consists of microscopically small mirrors embedded in a matrix on a semiconductor chip and, by controlling each chip, one can rapidly and independently set each mirror up in either reflective or nonreflective configuration. Subsequently, the distance between the printed object and the illumination system is increased by the value of the thickness of one layer of the printed part, and the procedure is repeated until the entire process is finished. The accuracy of the DLP method mostly depends on the size of the micromirror, which can be as small as a few microns, but also it depends on the minimum layer thickness as well as UV light intensity. Compared to DLW, the DLP method is fast because a whole layer

of the fabricated object is exposed to light and crosslinked simultaneously.

Independent of the chosen technique, both the post curing and precise cleaning process are required. What is more, the photosensitive silicone must be compatible with the UV system, since the material needs to be transparent with respect to the UV light. Additionally, SL methods can only be used to create objects made from a single material, which cannot be altered during the printing process. Despite these limitations, such as high cost of the exposure and patterning source, this method guarantees extraordinarily high accuracy and good finish.

### 2.3.3 Inkjet printing method for silicones

Another method that has been recently developed for silicones is inkjet printing where an object is made of deposited droplets. Among the main advantages of inkjet printing, is high accuracy of the deposition of droplets. This feature implies low waste and a possibility of printing multiple-material objects in distinct colors in just one process. One can essentially distinguish two systems of drop generation, the continuous system (CIJ), which is known to be less effective for silicones, and drop-on-demand system (DOD). In the latter, a drop is dispensed because of the overpressure created by either thermal or piezoelectric transducer. Piezo DOD printers are mostly used for PDMS and they are preferred over the ones with thermal transducers because of the specific requirements imposed by the materials. The weakness of the latter is that it works only with aqueous materials, which easily evaporate and withstand the influence of ultra-high local temperature reaching the value of about 350 - $400^0$C without changing any parameters of the used material. However, piezo DOD printers also have some limitations. The main one is that the viscosity of the ink used should be similar to water's, in the range of a few mPa·s.

Because of the surface tension forces, the choice of a material strictly depends on both the geometry of a nozzle and the material it is made of. Additionally, the dispensing device cannot work well when the applied liquid contains particles larger than a few microns (their maximum dimension depends on the diameter of the orifice), but also when the material tends to form bubbles. Despite these limitations, however, there exist certain types of silicones that can printed using the piezo DOD method.

#### 2.3.3.1 Thermally initiated silicone resin

First of them is thermally initiated PDMS which reacts under the influence of elevated temperature. The inkjet method usually relies on either a single or multi-nozzle configuration. However, the single nozzle approach is not applied in the fabrication of silicones, as the throughput of the material through the nozzle is very small which results in long residence time in the dispenser. Such long residence time could initiate polymerization to occur within the dispenser, eventually clogging it. Therefore, the multi nozzle configuration is chosen thanks to which two material ingredients are placed in two tanks separately and dispensed from two independent nozzles [41]. Subsequently, they are deposited on a hot plate alternately, one on the top of another, using either the layer or surface strategy. In the former, both the components are deposited along the same line, where the second substance is added several hundred of milliseconds after the first one. The latter option is slightly different, since the second material is added once the whole surface is filled with the first ingredient. After the deposition of relatively small volumes of materials, they mix by diffusion and subsequently react under the influence of higher temperature, which eventually results in a solid PDMS. Nevertheless, as mentioned above, PDMS is a thermal insulator and therefore consecutive layers of the printed material are

not heated sufficiently fast by the heating of the print bed which elongates the reaction time leading to the swelling of the material and poorer resolution. Hence, this method can only be used to print very thin elements. In general, one can conclude that inkjet methods are not suitable for thermally cured PDMS. They guarantee very good resolution provided the thickness of a printed object will be no larger than a few hundred of microns which is not sufficient in 3D printing.

#### 2.3.3.2 UV curable silicone resin

In contrast to thermally initiated PDMS, UV curable silicones are well-suited for the DOD-based method [42]. It is important to take the necessary precautions against the exposure of light to be able to premix two components and generate drops from one nozzle, as it is done in the extrusion-based printing. However, in contrast to the extrusion method, in the inkjet approach the irradiation takes place after the completion of each layer and it cannot be done together with the deposition [43]. This limitation is caused by two features inherent in the method. First, the flow though the nozzle is slow because of the very small volume of the droplets and, second, the diameter of the orifice is of the order of micrometers which means that even stray light that is reflected can crosslink the material at a tip of the nozzle which leads to a buildup and eventually clog it. Moreover, the nozzle is small and fragile, thus it is difficult to prepare a protective case which will still allow efficient droplet generation. Because the printing and the curing processes are carried out separately, the ink is allowed to spread on the substrate which, leads to the loss of desired resolution. It means one should apply liquid with the viscosity close to the upper limit of the dispensing device tolerance which in result might also significantly affect the accuracy. The Wacker Chemie company developed the technology that enables printing strips about 0.6 mm wide and 0.3 mm thick which is regarded as

the biggest achievement in the field. After the completion of the printing process, a post processing stage is required in order to continue the exposure to UV until the polymerisation of whole printed part is completed. To sum up, DOD-based methods for UV curable silicones guarantee good resolution (worse than SL but better than the extrusion printing) and almost smooth surface of a printed object. On the other hand, the presence of UV system noticeable increases the cost of the printer and make the printing process longer and more complicated.

#### 2.3.3.3 Chemically initiated two-component materials

Inkjet printing method for chemically initiated silicones have rarely been attempted in the literature. However, there exist two techniques for reactive materials (such as hydrogels) which can be utilized also for silicone printing. First of them concerns printing of the low viscous component above a bath consisting of the other component [44]. The platform with the cured material descents into the bath after the completion of a layer. As the curing reaction between the two substances is instantaneous, the viscosity of the hydrogel should be sufficiently low to ensure a free flow after the creation of each layer. The advantages of this method are twofold, first, it features high accuracy, which depends on the printed droplet size and, second, the method is relatively fast because only one material is deposited. On the other hand, the cleaning process in the post processing stage is long and, moreover, it is difficult to perform multi material printing. The other method is designed for low viscous and chemically initiated materials in which both components are dispensed from separate nozzles and deposited one on the top of another [45]. In this method, excluding a positioner and two print heads, no additional equipment is required. Its high accuracy has been successfully verified only for 2D printing. Printing of 3D objects have not been demonstrated with this approach.

Based on the above descriptions, it is clear that there does not exist universal 3D printing techniques that are suitable for the whole family of silicones, including diverse types of PDMS. The choice of a method and material largely depends on design criteria for each application. Nevertheless, one can point out that chemically-initiated PDMS has a few advantages over the others. First, it is initiated in a very simple approach, thus additional and often expensive setup is unnecessary. Second, it is highly reactive which decreases the polymerisation time to only a few seconds and eliminates the need for a gel support material, which usually maintains deposited material in the required patterned position before and during the curing process. Third, by reducing the viscosity, one can significantly improve the resolution of a printed object. Nonetheless, for chemically-initiated, low viscous and highly reactive silicones, one can hardly find any suitable printing methods. Because of a different polymerisation mechanism, the stereolithography technique is not suitable for this type of materials. What is more, the high reactivity feature also precludes the use of extrusion printing as it is impossible to carry out the premixing step, which ensures homogeneous mixing of the two components without the clogging of the dispensing device. Highly reactive components in particular need to be dispensed in small volumes so that they can quickly mix, relatively homogenously, before the polymerization process proceeds significantly. Inkjet methods are ideal for this application because low-volume droplets are deposited from two separate dispensers. However, sequential printing from the dispensers of low viscosity inks leads to loss of resolution. Nonetheless, inkjet printing methods seem to be the most appropriate for low viscous and highly reactive silicones, but they require same further modifications. Therefore, this thesis is focused on overcoming the limitations associated with the inkjet printing process in printing low viscosity, highly reactive

inks by novel design of a printhead.

# 3 Design, Materials and Methods

## 3.1 Design

Low viscosity inks are desirable in 3D printing as they can smoothen the topography that is fabricated during the printing process. However, low viscosity inks can also spread and lead to loss of resolution. Therefore, highly reactive inks that cure instantaneously when the two components are brought together are desirable. Although the chemically-initiated cross-linking is the simplest approach, as it does not require extra initiating equipment, highly reactive and low viscous inks are very hard to fabricate. Such liquids have to be mixed outside the dispensing system once they are separately ejected, because there is a large probability that premixing of these components before pouring them into the chamber or mixing them by an integrated mixer inside the dispensing system, will clog the nozzle. Additionally, the amount of the deposited material should be minimized in order to prevent excessive spreading and achieve good printing resolution. The volume of materials used also influences the degree and uniformity of mixing as both the components continue to diffuse into each other post deposition. Larger droplets can result in inhomogeneous initial mixing and gradient of components across the deposited drop which can also affect the mechanical property of the deposited material. Due to the above-mentioned reasons, two of the common 3D printing methods for silicones, stereolithography and extrusion-based, cannot be applied to low viscosity highly reactive inks. The stereolithography technique requires the two components to be premixed, which are subsequently polymerized under the influence of UV-light. However, the chosen inks rely on a different cross-linking approach, which is initiated chemically when both the components are in contact with each other. On the other hand, in the extrusion

method, in-situ mixing and extrusion could potentially clog the nozzle when used with highly reactive inks. The inkjet printing method, however, satisfies both the requirements, as it enables the ejection of two components separately and the diameter of dispensed drops can be relatively small. Nonetheless, the traditional inkjet method, which is capable of printing one material on the top of another, requires some modification to minimize the time between the deposition of each low viscous component which could reduce the spreading time. Moreover, alternate methods to effectively mix the reactants are needed to create a homogeneously mixed material after deposition. To address this design criteria, a new inkjet printing method, based on an integrated free space droplet mixing module, is proposed in this thesis. The new printing approach enables ejecting two reactive droplets simultaneously, merging and mixing them in free space outside the nozzles, and depositing as one drop in a patterned format on a substrate. However, this technique requires a special 3D printer, in which a printhead consisting of two dispensers and a holder that enables mixing in free space.

### 3.1.1 Configuration and Fabrication of the Printhead

The printhead consists of jet dispensing devices and a holder. The selection of a dispensing device is made based on the drop generation method and properties of the silicone. Thermal DOD dispensing devices use a resistive microheater to rapidly superheat a thin film of ink and eject it thanks to the quick vapor bubble expansion. Therefore, the material must withstand the influence of ultrahigh local temperature and be able to easily vaporize. However, since some silicone components are heat sensitive, this actuation approach cannot be utilized. Alternatively, a piezoelectric mechanism can be used to eject an ink droplet in the inkjet printing method which is more suitable. Therefore, a piezo drop-on-demand single jet dispensing device

$MJ - AB - 80$ from the $MicroFab$ company was chosen. This dispenser consists of a glass capillary, that contains the ink to be printed, surrounded by an annular piezoelectric actuator, as shown in Figure 3.1. The application of a potential to the actuator will deform it, which is then coupled to the deformation of the glass tube that leads to pressure generation in the fluid (ink) inside the tube that subsequently results in droplet ejection. The outlet of the glass tube is in the form of a nozzle featuring an orifice with the diameter of 80 $\mu$m, while its inlet is connected to the fluid fitting. The size of the orifice was purposely chosen to be large so that it would be possible to mechanically clean the orifice in the event that it gets clogged during experimentation. Smaller diameter piezo dispensers, as small as 5 $\mu$m, are available and can be used in the future to generate smaller droplet sizes. The piezoelectrical actuator is wrapped by two electrodes with soldered gauge wires, and it is controlled using an electrical control system known as $JetDrive^{TM}$. The DOD single micro dispensing device is suitable for fluids with the following range of physical properties, namely with the dynamic viscosity below 20 $cPs$, surface tension in the range of 20 - 70 $mN/m$, pH between 2 and 11, and the temperature below 50°C.

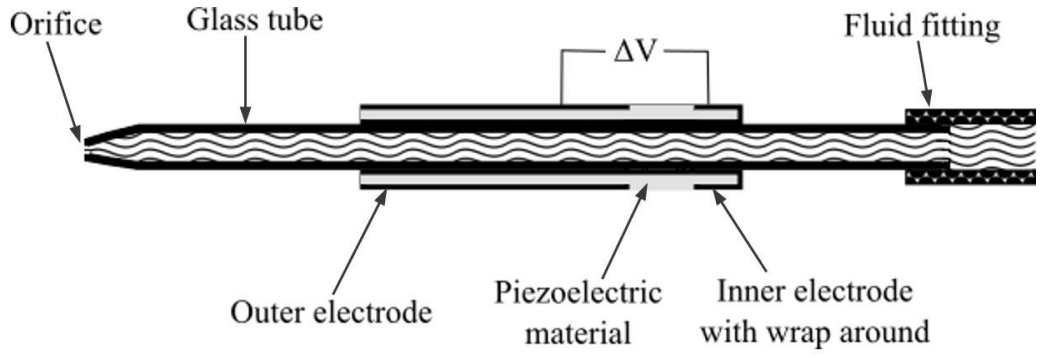


Figure 3.1: MJ-AB style drop-on-demand single jet dispensing device with an orifice whose diameter equals to 80 $\mu$m.

The holder is a crucial element of the printer. It enables the alignment of the

dispenser nozzles in the appropriate positions as well as maintain their positions during printing. The dispensers have to be positioned such that the trajectory of the droplets ejected from them intersect. Therefore, they have to be aligned at an angle to each other. In addition, there are several other design specifications for the holder which needs to be considered. Firstly, the distance between the two ends of the dispenser, marked as $a$ in Figure 3.3, should be large enough to avoid the contact between the two reactive precursors. During the initial setup, there is a possibility that inks would accumulate at the tip of the nozzle. These accumulating droplets can grow to a sufficient size that they touch each other which initiates instantaneous reaction between the reactive components and clogging of the nozzle. Therefore, to calculate the minimum spacing distance $a$, one can consider the maximum possible diameter of a drop the dispenser might handle. This droplet size is a function of the surface tension and gravity forces. The former is proportional to the length of the boundary between the glass capillary and liquid, and it can be expressed in the following way,

$$F_s = 2\pi r\gamma, \tag{3.1}$$

where $r$ is the outer diameter of the glass capillary, while $\gamma$ denotes the surface tension parameter. This force allows to maintain a drop on the glass surface as long as its vertical component is not smaller than the gravity force. This condition can be mathematically written as

$$\frac{4}{3}\pi R^3 \rho g \leq 2\pi r\gamma sin\beta, \tag{3.2}$$

where the left-hand side describes the gravitational force, $R$ is the radius of a drop, $\rho$ denotes the density of liquid, $g$ denotes the gravitational acceleration, and $\beta$ is

the angle between the horizontal surface of the glass capillary and the surface of a drop. Because we are looking for the maximum value of $R$, $\sin\beta$ has to be equal 1, which implies that $\beta = 90^0$. One can rewrite equation 3.2 to achieve the formula for the maximum radius of a drop, i. e.

$$R \leq \left(\frac{3r\gamma}{2\rho g}\right)^{1/3}. \tag{3.3}$$

Using both the above inequality and the material data from Section 3.2.1, the theoretical maximum droplet size was calculated separately for each substance and the results are presented in Table 3.1.

| **Substance's name** | **Diameter** $[mm]$ |
|---|---|
| 30% wt. glutaraldehyde + 20 ppm IPA | 2.34 |
| 50% wt. glutaraldehyde | 2.72 |
| 3-(Aminopropyl)methylsiloxane-dimetylsiloxane ($A_1A_2D_4$) | 2.17 |
| Aminipropyl terminated polydimethylsiloxane (DMS-A11) | 2.54 |

Table 3.1: Maximum diameter of a drop calculated based on equation 3.3 for different materials.

Once can notice that the diameter varies between 2.17 $mm$ and 2.72 $mm$, regardless of the substance type. Additionally, experiments were also performed to determine the maximum diameter that is achievable. Two kinds of materials, namely 30% wt. glutaraldehyde + 20 ppm IPA and 3-(Aminopropyl)methylsiloxane-dimetylsiloxane ($A_1A_2D_4$) were delivered to separate dispensers inclined at an angle of $30^0$. Under the influence of the gravity the materials flow through the dispensing device and accumulates at its tip. The images of hanging droplets captured just before it drops when the surface tension balances the gravity force are illustrated in Figure 3.2. They show that the maximum diameters are 2.3 mm and 2.2 mm for the curing

agent and silicone base, respectively which compares favorably with the theoretical calculations which were 2.34 mm and 2.17 mm for the same materials indicating that the theoretical calculations are a good estimate. Therefore, based on the calculations in Table 3.1, and adding a small safety margin, the distance between the nozzle tip was set to 4 $mm$.

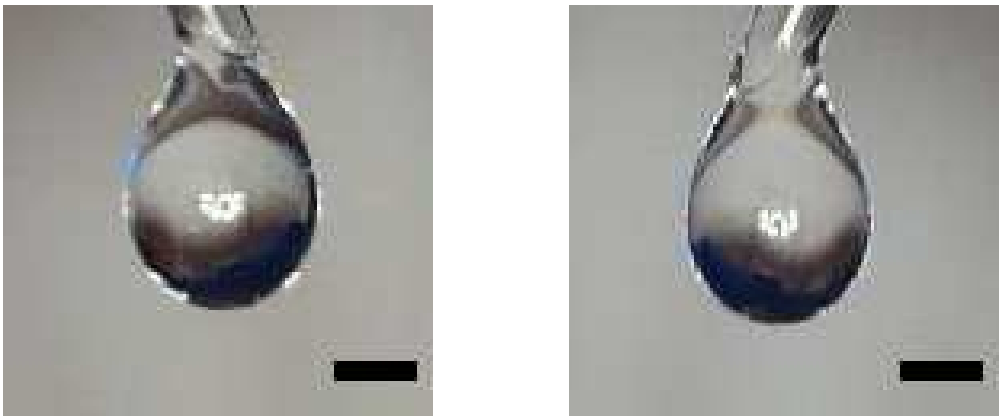

Figure 3.2: The maximum dimension of a droplet accumulated at the tip of the dispensing nozzle. The sale bar = 1 mm. The diameter of 30% wt. glutaraldehyde + 20 ppm IPA droplet is equal to 2.3 mm ($left$), and 3-(Aminopropyl)methylsiloxane-dimetylsiloxane ($A_1A_2D_4$) - 2.2 mm ($right$).

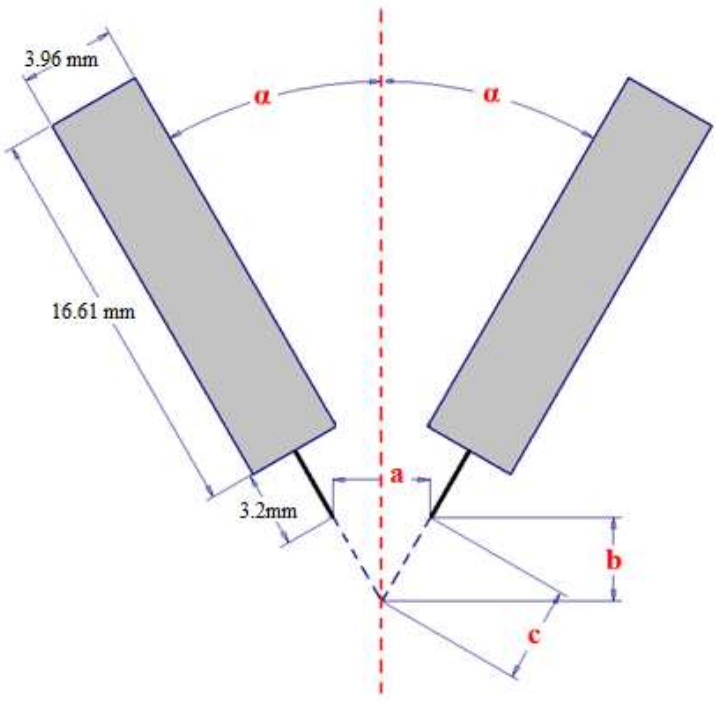


Figure 3.3: A sketch of the dispenser setup with the parameters taken into account in the design of the holder.

It is desirable that the droplets that are ejected from the nozzle travel in a straight-line trajectory so that the nozzles could be easily aligned to enable the droplet to meet each other and merge. Typically, when a droplet is ejected, it has significant momentum and travels along a straight-line path. Over time, is slows down due to drag forces and is susceptible to external influences and the trajectories of the droplets do not follow each other. Therefore, it is crucial to determine the distance (denoted by $c$ in Figure 3.3) over which successive droplets follow the same trajectory and ensure that the paths are aligned such that they intersect within this distance. To measure this critical length, experiments with 30% wt. glutaraldehyde in water solution with 20 ppm of isopropanol and 3-(Aminopropyl)methylsiloxane-dimethylsiloxane was carried out. In the experiment, during the droplet generation process, both the dwell time and voltage are changed, while the rise time, fall time,

and the frequency are kept constant at the value of 7$\mu$s, 12.5$\mu$s, and 300 $Hz$, respectively. The results obtained from the measurement are presented in Tables 3.2 & 3.3 and based on them one can observe that the minimum length of a stable path is equal to 4 $mm$. Finally, based on the $a$ and $c$ parameters as well as the dependencies presented on Figure 3.3, the inclination angle, denoted as $\alpha$, was calculated. If the values of $a$ and $c$ are both 4 $mm$, then $\alpha$ equals to 30°, and the minimum distance between the tips of dispensers and printed bed, $b$, is 3.5 $mm$.

| Dwell time [$\mu s$] | Voltage [$V$] | Length [$mm$] |
|---|---|---|
| 3 | 60 | 5.1 |
| 5 | | 5.9 |
| 7 | | 6.5 |
| 9 | | 7.7 |
| 12 | | 10.1 |
| 15 | | 11.3 |
| 3 | 65 | 8.4 |
| 5 | | 9.5 |
| 7 | | 9.5 |
| 9 | | 10.5 |
| 12 | | 12.5 |
| 15 | | 13.8 |
| 17 | | 9 |

Table 3.2: Printing parameters and the length of a stable droplet path for 30% wt. glutaraldehyde in water solution with 20 ppm of IPA.

| Dwell time [$\mu s$] | Voltage [$V$] | Length [$mm$] |
|---|---|---|
| 9 | 90 | 4.7 |
| | 93 | 5.9 |
| | 95 | 7.3 |
| 16 | 82 | 5 |
| | 84 | 6.4 |
| | 86 | 9 |
| | 88 | 9.6 |
| 24 | 90 | 5.3 |
| | 92 | 5.3 |
| | 94 | 6.4 |
| | 96 | **4** |
| | 98 | 5 |
| | 100 | 7.2 |

Table 3.3: Printing parameters and length of a stable droplet path for 3 - (Aminopropyl)methylsiloxane - dimetylsiloxane.

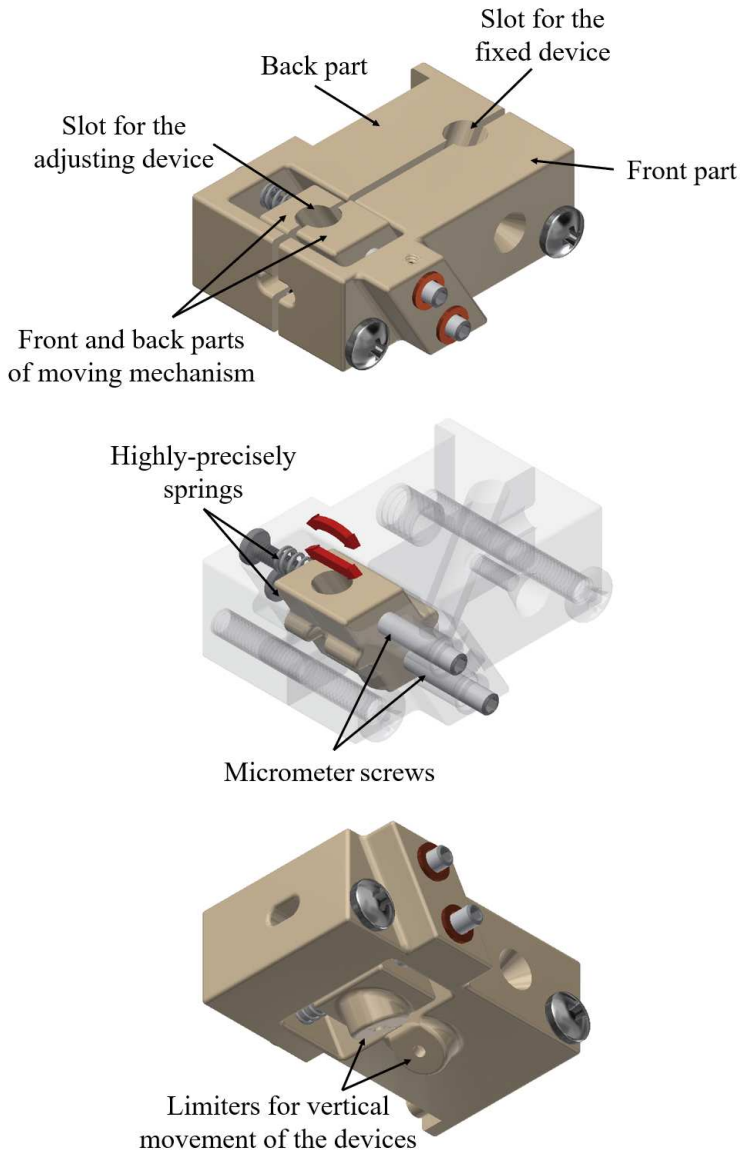


Figure 3.4: Holder designed for the dispensing devices (*top*), the regulation mechanism (*center*), and the view of the bottom part of the holder (*bottom*).

The holder was also designed in a modular manner as illustrated in Figure 3.4 (*top*), so that it can be easily dismantled and cleaned. In addition, to make the printhead more robust to small variations in printing parameters or other environmental factors, adjustable mechanisms were incorporated. One nozzle is held fixed while the other nozzle slot has two degrees of freedom incorporated to move it rectilinearly in

the plane parallel to the dispenser's plane and deviate by maximally two degrees as marked by the red arrows in Figure 3.4 (*center*). The regulation mechanism allows for precise positioning of dispensers controlled by two micrometer screws at the front and two high-precision springs at the rear. As shown in Figure 3.4 (*bottom*), the movement of the dispensers is limited to ensure their identical positioning relative to the holder.

### 3.1.2 Design of the 3D printer

The 3D inkjet printer, illustrated in Figure 3.5, consists of five main sub-assemblies, namely a printhead including jet dispensing devices and a holder, positioner, an electronic control system for dispensers, chambers for the material, and, finally, a vacuum pressure system.

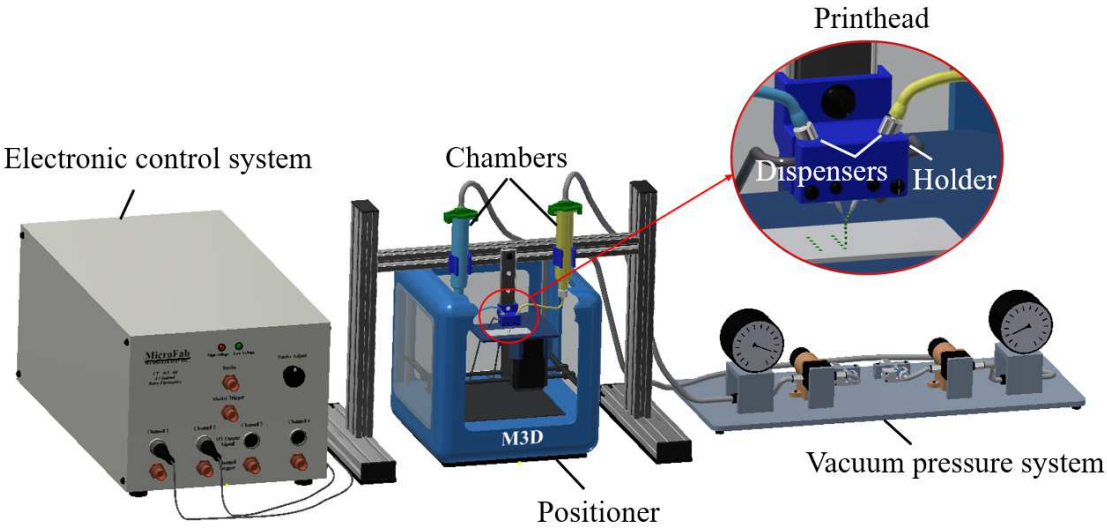


Figure 3.5: 3D inkjet printer.

The printhead was described in detail in the previous subsection. However, another critical constituent of the designed 3D printer is the XYZ positioner, which was adapted from a commercial and inexpensive 3D printer, *The Micro+* from the

*M3D* company. The positioner enables building 3D objects with the maximum dimension of each side of 11 centimeters, positioning accuracy in both the X and Y directions no less than 15 microns, and layer resolution ranging between 50 and 350 microns. Thus, one can notice that the theoretical printing parameters, especially the resolution, are not impressive, and they cannot guarantee high quality printing. Nevertheless, the choice of this particular printer was dictated by its one unique feature. The droplet generation and free space merging process is sensitive to any mechanical force that act on the printhead. Therefore, it is desirable to have a stationary printhead and impose all the XYZ axis movements on the print bed to facilitate coherent printing. The "Micro" printer is ideal for adaptation for such a print bed design. It has a design such that the print bed is stationary, and all the movement is fed into the printhead. Thus, modifying the printer by removing its original printhead and attaching an adapter that serves as a print bed, a XYZ movable print bed can be easily made. Such a movable print bed was additionally protected against potential vibration generated during the movement. Also, since the ejected droplets are very sensitive to the air movement, three sides of the positioner case, left, right and rear, are covered by a PVC transparent sheet to minimize the impact of external air flow. Both the top and front sides remain open to allow free access to the dispensers and printing bed, and also to facilitate recording a video by a camera. Finally, a vibration damping rubber was attached to the base of the positioner, to reduce the impact of vibrations generated by the five stepper motors on the droplet generation at the printhead, and to make the alignment of the droplet streams in free space possible.

The electronic control system, $JetDrive^{TM}$, can generate electrical impulses with a wide range of characteristics (such as amplitude, rise and fall times) which enables precise control of the size and the velocity of the droplets generated. The impulses

can be controlled by setting various parameters of the generator, for example, the voltage can be chosen from the range between - 140 $V$ and 140 $V$, rise and fall time can be set between 1$\mu$s and 3276$\mu$s, dwell time between 3$\mu$s to 3278$\mu$s and, finally, the frequency can vary from 1 Hz and 30 $kHz$. These parameters can be set via a computer using $JetServer$ software.

The barrel syringes were purchased from $Nordson\ EFD$, and they serve as chambers for the reactants of PDMS that are to be mixed. They are connected to the dispensers via a chemically inert tubing (3 cm length), and to the vacuum system from the top via an adapter. The 10 ml syringes are made of chemically compatible polymers and they are specially designed to eliminate material waste, turbulence and dead zones, that could trap air. Typically, it also consists of a piston in order to push high viscosity ink. However, the piston was removed to adapt it for use with low viscous liquids which requires application of a vacuum back pressure rather than a positive pressure.

The vacuum pressure system consists of a pump, check valve, regulator, and gauge. The key role of the system is to balance the capillary and hydrostatic pressure at the orifice and, consequently, to form a stable meniscus during the printing process. One can estimate from the height of the syringe above the nozzle that the maximum hydrostatic pressure imposed by the liquid in the syringe will be less than 1.38 $kPa$ and, therefore, a small air vacuum pump, KPV-14A from the Cole-Parmer company was chosen. Despite its miniature size, the pump parameters in easily meet the requirements; the maximum vacuum pressure it generates equals to 81.34 $kPa$, while the flow rate is no greater than 0.4 $L/min$. The pump is connected to the regulator, V-800-30-W/K from the Airtrol company, with a check valve which prevents the back flow of air. The main task of the regulator is to set the pressure, which depends on the hydrostatic pressure induced by the liquid, in the range between 0

and 101.6 $kPa$ with the sensitivity of 0.25 $kPa$. The vacuum air flows through a gauge, which measures its pressure, and reaches the syringe. As the two dispensers are used independently, each element of the vacuum system is duplicated.

### 3.1.3 Working principle of the Inkjet Printing Method with an Integrated Free Space Droplet Mixing Module

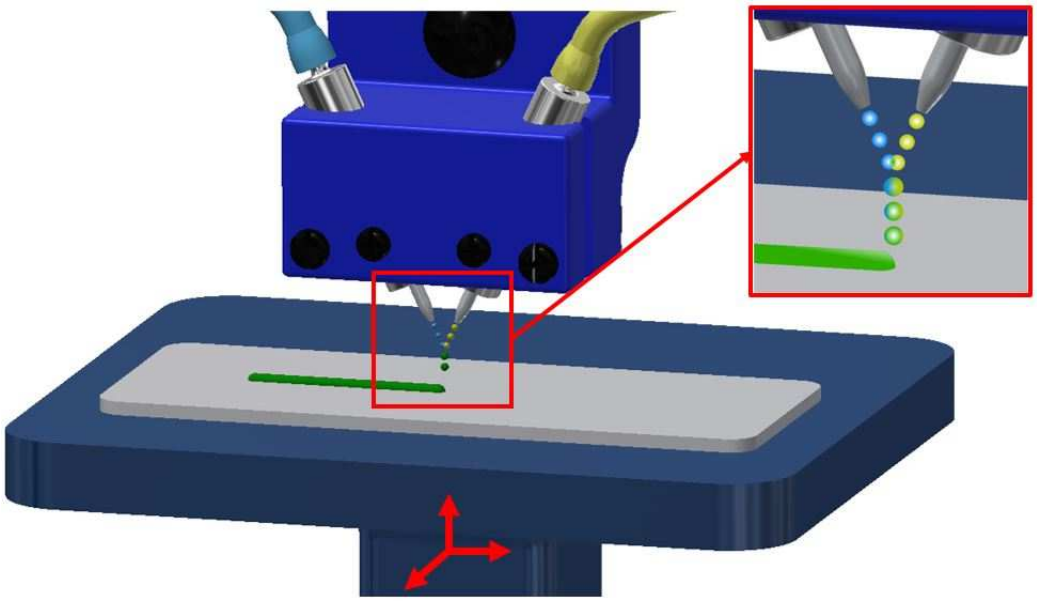

Figure 3.6: The working principle of the proposed inkjet printing method with free space mixing process.

The working principle of this method is presented in Figure 3.6. It involves the simultaneous ejection of two droplets of highly reactive components using two separate dispensers that are inclined towards each other at a defined angle. The dispenser nozzles are assembled such that the trajectories of the dispensed droplets lay on the same plane to enable their collision and merging in free space between the dispensers and the print bed. Subsequently, the combined drop falls vertically down and attaches to the print bed. To ensure that they meet both spatially and temporally, both the trajectory and velocity of the drop should be precisely controlled.

Therefore, a holder was designed so that fine control over the position and the angle between the nozzle tips can be adjusted. The velocity of the droplets that are ejected can be controlled by the electrical impulses applied to the piezoelectric actuators on the dispensers. In the ejection process, the droplets have a relatively large velocity. At the moment of collision, the horizontal components of their velocities must balance such that they cancel the net momentum in that direction and the combined drop falls down. The impact of the one drop on the other could initiate mixing of the content of the droplets. In addition, the impact of the combined drop onto the substrate will also cause mixing of the contents. Finally, diffusion of the molecules also occurs that ensures homogenization and mixing over a longer term. The inks are designed such that they polymerize upon contact with each other instantaneously. However, it is important that the combined drop remains in a reasonably liquid state until the deposition, so that it is capable of spreading and adhering to the underlying substrate and producing smooth features. Due to its sensitivity, the dispensing system was designed to be immobile during the printing process and an XYZ positioner was used to move the substrate. The positioner moves in the XY plane during the printing of a layer and then it descends to continue further deposition. Therefore, the shape of the printed object is critically dependent on the platform movement.

## 3.2 Materials

The PDMS used in experiments is crosslinked thanks to both a traditional strong covalent bond and an additional dynamic non-covalent bond of imine. Generally, PDMS elastomers belong to the family of thermoset materials, which are not reprocessable. Nevertheless, the imine-based cross-linking ensures macroscopic freedom which improves the mechanical properties, self-healing, and recyclability of the ma-

terial. What is more, the cross-linking reaction is carried out without any catalysts, and its only by-product is water. In addition, this method is generic as it can be applied to a wide range of commercially available aldehyde and amine components, thereby lowering the cost of PDMS-based reactive inks. Lastly, it is worth mentioning that the materials made through imine cross-linking are biocompatible.

In the experiments, 3-(Aminopropyl)methylsiloxane-dimethylsiloxane was used. This material is a mixture of AMS-132 (2 - 3% mol aminopropylmethylsiloxane, 4500 - 6000 MW), AMS-162 (6 - 7% mol aminopropylmethylsiloxane, 4000 - 5000 MW), and octamethylcyclotetrasiloxane, which was prepared in two compositions. First, the volume ratio of the three components was respectively 1:1:1, and this substance will be referred to as $A_1A_2D$. The other composition features the ratio 1:1:2 and it is named $A_1A_2D_4$. Additionally, as an alternative to the above materials, DMS-A11 (aminopropyl terminated polydimethylsiloxane, 800 - 900 MW) was also utilized. These three telechelic polymers/monomers, $A_1A_2D$, $A_1A_2D_4$, and $DMS-A11$, will be collectively referred to as a silicone base. In addition, Glutaraldehyde solution, 30%, 38%, 40% and 50% wt. in water was used as a curing agent, to which in some cases methanol or isopropanol was added to prevent the material from autocondensing during the storage. Moreover, these solvents also were used to decrease the value of surface tension and to improve the miscibility between the two ingredients. Apart from methanol and isopropanol, a surfactant triton X - 100 was utilized.

The glutaraldehyde-aminopropyl silicone (PDMS) is prepared using a silicone base and curing agent mixed together. The mixing phenomenon can be excited either by external forces or by diffusion. During this process, the viscosity of the mixture increases until it solidifies to a free standing gel. It is difficult to unambiguously determine the gelation time, especially when the mixing of the two components is driven mainly by the diffusion. In this case, the gelation time depends on the

properties of the used materials and their volume. For example, two drops, each consisting of 7 $\mu$L of DMS-A11 and glutaraldehyde 50 % wt. in water, need around 10s to transform to a gel state if one is dispensed on the top of another. At an early stage of the curing, the gel is soft, yellow, and moldable. However, once the polymerization process progresses, which is illustrated in Figure 3.7, it becomes deep brown, and its Young modulus and shore hardness increases.

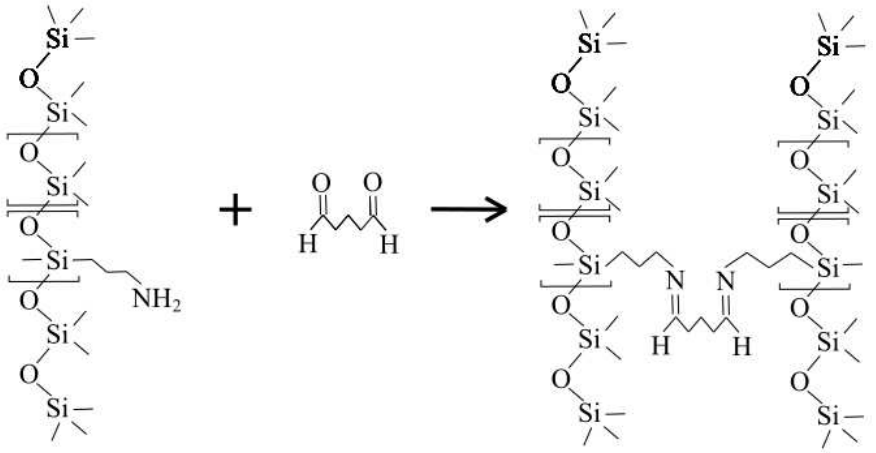


Figure 3.7: The simplest formulas describing the reaction of glutaraldehyde with 3-aminopropyl PDMS.

In general, the curing process can be accelerated in several ways, for instance, by drying the material in a vacuum oven, or by placing it in an oxidized or aqueous environment. In addition, one can control the reaction time by varying the pH (2.5 $<$ pH $<$ 12) of the curing agent, which consists of a mixture of hemiacetals and aldol condensation polymers. In the case of low pH, the aldehydes reversibly condense to hemiacetals and, therefore, the reaction is slow. In contrast, when the value of pH is high, the final product involves very few hemiacetals and its polymerized form is obtained from the condensation of polyglutaraldehydes with attached imines in a fast and non-reversible cross-linking process. On the other hand, in order to slow down the polymerization, one can either initiate the reaction using nitrogen

or reduce the concentration of the curing agent. However, the latter option is not recommended as the added solvent might change the final condensation products.

### 3.2.1 Critical Fluid Properties in the Context of 3D Printing

For the purpose of this project, a new 3D inkjet printer for highly reactive and low viscous silicones was developed. Therefore, it is critical to select suitable materials to verify if the new printer is working as desired. In the experiments involving different printable liquids, emphasis was given to three main conditions. First, the materials should satisfy the physical requirements of the printer, which means that the values of viscosity, surface tension and pH must be in the range permitted by the dispensing device, namely 0 - 20 $mPa \cdot s$, 20 - 70 $mN/m$, 2 - 11, respectively. Second, during the printing process, these parameters should not change, as any variations can affect both the diameter and velocity of the dispensed droplet. Therefore, the amount of the IPA or methanol incorporated into the inks should be reduced to a minimum, because both the alcohols are easily vaporizable liquids and their evaporation over time can result in changes in physical parameters such as viscosity and surface tension that could make the printing process unstable. Additionally, one should pay attention to the homogeneity of the materials, because some of them undergo autocondensation in the preparation process which leads to the undesirable formation of precipitates. Third, one should also investigate the pH value of a material, as this quantity has a direct influence on the polymerization process. It was shown in an experiment with silicic acid, that the rate of the polymerization increases with pH [46]. This result is very important in the context of the proposed 3D printing method, hence the inks with higher values of pH was preferred.

Based on the measurement of different material properties and the above selection criteria, the choice of two curing agents and two silicone bases for further experiments was made which is presented in Table 3.4. The table with the all tested materials is placed in Appendix B.

| **Substance name** | **Density** $\left[\frac{kg}{m^3}\right]$ | **Viscosity** $[mPa \cdot m]$ | **Surface tension** $\left[\frac{mN}{m}\right]$ | **pH [-]** |
|---|---|---|---|---|
| 30% wt. Glu.+20 ppm IPA | 1002 | 11.54 | 35.00 | 3.5 |
| 50% wt. Glu. | 1198 | 17.42 | 65.32 | 4 |
| $A_1A_2D_4$ | 948 | 14.43 | 26.30 | 10 |
| DMS-A11 | 935 | 17.86 | 41.55 | 10.5 |

Table 3.4: Selected properties of the applied materials.

The densities of liquids were calculated using the standard formula involving mass and occupied volume. These liquids were dosed into a container using air displacement micropipettes and, subsequently, their mass was measured with a high precision electronic laboratory balance that had a resolution of 0.1 mg. Every measurement is repeated five times to determine the error in measurement. In the measurement of the viscosity, a cone-plate version of a StressTech HR high-resolution oscillatory rheometer was used. This device regulates the applied stress by changing its value between 0.05 and 150 Pa. Although the curing agent and silicone base belong to the two different families of liquids, Newtonian and non-Newtonian, respectively, both of them feature a linear dependence between the dynamic viscosity and shear rate, which is characteristic for Newtonian fluids. The response of the silicone base can be caused by a low value of the molecular weight. It was reported that the polymers featuring low molecular weights do not behave as the majority of polymeric liquids, whose effective viscosity reduces under the influence of shear rate [47]. The surface tension was calculated using the pendent drop approach, which is an optical method that facilitates analyzing the shape of an axisymmetric drop utilizing the ImageJ software with the Pendent Drop plugin [48]. Lastly, the pH was measured using a pH test strips with the accuracy of 0.5.

### 3.2.2 Dimensional Analysis of Stable Droplet Generation Process

Certain physical properties of a material, such as the viscosity, molecular weight, and surface tension, directly impact on its printability. The viscosity, for example, is responsible for the energy loss during the droplet ejection and, therefore, its increase can slow down the jetted droplets. If both the viscosity and frequency of the droplet generation are high, the printing process can be unstable, as there might not be enough time to refill the nozzle between two consecutive cycles. The viscosity is a function of many factors, including the molecular weight. The relation between the viscosity and molecular weight is linear if the latter quantity is small. A nonlinear dependence may occur not only in case of a large molecular weight, but also if the ink contains branched polymer. In the inkjet printing method, one can identify four types of droplet ejection phenomena that depend on both the molecular weight and concentration of polymers. First, if the values of these two quantities are low, the ejected drop features a long tail, which breaks up into several satellite drops. This kind of printing is very unstable, irreproducible, and it results in a mediocre quality of printing. Further increase of the values of both the quantities leads to the second kind of droplet ejection, in which a few satellite drops appear only at the end of the ligament. As the molecular weight and concentration are increased further the third type of behavior is observed in which a single spherical drop is ejected. This condition guarantees stable and repeatable printing. Finally, in the fourth type, very high molecular weight and concentration change the polymer mechanical properties into viscoelastic, hence the droplet usually cannot leave the nozzle [49]. In addition to that, a high value of the surface tension also facilitates the accumulation of the material at the tip of the nozzle during the printing, which hinders the droplet ejection. In general, one can notice that the droplet genera-

tion process is complex and strictly dependent on the underlying flow phenomena. Therefore, different dimensionless numbers, in particular, the Reynolds ($Re$), Weber ($We$), and Ohnesorge ($Oh$) number, have been used in literature to characterize the droplet printing process involving droplet generation and deposition. The Reynolds number,which reflects the ratio of fluid inertia to viscous forces, is defined in the following way:

$$Re = \frac{v\rho d}{\eta}. \tag{3.4}$$

The Weber number represents the relation between the inertia and surface tension, and it can be written as:

$$We = \frac{v^2\rho d}{\gamma}. \tag{3.5}$$

Finally, the Ohnesorge ($Oh$) number is described by the equation

$$Oh = \frac{\sqrt{We}}{Re} = \frac{\eta}{\sqrt{\gamma\rho d}}, \tag{3.6}$$

where $\rho$, $\eta$, and $\gamma$ respectively denote the density, dynamic viscosity, and surface tension of the liquid, while $v$ and $d$ are the velocity and characteristic length.

The studies concerning the droplet formation mechanism were originally reported by Fromm [50]. In this pioneering research, involving numerical simulations of Newtonian fluids, the Ohnesorge number was used to characterize the behavior of droplet. Fromm postulated that the value of Oh reciprocal, $Z = 1/Oh$, should be lower than 2 to have stable droplet ejection. This phenomenon was further analyzed by Reis and Derby [51], who concluded that a stable drop formation is possible if $10 > Z > 1$. They showed that if $Z$ is below 1, the viscous dissipation prevails and therefore, the droplet ejection is impossible. Their simulations also proved that if $Z$ exceeds 10, large amount of satellites are generated. In another experiment, the Duineveld

group [52] took into account the influence of the surface tension between the liquid, air and nozzle. They assumed that the drop must have enough kinetic energy to overcome the surface tension forces. Based on that, they suggested an equation for the minimum required velocity for the droplet generation, i.e.,

$$v_{min} = \sqrt{\frac{4\gamma}{\rho d_n}}, \tag{3.7}$$

where $d_n$ denotes the nozzle diameter. Since the analysis was carried out using dimensionless numbers, equation 3.7 was plugged into 3.5, giving rise to the following inequality,

$$We = v_{min}\sqrt{\frac{\rho d_n}{\lambda}} > 4. \tag{3.8}$$

From 3.8, one can compute the minimum kinetic energy necessary to secure stable printing.

Finally, one can determine the threshold for stable droplet deposition based on the analysis of the collision of the ejected droplet and substrate. In an experiment, Stow and Hadfield [53] deposited a drop of water on a dry metal substrate to show that the splashing of the deposited material is dependent on the surface roughness of the substrate. They concluded that only if

$$We^{1/2}Re^{1/4} > K(R), \tag{3.9}$$

the onset of splashing occurs, where $K(R)$ is a splash parameter dependent on the surface roughness.According to the literature [54, 55], the splashing on a flat and smooth surface can be observed when $K(R)$ exceeds the value more or less equal to 50.

Formulas 3.6 - 3.9 together with the range $10 > Z > 1$ might be visualized in a phase

diagram, defined in the Re-Oh space. The plot in Figure 3.8 illustrates the regime in which the fluid properties enable stable printing in a DOD inkjet system. Because the analysis of stable printing is based on dimensionless numbers, the results are universal for most Newtonian fluids. However, in case of fluids exhibiting non-linear behavior, for example, polymer solutions, the region for stable droplet generation may be slightly different.

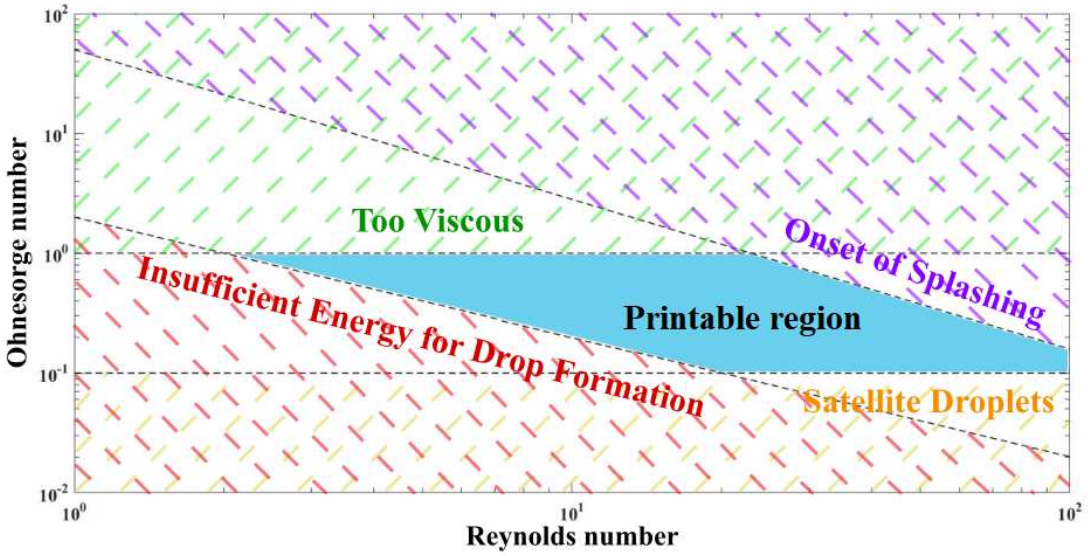


Figure 3.8: Diagram highlights the range of fluid properties,for which stable printing in a DOD inkjet system is feasible [56].

## 3.3 Methods

### 3.3.1 Observation and registration of ejected droplets

During the experiments, three different cameras were usually utilized to observe the droplet generation, as well as other events occurring in the nozzle. One of them was a digital microscope camera, *MicroDirect* 1080*p HDMI Handheld Digital Microscope*, form *Celestron* company, which enabled high magnification (220X) observation of the printing process. The camera was assembled in front of dispensers

in a distance between 2 cm and 14 cm depending on the magnification, to record the dispensing and clogging, that can occur occasionally at the glass tip of the nozzle. In addition, based on the careful analysis of the prepared pictures, the dispensers were appropriately calibrated to produce a straight and stable jet. Unfortunately, the biggest drawback of the camera was its limited frame rate, which did not exceed 30 $fps$, thus, the registration of an individual drop was impossible. Therefore, a high-speed $Fastec\ Imaging\ TSHRMS$ camera with $Monozoom-7$ lens was used. For the purpose of the experiments, the camera and a light were mounted on two sides of the dispensers, in a distance around 15 cm. Its frame rate upper limit was 2,000 $fps$ which enabled a detailed observation of dispensed droplets and measurement of their respective diameters. Nevertheless, the recording speed was found to be too low to determine the velocity of the drops. In addition, this camera required significant amount of lighting to produce clear pictures, especially when droplet ejection occurs at high speeds. Finally, the third camera, a high-speed $Fastcam\ AS4$ assembled with $Monozoom-7$ lens, was occasionally used due to limited access. Its remarkable recording specifications, namely the frame rate up to 500,000 $fps$, lower light intensity requirements, and greater flexibility with respect to the shutter time, allowed to precisely observe the droplet ejection phenomena.

In the measurement of the diameter and velocity of ejected droplets, mostly the $Fastcam\ AS4$ camera was utilized taking pictures in resolution 320 x 240 pix with the frame rate 10,000 $fps$. The $Monozoom-7$ lens was used to magnify the droplets with a resolution of 4 $\mu$m/pix. Using these parameters, one dispensed droplet was registered on at least five snapshots dependently on its velocity. Subsequently, the pictures were analyzed using Matlab software, which measured the diameter of the drop and localized its center, which was used to calculate velocity. Dependently on the position of the droplet, the accuracy with which its diameter could be estimated

varied by +/- 4 $\mu$m which was caused by uneven distribution of light. In the center which was the lighter area, the droplets were focused, and therefore its diameter was smaller, however closer to the edges the background was darker, which occasionally influence on the droplet size.

### 3.3.2 Accuracy of the positioner

Since the XYZ positioner used was part of an inexpensive, commercially available 3D printer it had poor accuracy and was not completely rigid after assembly. This drawback is critical in case of inkjet printing methods, because any unwanted vibration significantly affects the printing resolution. To verify the effect of positioner accuracy on the printing process, an experiment was conducted in which a particular path was provided to the positioned and the resulting print bed movement was recorded by a microscope camera. The displacements were measured separately for each axis which was repeated at least ten times with different path length, to better understand the behavior of the positioner. It was found that the displacement provided by the software and the actual resulting displacement of the print bed were proportional to each other but not the same. The linear fit of their relationship can be represented as: x = 0.955X, y = 1.067Y - 1.667, and z = 0.983Z, where the x, y, z represents the measured displacement of the print bed along those axes while the X, Y, Z represents the displacement that was input into the software. Therefore, to account for this error, the design of the objects to be printed were dimensioned considering this relationship so that the intended dimensions could be accurately printed. Furthermore, the XYZ positioner was also imaged using a high-speed camera to determine the amplitude of vibration induced due to the stepper motors. The amplitude was found to be $\sim$ 32 $\mu$m which is significant considering that the diameter of the printed droplets is close to 50 $\mu$m. Therefore, this vibration could

have a significant effect on the smoothness of the walls of the printed structure. All of these effects could be mitigated by using a higher resolution positioning system that the one used albeit at a higher cost.

### 3.3.3 Preparation of the printing process

The preparation of the printing process consists of a few steps. Once the printer is assembled, as shown in Figure 3.6, the adapters of the vacuum pressure system are disconnected from the chambers and the two inks are poured into two separated syringes. Under the influence of gravity forces, the inks push air out from the dispensers and accumulate at the tip of the nozzle. The vacuum system is then connected with the chambers and subsequently turned on. Next, the dispenser tips are wiped and each of them is separately activated so that stable droplets are generated. This is achieved by adjusting the parameters of electrical signals and by setting the vacuum pressure to a proper value. Afterward, both the dispensers are simultaneously turned on, and the droplets are spatially and temporally calibrated so that they could merge with each other. For this purpose, the position of one of the dispensers is manually regulated using the screw-spring mechanism in the holder, and the velocity of the ejected droplet is adjusted by controlling the electrical impulses delivered to the piezoelectric actuator. Usually, a high-speed camera is used to observe the droplets in the calibration process. It is possible to secure stable coalescence without recording equipment but, however, that would be more time-consuming. Once the droplet mixing process is stabilized, the positioner is turned on and the printing can be initiated. After every experiment, the dispensers must be carefully cleaned, as it is probable that the inks, which are highly reactive, undergo autocondensation. A detailed description of the cleaning procedure is included in Appendix A.

# 4 Characterization of the droplet generation and mid-air mixing

In order to print low viscous and highly reactive materials, the modified inkjet printing method was applied. The droplet generation process in inkjet printing is complex and strongly depends on physical properties of utilized ink. Therefore, in this chapter, the capabilities of the selected dispensing devices working with reactive inks will be presented. Additionally, due to the presence of the integrated free space mixing module, the stability of droplet generation and mixing phenomena will be carefully investigated under different conditions.

## 4.1 Working Principle of Piezoelectric Dispenser

The dispenser, presented in Figure 3.1, is made of a glass tube with an integrated nozzle and bonded with an annular piezoelectric element. The piezo actuator consists of outer and inner electrodes and, depending on the applied electrical impulses, it can both compress radially and expand axially (or vice versa) the glass chamber. However, the glass capillary deforms only in the neighborhood of the actuator.

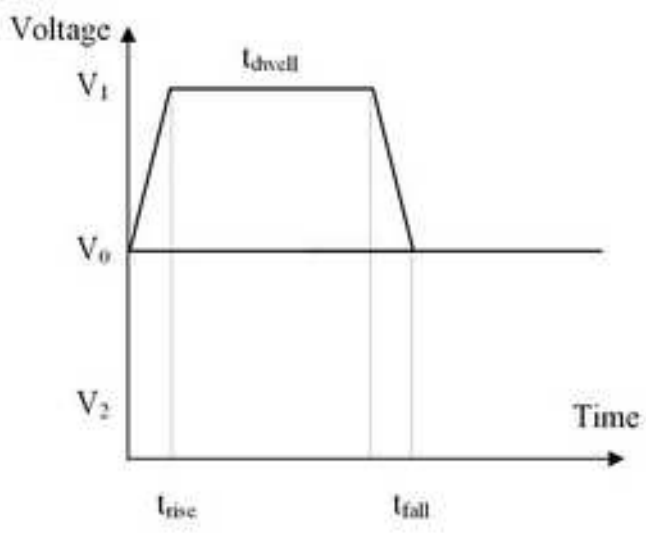


Figure 4.1: A trapezoidal actuation signal.

The simplest actuation signal applied to the electrodes is characterized by a trapezoidal (unipolar) waveform involving three time frames, as illustrated in Figure 4.1. The first one is the rise time, during which the voltage applied to the piezo actuator increases, causing its deformation which, leads to the increase in the glass tube diameter. The next one, the dwell time, defines the period in which the tube remains in a deformed configuration. Finally, the third regime, called the fall time, determines the time in which applied potential returns to zero and affects the deformation of actuator. The glass capillary then returns to its normal state. The entire deformation of the actuator leads to a pressure generation inside the capillary. The actuation signal amplitude directly influences the magnitude of deformation. In particular, variations in the glass tube diameter occur when the voltage value changes during either the rise or fall period.

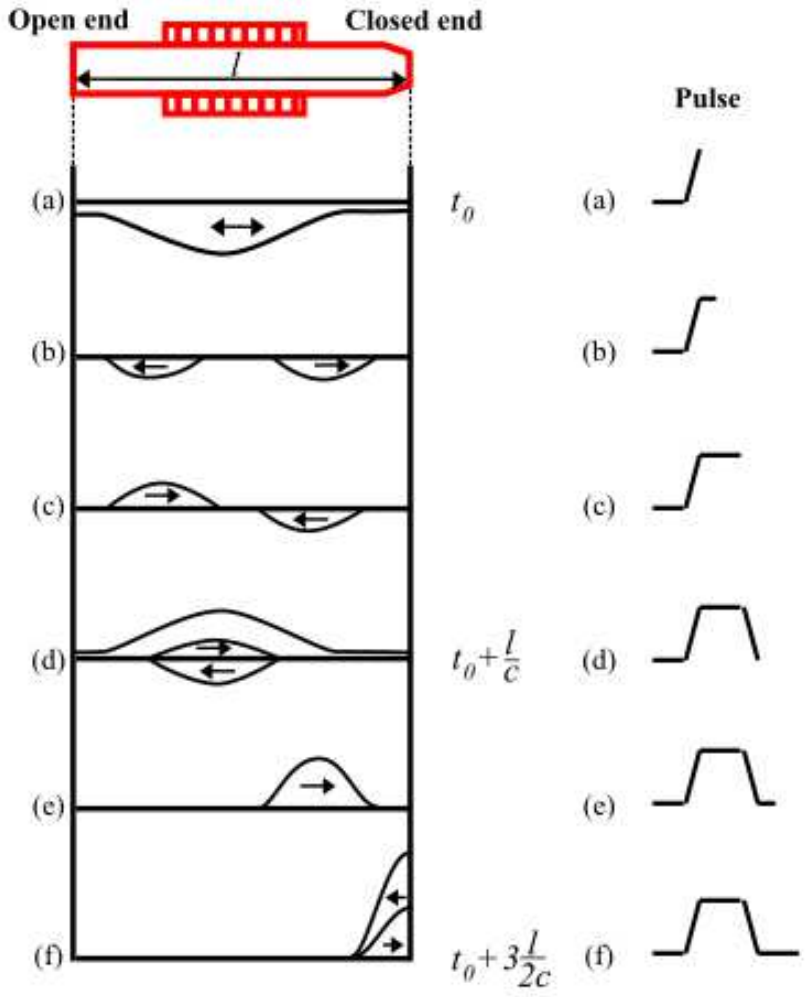


Figure 4.2: Propagation and reflection of the initial pressure pulse in an open-close squeeze tube [57].

The deformation of the glass tube influences the behavior of the liquid inside the dispenser. The rapid expansion of the tubular glass, caused by the growth of applied voltage in the rise period, generates a negative pressure wave, as visualized in Figure 4.2 (a). In the next step, which is the dwell period, presented in Figure 4.2 (b), the wave splits into two halves and each of them moves with the speed of sound in the ink in opposite directions, one travels to the orifice and the other one towards the supply end. The tip of the nozzle can be considered as a closed end because the diameter of the orifice is very small compared to the diameter of the tube.

However, the supply end, whose diameter is slightly larger than the one of the tube, is regarded as open. The presence of an open and close end determines the behavior of the pressure wave, as shown in Figure 4.2 (c). The wave approaching the closed end bounces back and moves towards the center of the tube. The second one that approaches the open end also bounces back; however, its sign changes from negative to positive. Thus, after the time $l/c$, where l is the length of the glass tube and c is the speed of sound in ink, both propagating waves should have travelled the same distance and met at the same point, as presented in Figure 4.2 (d). Although the net pressure equals to zero, the waves do not interfere with each other and can still propagate. In the final time stage, i.e. in the fall period, the voltage value drops to zero. As a consequence, the glass tube comes back to its original state, which leads to generation of another pressure wave similar to the initial one, but with the positive sign. Subsequently, this wave neutralizes the negative pressure wave and amplifies the positive one, which moves towards the orifice, as illustrated in Figure 4.2 (d and e). However, at the closed end (see Figure 4.2 (f)), the amplified pressure wave is split into two smaller ones. The reflected one travels back to the dispenser interior, while the second one moves out of it leading to the droplet ejection. It is estimated that at the time $3l/2c$, after the primary expansion of the dispenser, the pressure in the nozzle is four times higher than its initial value and therefore, the condition necessary for successful droplet generation is satisfied. To sum up, one can estimate that the width of the generated electrical pulse should be approximately equal to $l/c$, to guarantee the maximum possible value of the amplified pressure and thus the maximum volume and velocity of the ejected droplet. However, the ejection is delayed by $3l/2c$ with respect to the initial time [57].

## 4.2 Droplet generation Phenomenon

The theoretical model describing the correlation between electrical impulses and a pressure wave in a dispenser incorporates the impact of a single impulse only. During the injection, however, apart from the injecting wave, one can also observe residual waves travelling back inside the dispenser. Therefore, in a long printing process the cumulation of residual oscillations may hinder the droplet generation. Moreover, in order to optimize the injection process, the speed of sound in the ink filling the capillary must be known to appropriately generate electrical impulses. However, this parameter is unknown for many materials such as those used here, i.e.curing agent 30% wt. glutaraldehyde in water with 20 ppm IPA and silicone base $A_1A_2D_4$. Therefore, the characterization of the effect of various electrical parameters on the droplet ejection process for both the liquids was carried out.

The characterization was performed by capturing monochrome optical images of the droplet as it is ejected from the nozzle using a high-speed camera (*Fastec Imaging TSHRMS*). The volume of the droplet and its velocity were determined based on the image analysis. Moreover, the influence of each impulse parameter on the droplet behavior was examined separately.

### 4.2.1 Effects of dwell time

First, glutaraldehyde in water solution was characterized in detail. In the experiment, the dwell time value was increased from 2$\mu$s to 18$\mu$s, however the other parameters of an electrical impulse were constant, the rise time was equal 7$\mu$s, fall time - 12.5$\mu$s, frequency - 300 Hz, voltage - 55 V.

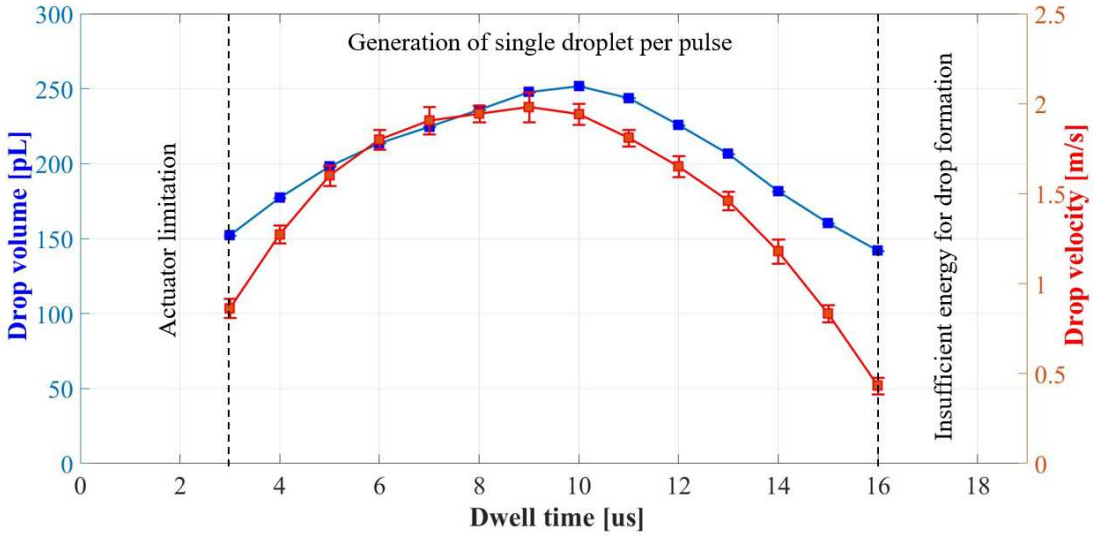


Figure 4.3: Both the volume and velocity of a drop, consisting of 30% wt. glutaraldehyde in water solution with 20 ppm IPA, depend on the dwell time. Electrical impulse generation parameters: the rise time - 7$\mu$s, fall time - 12.5$\mu$s, frequency - 300 Hz, voltage - 55 V.

The obtained results, which are presented in Figure 4.3, indicate that at low dwell times ($< 3\mu$s) the actuator is not able to accurately deliver the intended pulse and droplet ejection does not occur. Similarly, at very high dwell times ($> 16\mu$s) the ejection pressure is not sufficient for droplet formation and no droplets are ejected. Within this range of dwell times, single droplets without any satellites are ejected. Moreover, in the same range, both the droplet volume and the velocity initially increase, reach a peak value between 9 - 10$\mu$s and then fall. The volume changes in the range between 142 and 252 pL, while its maximum value occurs between $t_D = 9\mu$s and $t_D = 11\mu$s. The other curve indicates that the maximum value of the velocity equals to 1.98 m/s, which corresponds to $t_D = 9\mu$s, while its minimum value is 0.43 m/s. Therefore, one can conclude that both the maximum values correspond to two similar dwell times.

The parabolic shape of the curves can be explained based on the operation of the piezoelectric dispensers. When the sum of the rise and dwell periods equals to $l/c$,

the pressure wave is maximally amplified and, therefore, the drop is ejected with the highest force. However, if the sum deviates from the matching time, the negative wave is not completely neutralized and thus the magnitude of the amplified wave starts to decrease. Despite the reduction in the ejection force, droplets can still be generated, provided its value is higher than the surface tension force. If this condition is not satisfied, no droplets can be produced (see the dotted line in Figure 4.3 at $t_D = 16\mu$s).

Next, the same characterization was carried out for the silicone base. In this experiment the dwell time value was increased from $2\mu$s to $30\mu$s, and the other parameters were maintained constant: rise time - $7\mu$s, fall time - $12.5\mu$s, frequency - 300 Hz, voltage - 90 V.

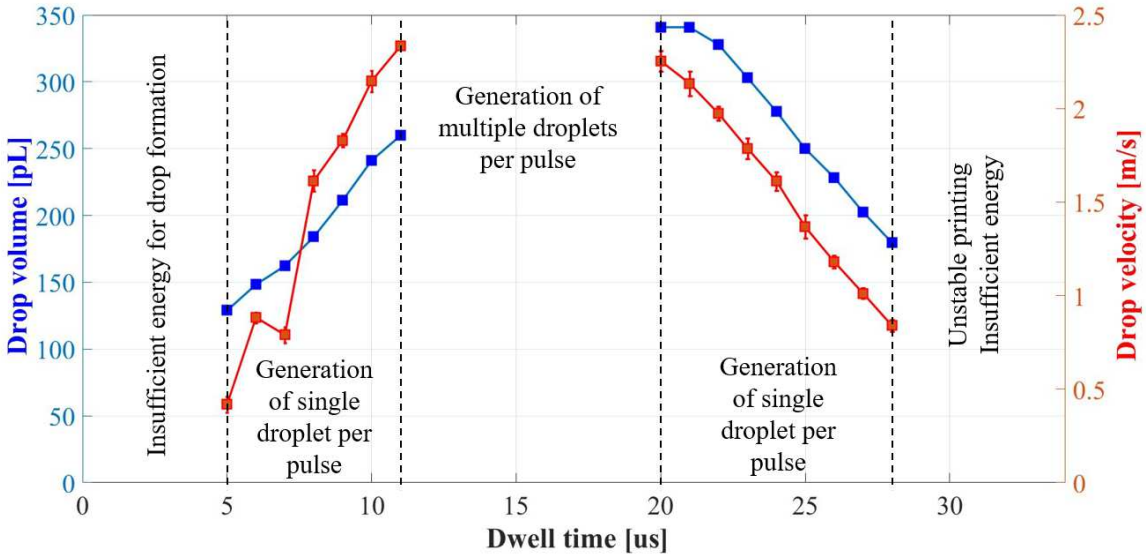


Figure 4.4: Both the volume and velocity of a drop, consisting of $A_1A_2D_4$, depend on the dwell time. Generation parameters: rise time - $7\mu$s, fall time - $12.5\mu$s, frequency - 300 Hz, voltage - 90 V.

The results as illustrated in Figure 4.4 shows somewhat similar behavior. At low dwell times ($< 5\mu$s) and at high dwell times ($> 28\mu$s), droplets are not ejected due to insufficient pressure generation inside the nozzle. However, droplets are generated

within these two dwell times. Interestingly, single droplet per pulse is only generated in some of the conditions while in others especially between 11 - 20$\mu$s a stream of drops is generated per pulse. The silicone base contains polymeric chains which can transmit stress over larger distances within the material. As a consequence, the polymeric solution requires a larger amplitude of the electrical impulse to eject a drop. Indeed, in our experiment the curing agent was ejected with an applied potential of 55 V, while the $A_1A_2D_4$ needs at least 90 V. The results presented in Figure 4.4 show two regions where single droplet per pulse is produced. One of those regions (between 5 - 11$\mu$s of dwell time) shows an increasing trend of the droplet volume and velocity with corresponding increase in the dwell time. The other region (between 20 - 28$\mu$s of dwell time) shows a decreasing trend of the droplet volume and velocity with corresponding increase in the dwell time. The region between them exhibits generation of multiple droplets per pulse and is not suitable for printing purposes. At $t_D$is lower than 5$\mu$s, the ejection force does not overcome the surface tension force and, therefore, the droplets are not produced. Beyond $t_D = 28\mu$s the pressure wave is dampened and only slightly larger than the surface tension holding the droplet back. Therefore, the momentum of the ejected droplets is small, and its path is significantly influenced by external factors that make its path unstable. In the stable printing regime, the velocity of the drop can be controlled between the interval between 0.418 m/s and 2.033 m/s, while its volume between 128.85 pL and 340.84 pL. In summary, $A_1A_2D_4$ is easier to control compared to 30% wt. glutaraldehyde in water with 20 ppm IPA, as the droplets can be generated in a bigger range of the dwell time. Furthermore, it also generates a wider range of droplet volume and velocity. However, there are certain regions where multiple droplets are generated per pulse and these have to be avoided for stable printing.

To explain the reasons for multidroplet printing that occurs between 11$\mu$s and 20$\mu$s

of the dwell time, one first need to understand how the liquid leaves the nozzle and creates a drop. Under the influence of the piezoelectric transducer, the liquid is first accelerated and then pushed out the nozzle which is graphically presented in Figure 4.2, and described in Section 4.1.

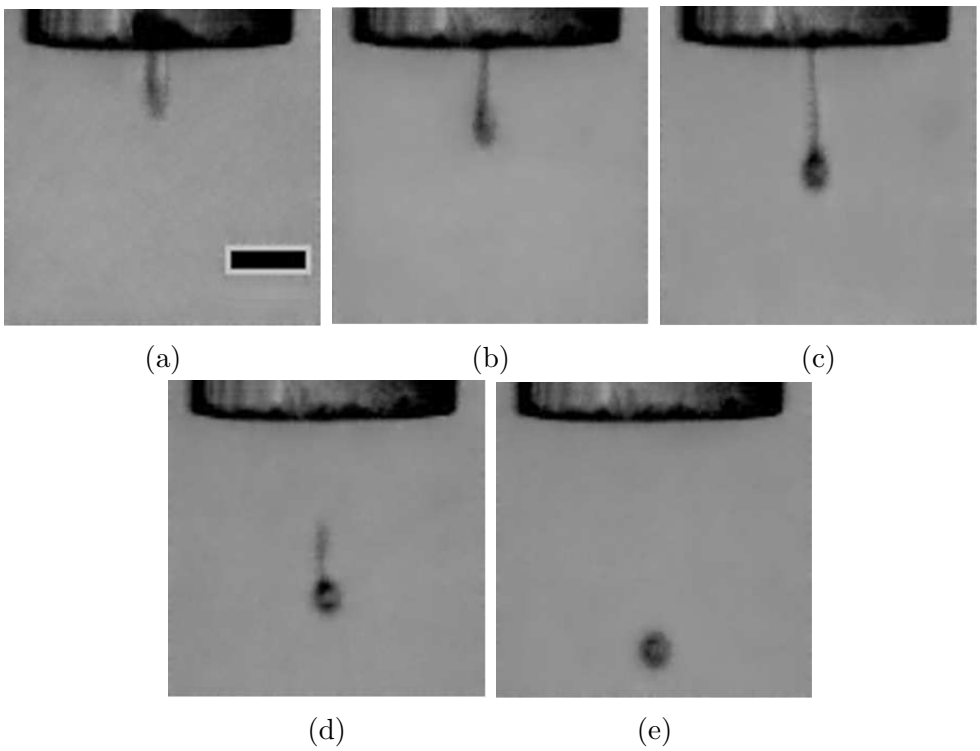


Figure 4.5: Generation of the drop of $A_1A_2D_4$ at dwell time - 6$\mu$s, rise time - 7$\mu$s, fall time - 12.5$\mu$s, voltage - 90 V, frequency - 300 Hz, Scale bar = 100 $\mu$m.

When the ink is pushed out, the meniscus quickly extends and creates a liquid column with a round head, as illustrated in picture (a) of Figure 4.5. The next picture, 4.5 (b), shows that, due to the decreasing flow rate from the dispenser, significant variations in the velocity distribution occur in the column, which forces it to stretch. Simultaneously, the surface tension acts to minimize the surface area of the column. Moreover, some ink is sucked back to the nozzle which is a consequence of the negative pressure created by the extension of the piezo element in the subsequent cycle. Due to these three reasons, at the tip of the nozzle the necking phenomenon occurs

(Figure 4.5 (c)), which leads to the pinch-off of the liquid thread (Figure 4.5 (d)). One can observe that the free liquid thread contracts and, under the influence of the surface tension, creates a stable drop as shown in Figure 4.5 (e). However, it is also possible that during the elongation of the liquid thread, the second neck, close to the bulbous head, occurs and progresses until the thread breaks up into two parts a primary drop and satellite (small drop). Both parts strive towards the spherical (equilibrium) shape, however in case of the latter, this phenomenon is more complicated. At the transitional stage, the free liquid thread contracts from both the top and bottom side which causes an oscillatory movement of the satellite. In some situations, however, the oscillation leads to the merging of the satellite and primary drop forming one large droplet. Both the above scenarios were observed for the dwell time values ranging between 5$\mu$s and 11$\mu$s as well as between 20$\mu$s and 28$\mu$s. However, between these two intervals one can identify another possibility, in which the satellite does not merge with the primary drop. The number of independent satellites depends on the applied voltage, since the liquid thread is further stretched when the voltage increases, and, at some point, it eventually becomes unstable. Hence, if the voltage is very low, only one independent satellite is formed. However, at higher voltage, the stretching of the liquid is accompanied by a wave-like instability along the thread. Afterward, the thread is subjected to a Plateau-Rayleigh instability, which, due to the presence of surface tension in the liquid, leads to minimize its surface area. Therefore, at the point where the capillary wave grows, one can notice inhomogeneous discontinuities in the thread structure and, in consequence, a formation of several satellites [58]. Because in the experiment with $A_1A_2D_4$ relatively high voltage was applied, multiple breakups occur in the dwell time range between 11$\mu$s and 20$\mu$s which is graphically presented in Figure 4.6.

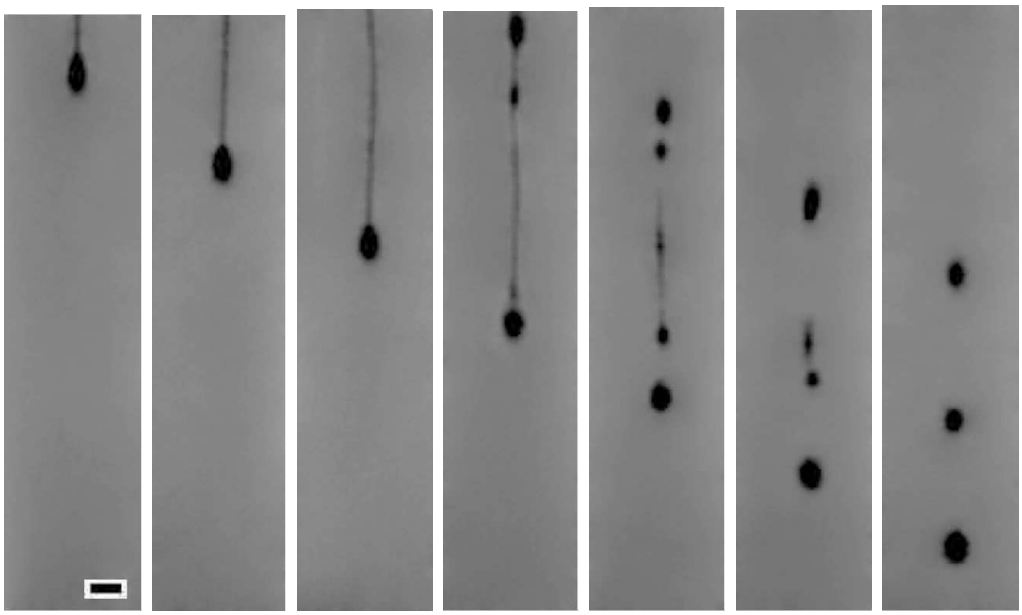


Figure 4.6: Multiple breakups of $A_1A_2D_4$ at dwell time - 15$\mu$s, rise time - 7$\mu$s, fall time - 12.5$\mu$s, voltage - 90 V, frequency - 300 Hz, time between the frames - 66.67$\mu$s. Scale bar = 50 $\mu$m.

Pictures (a-c) in Figure 4.6 illustrate the stretching of the liquid thread, which exhibits a bulbous head at the bottom end and it is attached to the nozzle, which is not visible in the picture. One can notice, based on these three pictures, that the liquid thread becomes thinner and more unstable as the elongation progresses. In picture 4.6 (d), one can see the pinched off thread, which is under the influence of the capillary wave instability. At the upper end, the surface tension contracts the liquid which leads to the formation of another bulbous head, and, as a consequence, it causes necking between this head and the rest of material. Additionally, below the newly created structure, another part of the thread is shrunk, and separated from both the top and bottom sides. The impact of the Plateau-Rayleigh instability is also visible right at the end of the long ligament, where the primary drop starts to separate. In picture 4.6 (e), one can observe that in the necking region the

liquid breaks up and, furthermore, the long thread, shown in picture 4.6 (d), starts shrinking into independent droplets in its central part. Based on pictures 4.6 (d) and (e), it was noticed that under the influence of the capillary wave, the liquid thread asynchronously disintegrates at several locations. Subsequently, Figure 4.6 (f) illustrates that the two upper drops merge, while the two bottom ones are still moving separately and the distance between them increases. However, the second upper drop is still in the formation process and moves quickly in an oscillatory manner. Finally, in picture 4.6 (g) one can identify three in-lined independent droplets. The bottom drop, with the largest diameter, was formed at the beginning of the ejection process and remained unchanged. However, the two other droplets were created during both the separation and joining process, and their diameter slightly decreased.

Although in the experiment the breakup process was observed only for the silicone base, this phenomenon is widely seen in Newtonian liquids. In general, liquids containing polymers chains, as opposed to Newtonian fluids, are capable of being stretched longer into an extended column before succumbing to the Plateau-Rayleigh instability. This result shows the propensity of such columns to breakup into a single drop rather than multiple droplets [59].

### 4.2.2 Effects of applied potential

The influence of the applied potential on both the volume and velocity of a generated droplet is significant, as it determines the glass tube deformation in the dispenser. If the amplitude of the electrical impulse is small, the volume of the glass tube slightly increases and, therefore, the resulting pressure wave is insufficient to prevail over the surface tension forces. Once the voltage is increased, the deformed tube impacts a larger volume of the ink and thus increases its velocity. However, when the applied

potential is too large, multiple droplets are ejected.

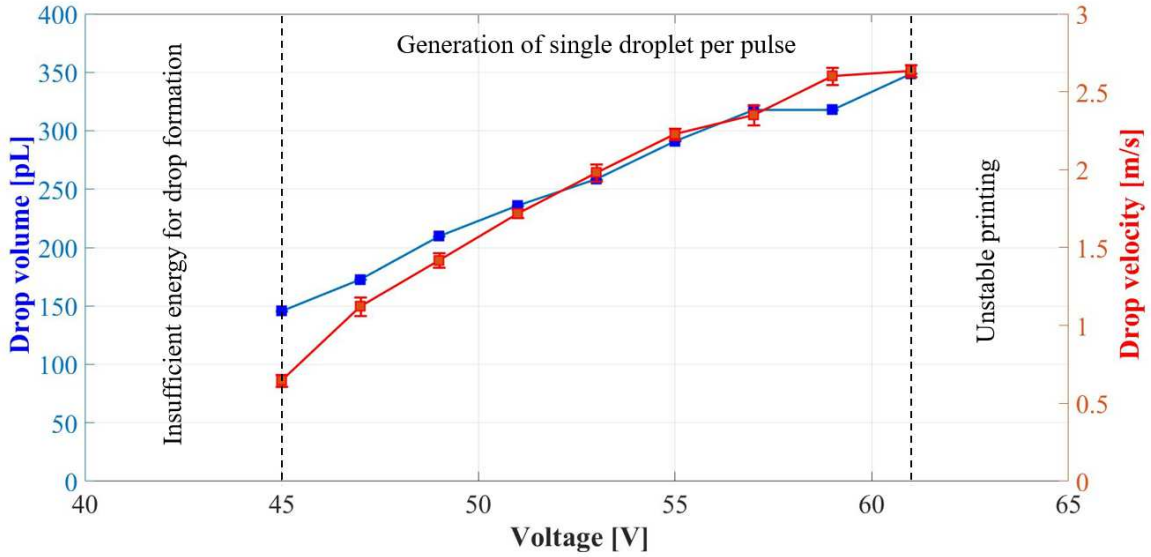


Figure 4.7: Both the volume and velocity of a drop, consisting of 30% wt. glutaraldehyde in water solution with 20 ppm IPA, depend on the voltage. Generation parameters: dwell time - 9$\mu$s, rise time - 7$\mu$s, fall time - 12.5$\mu$s, frequency - 300 Hz.

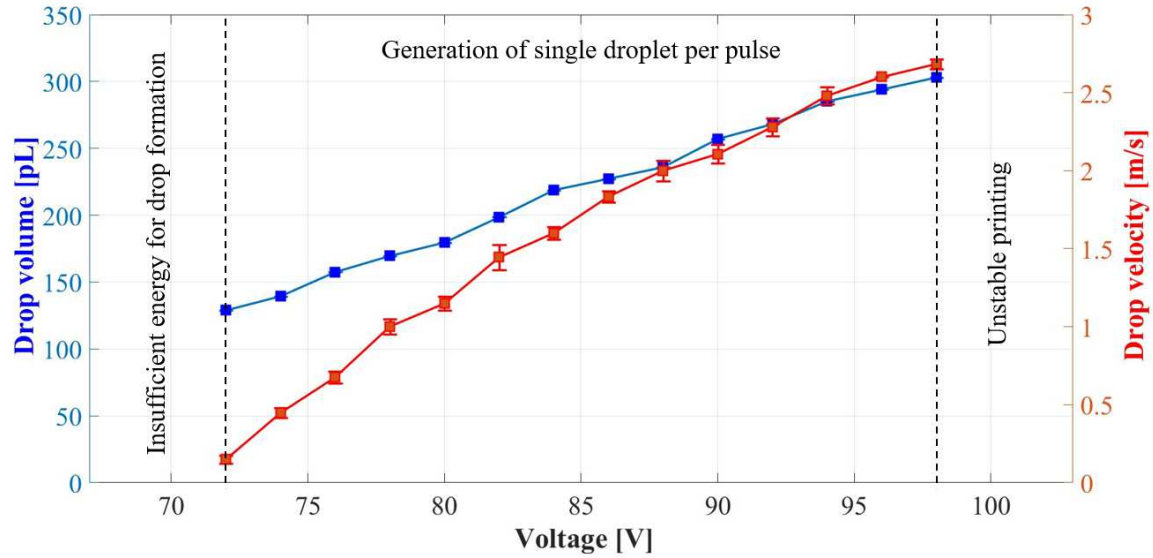


Figure 4.8: Both the volume and velocity of a drop, consisting of $A_1A_2D_4$, depend on the voltage. Generation parameters: dwell time - 9$\mu$s, rise time - 7$\mu$s, fall time - 12.5$\mu$s, frequency - 300 Hz.

In order to visualize this phenomenon, experiments with curing agent and silicone

base were carried out, in which droplets of both the substances were generated by applying the following parameters: dwell time - 9$\mu$s, rise time - 7$\mu$s, fall time - 12.5$\mu$s, frequency - 300 Hz, while the value of applied potential was gradually increased every two volts, from 43 V to 63 V for the curing agent, and from 70 V to 100 V for the silicone base. The results showing the dependence of the volume and velocity of the drop on the applied voltage are graphically presented in Figures 4.7 and 4.8 for the curing agent and silicone base, respectively. In both cases, the pulse width was unchanged during the experiment and, based on the result, one can infer that the relation between the applied voltage and parameters of the drop is linear. However, due to the differences in the properties of both liquids, the growth of the drop velocity and volume as well as the range of the applied potential values are different. Hence, in the droplet generation process of 30% wt. glutaraldehyde in water solution with 20 ppm IPA, a potential range from 45 V to 61 V can be used to have stable printing. The velocity of the droplet generated in this range is between 0.65 m/s to 2.63 m/s (a 306.5% increase), and the volume from 145.55 pL to 348.77 pL(a 139.6% increase). However, the potential range for $A_1A_2D_4$ guaranteeing stable printing is between 72 V and 98 V. In this range the velocity of the drop increases from 0.15 m/s to 2.68 m/s (a 1701.3% increase),while its volume increases from 128.86 m/s to 303.0 m/s (a 135.15% increase). In conclusion, one can notice that in both the experiments the change of voltage has a greater impact on the velocity rather than on the volume, which increases only by around 140% for both the materials. Moreover, one can conclude that in case of the curing agent the increase of voltage by 1 V leads to the increment in the velocity and volume by 0.12 m/s and 12.7 pL, respectively, and by 0.1 m/s and 6.7 pL for the silicone base. Therefore, one can infer that it is more convenient to regulate the velocity and volume of the silicone base in the proposed method,as the range of acceptable

voltage values is larger,and the droplet parameters are less sensitive to variations in the value of voltage, compared to that of the curing agent.

In the description of the working principle of the piezoelectric dispenser, only the primary pressure wave was considered. However, in practice, there are numerous secondary waves which also influence the fluid behavior inside the device. The residual oscillation will be described in detail in the next subsection, however, here the main focus is the droplet generation process when the applied potential is higher than in the stable regime. One can observe that higher the voltage, higher the amplitude of all the pressure waves in the dispenser. Thus, it is possible that the first secondary wave, with respect to the amplitude, is amplified such that it is able to overcome the surface tension force and, as a consequence, leads to the ejection of another drop. In the experiments the droplets made of 30% wt. glutaraldehyde in water solution with 20 ppm IPA were generated with the following parameters: dwell time - 9$\mu$s, rise time - 7$\mu$s, fall time - 12.5$\mu$s, voltage - 62 V, frequency - 300 Hz and the results are visualized in Figure 4.9.

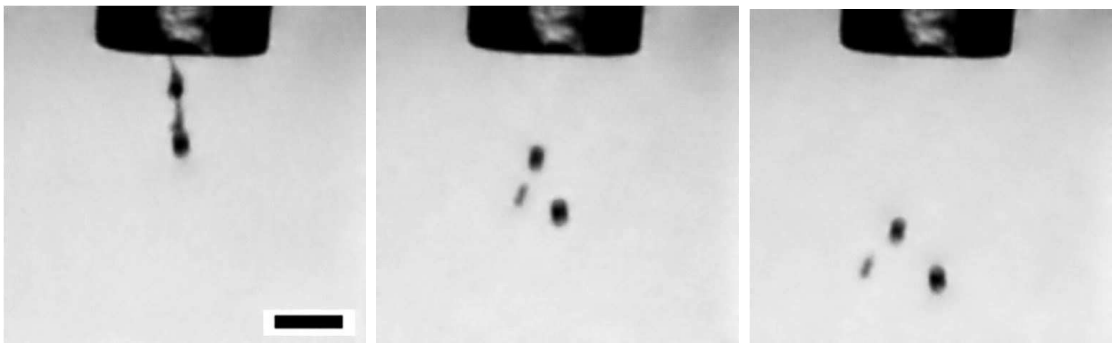

Figure 4.9: Phenomenon of ejection of droplets under the influence of too high voltage value. The droplet consisting of 30% wt. glutaraldehyde in water solution with 20 ppm IPA. Generation parameters: dwell time - 9$\mu$s, rise time - 7$\mu$s, fall time - 12.5$\mu$s, voltage - 62 V, frequency - 300 Hz. Scale bar = 100 $\mu$m.

At the beginning, one liquid thread with a bulbous head is dispensed. However, before the thread is pinched off from the nozzle, another portion of the material is

ejected. Subsequently, the head from the first ejection breaks up, its tail changes into a satellite, and the liquid portion from the second dispersion forms a drop. Therefore, instead of one droplet, two large droplets with one satellite are obtained, which is not suitable in a printing process.

### 4.2.3 Effects of rise time

In order to visualize the dependence between the rise time, and the volume and velocity of the ejected droplets, an experiment with curing agent and silicone base was conducted. In case of 30% wt. glutaraldehyde in water solution with 20 ppm IPA, the value of rise time was increased from 2$\mu$s to 18$\mu$s, while the other parameters of electrical impulses were maintained constant, namely the dwell time was equal 9$\mu$s, fall time - 12.5$\mu$s, frequency - 300 Hz, and the value of applied potential was set to 55 V.

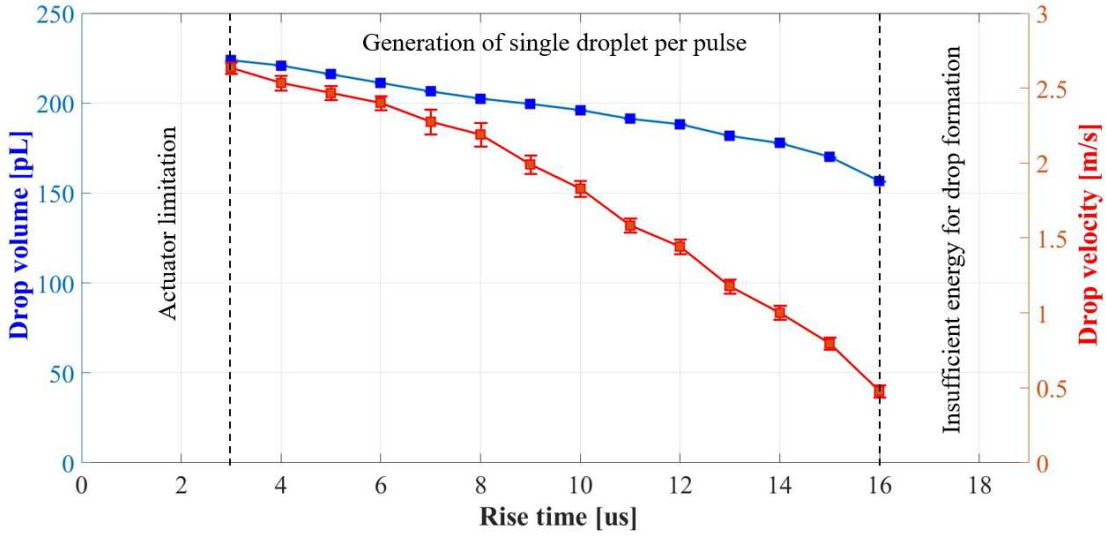


Figure 4.10: Both the volume and velocity of a drop, consisting of 30% wt. glutaraldehyde in water solution with 20 ppm IPA, depend on the rise time. Generation parameters: dwell time - 9$\mu$s, fall time - 12.5$\mu$s, voltage - 55 V, frequency - 300 Hz.

The obtained results, as shown in Figure 4.10, demonstrate that at low rise times

($< 3\mu$s) the actuator is not able to deliver a sufficient electrical pulse to the piezo actuator and therefore, droplets were not ejected. Similarly, at very high rise times ($> 16\mu$s), the ejection pressure is not sufficient to generate droplets. Within this range of rise times, single droplets are ejected, and both the droplet volume and the velocity decrease. In this range, the volume changes between 223.85 pL and 156.6 pL (a 42.9% decrease) and the velocity from 2.64 m/s to 0.48 m/s (a 451% decrease) as the rise time increases. The rise time is a period, in which the amplitude of the impulse increases, and thus the glass tube expands. Theoretically, if the time is long, the energy from the capillary expansion slowly converts to the kinetic energy of the liquid, and part of it dissipates. If this period is short, on the other hand, the energy transduced into the oscillating liquid in the capillary is less dissipative, which means the pressure wave is built more efficiently [60]. The theoretical results depicted in Figure 4.10 correspond to the curing agent, for which the measured parameter values decrease as the rise time increases.

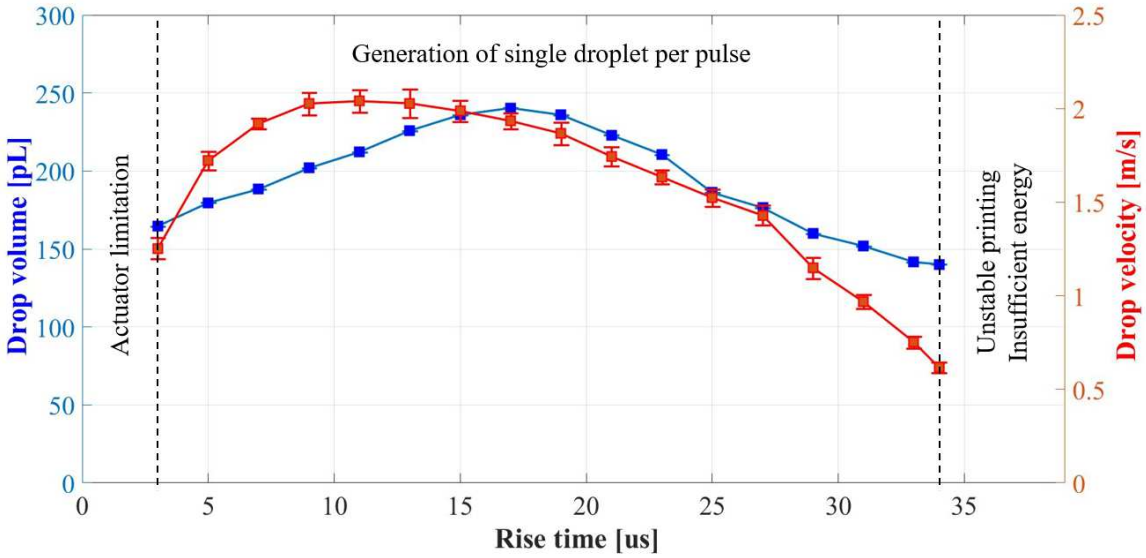


Figure 4.11: Both the volume and velocity of a drop, consisting of $A_1A_2D_4$, depend on the rise time. Generation parameters: dwell time - 9$\mu$s, fall time - 12.5$\mu$s, voltage - 90 V, frequency - 300 Hz.

In the experiment with $A_1A_2D_4$, the rise time value was increased every two $\mu$s, from 2$\mu$s to 36$\mu$s, and the remaining parameters of applied electrical impulses were kept constant, i.e. dwell time - 9$\mu$s, fall time - 12.5$\mu$s, voltage - 90 V, frequency - 300 Hz. From the collected results, which are shown in Figure 4.11, one can observe that, if the value of rise time is both smaller than 3$\mu$s and larger than 34$\mu$s, droplets cannot be seen. Inside these limits, i.e. between 3$\mu$s and 34$\mu$s, single droplets can be printed, and the magnitude of their volume and velocity initially increase, reach a peak and then fall. The volume varies in the range between 140.14 pL and 240.37 pL, while its maximum value corresponds to $t_R = 17\mu$s. The velocity curve has its minimum at 0.62 m/s and maximum at 2.04 m/s. The latter extremum corresponds to the rise time in the range $t_R = 9$ - 13$\mu$s. The velocity and volume curves exhibit a parabolic shape, however, their peak points do not coincide which might be caused by the measurement error of the droplets ejected with the maximum velocity.

Based on the comparison of the results for curing agent and silicone base, shown in Figures 4.10 and 4.11, respectively, one can observe that the ejected droplets exhibit different behaviors for both the materials. Based on the geometric characteristics of the curves, one can infer that for each material there exists an optimal value of the rise time, after which both the volume and velocity decrease. The critical value of the rise time is inseparably related with the properties of the applied materials, especially with the speed of sound in these materials. If this quantity increases, the optimal rise time reduces, and vice versa. Although the sound speed is not known for our materials, its value was estimated using the formula $c = l/t$, which is included in Figure 4.2. The equation combines the speed of sound c, and length of the dispenser l, and time t, during which the ejection pressure wave is maximally amplified, leading to the generation of a droplet with maximum velocity and diameter. Since some of the information required to calculate the speed of sound from the formula is

unknown, the experimental data was used instead. Based on the results from 4.3 and 4.11, the speed of sound for the curing agent was approximated to be 1165 m/s, while for the silicone base 990 m/s. Therefore, the silicone base requires more time to build a pressure wave with the maximum possible amplitude which explains the difference in the geometry of the curves for both materials.

### 4.2.4 Effects of fall time

In contrast to the rise time, the fall time is a period in which the glass tube returns from the expanded to neutral position and therefore, the built pressure is amplified. In the experiments, the value of fall time was increased from 2$\mu$s to 9$\mu$s for curing agent, and from 2$\mu$s to 37$\mu$s for silicone base. The remaining parameters, on the other hand, were set to constant values, i.e. dwell time - 9$\mu$s, rise time - 7$\mu$s, frequency - 300 Hz, voltage - 55 V for glutaraldehyde solution, and 90 V for $A_1A_2D_4$.

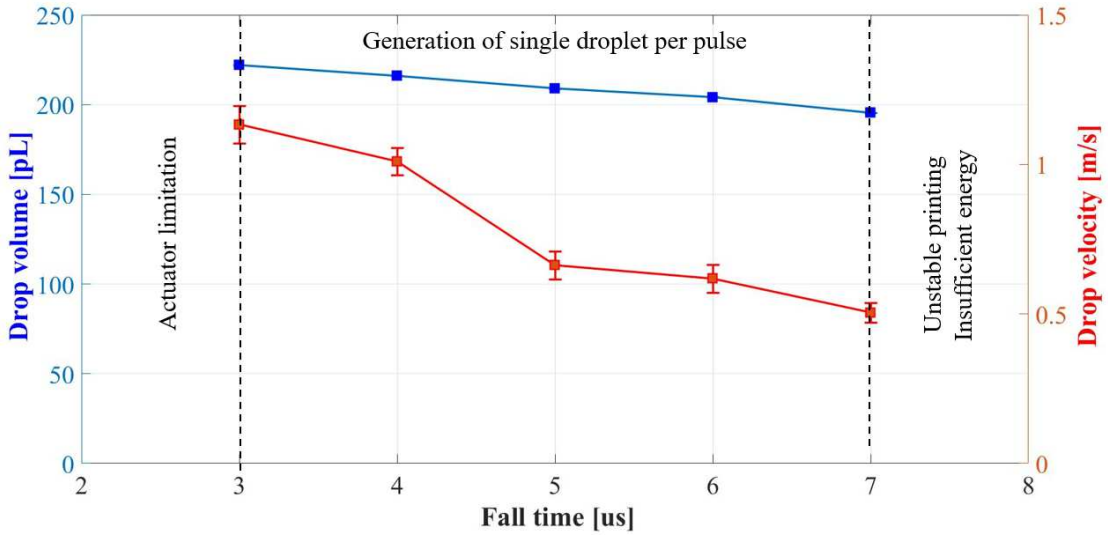


Figure 4.12: Both the volume and velocity of a drop,consisting of 30% wt. glutaraldehyde in water solution with 20 ppm IPA, depend on the fall time. Generation parameters: dwell time - 9$\mu$s, rise time - 9$\mu$s, voltage - 55 V, frequency - 300 Hz.

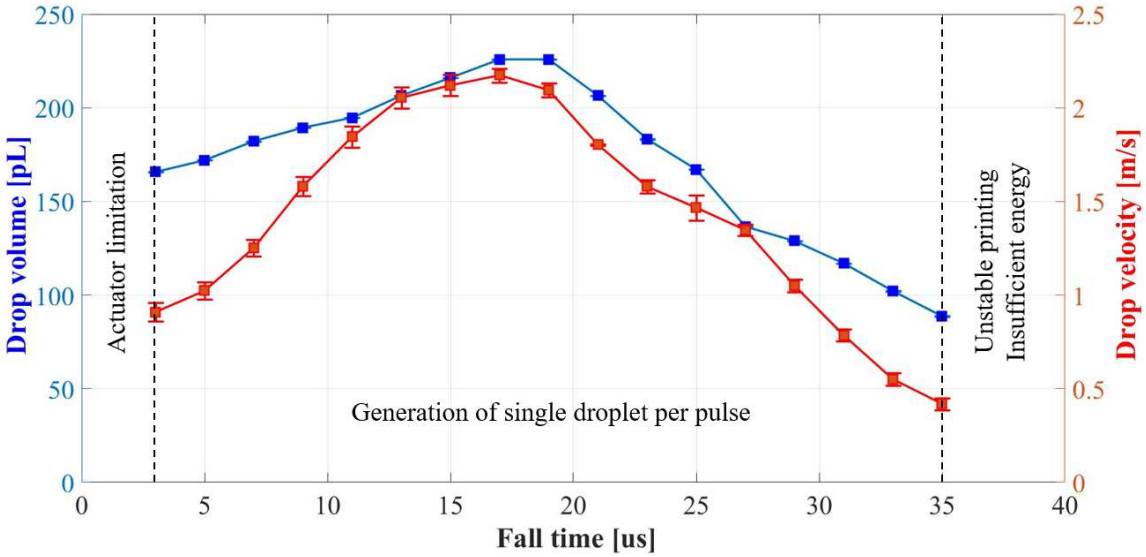


Figure 4.13: Both the volume and velocity of a drop,consisting of $A_1A_2D_4$, depend on the fall time. Generation parameters: dwell time - 9$\mu$s, rise time - 7$\mu$s, voltage - 90 V, frequency - 300 Hz.

The impact of fall time on both the velocity and volume of the drop is presented in Figures 4.12 and 4.13 for the curing agent and silicone base, respectively. One can observe that the dependence of the velocity and volume on the fall time is analogous to that of the rise time (compare with Figures 4.10 and 4.11). In case of small values of fall time ($< 3\mu$s), the initiating signal is not properly delivered to actuators, and, therefore, droplets are not ejected. For high values of fall time ($> 7\mu$s for curing agent or $> 35\mu$s for silicone base), the generated pressure inside the nozzle is not sufficiently large to print droplets. Between 7$\mu$s and 35$\mu$s, both the volume and velocity of a drop made of curing agent decreased with the increase of the fall time. The volume reduces from 222.03 pL to 195.43 pL (a 13.61% decrease), and velocity from 1.13 m/s to 0.51 m/s (a 124.69% decrease). However, both the volume and velocity of the silicone base droplets initially increase, reach their peak at $t_F = 17$ - 19$\mu$s and then fall. The volume varies between 88.71 pL and 225.84 pL (a 154.59% change), and velocity from 0.42 m/s to 2.17 m/s (a 418.85%, change).

In general, at the lower value of fall time the energy transfer for the actuators to materials is more focused, than at its larger value, which results in a higher amplitude of the pressure wave. Therefore, the velocity and volume of the drop of curing agent, as presented in Figure 4.12, decrease as the fall time value increases. However, there is an optimal value of the fall time, which is determined by the speed of sound in the material, before which the droplet parameters increase with the fall time, but beyond that these two quantities decrease. Based on Figure 4.13, one can infer that the optimal value of fall time for silicone base is in the range $t_F$ = 17 - 19$\mu$s.

### 4.2.5 Dimensional Analysis of Printed Droplets

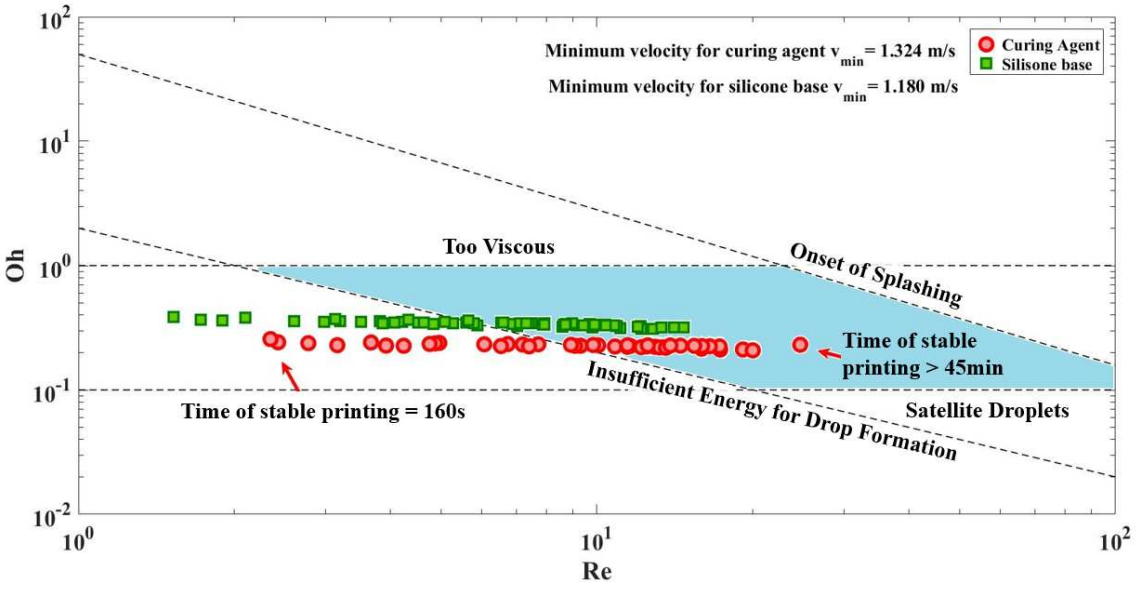


Figure 4.14: Results of 30% wt. glutaraldehyde in water solution 20 ppm IPA and $A_1A_2D_4$ presented as a dependence of the Ohnesorge number (Oh) and Reynolds number (Re), with the specified area of stable printing (blue area).

All the data presented in the figures above were analyzed using the stable printability theory, which is described in detail in Section 3.2.2. For this purpose, the results

were expressed in terms of the nondimensional numbers, Oh and Re, and presented in Figure 4.14. The stable printing area, marked by blue color, is limited by lines representing the equations 3.6 - 3.9 and the range $10 > Z > 1$. These limitations are associated with both the splashing and satellite droplets phenomena, as well as the restrictions of the actuators, which can generate insufficient ejection energy, or undesired liquid properties, such as too high viscosity. In Figure 4.14, the conditions were stable printing was observed for silicone base data is marked by green square, while those for curing agent is marked by red circles. Based on the results in 4.14, one can infer that observed results satisfy the three conditions of stable printing. All the stable printing conditions are between $0.1 < Oh < 1$ or between the *too viscous* and *satellite droplet* generation regime. It is also well below the *onset of splashing* threshold. However, it was noticed that some stability in printing was observed even below the threshold for insufficient droplet formation. Nevertheless, it was observed that those conditions that fall outside the stable printing zone which is marked in blue in Figure 4.14 were only able to stably print for a short duration of time (few 100s of sec). On the other hand, those conditions that fall within the stable printing zone were capable of sustained stable printing over very large duration of time (few tens of min). The onset of instabilities after a few minutes is surprising, since the largest resistance induced on the generated drop occurs at the beginning of the printing process. However, it should be noted that at the beginning of every experiment, the glass nozzle is wiped, which means that the tip of the nozzle was initially dry, and the created meniscus of liquid was small, which resulted in low resistance of the ejected droplets. However, when the meniscus achieved its optimal size, the surface tension force turned out to be too large hindering the droplet generation. Based on equation 3.7, the minimum velocity of the drop which guarantees its stable and long printing was calculated. Its minimum value is 1.324 m/s and 1.180 m/s for

the applied curing agent and silicone base, respectively. One can notice that these two values approximately equal to a half of the maximum velocity of the drop.

The calibration process was performed using only one kind of curing agent and silicone base, because other materials that were considered in the experiments have comparable properties. Based on the results presented in Figures [4.3, 4.4, 4.7, 4.8, 4.10, 4.11, 4.12, 4.13], one can observe that the silicone base requires a larger dwell time and a higher potential to be in the stable droplet generation regime as compared to the curing agent. In general, both the velocity and volume of an ejected silicone base droplet can be controlled over a wider range of relevant parameters. However, an exception to this rule is the velocity measured in the experiment with the rise time. What is more, the growth of the measured parameters, with respect to the change of either the pulse width or voltage by one unit, is smaller in case of the silicone base. Therefore, based on these three conclusions,one can infer that in the merging droplet experiment, the parameters of a silicone base drop will be adjusted to the ones of the curing agent, as they can be accurately controlled in a larger range and with a smaller increment.

## 4.3 Residual oscillations

After the droplet ejection, the ink that remained in the printhead channel is excited by residual oscillations that follow the initial pressure waves. An example of such oscillations has been shown elsewhere and is reproduced here [26], which continued to propagate through the printhead channel after the ejection. These oscillations that continue to propagate in the printhead channel even after droplet ejection, are damped over a period of time.

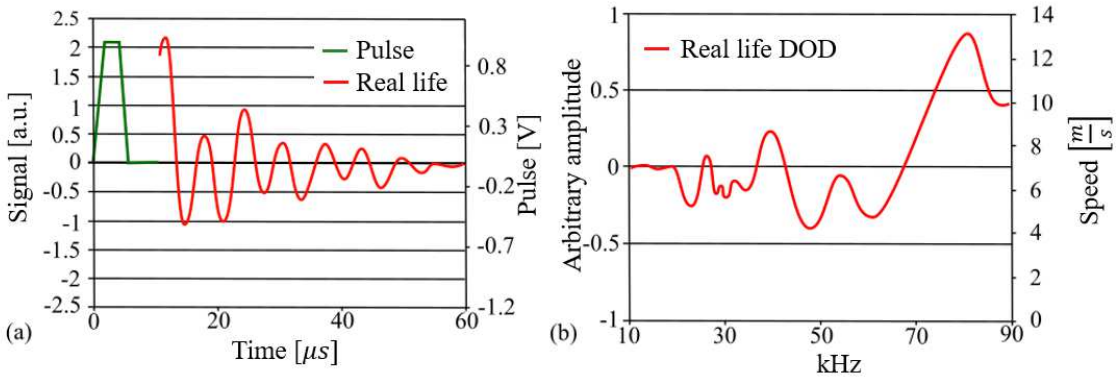


Figure 4.15: Residual oscillations in a channel. Electrical signal applied to the piezoelectric element ((a) - green line). Residual oscillations measurements presented with respect to time t ((a) - red line) and with respect to the time reciprocal 1/t (b) [26].

According to Figure 4.15 (a), it is clear that the excitation dies out after at a time frame (60$\mu$s in this example) that is several times the time required to ejected the drop. It means that the next electrical impulse should not be imposed before that time in order to avoid the influence of the secondary oscillations. It is acceptable that 5% of the pressure oscillation from the previous drop can be present in the subsequent ejection. However, if the piezoelectric element is activated before the residual oscillations damp to 5%, the pressure in the channel varies and, as a consequence, the dispensed droplet has a different volume and velocity compared to the previous one. This effect has also been demonstrated previously and can be visualized on a plot with either the drop speed or its volume as a function of the ejection frequency. In Figure 4.15 (b), the left axis represents the droplet speed variation. One can notice that the velocity varies (from 4 m/s to 13 m/s in this case) if the residual oscillations are undamped and a single trapezoidal impulse is applied. To increase the ejection frequency while maintaining the uniform drop parameters, the actuating electrical impulse should be properly modified.

In general, the damping time of residual oscillations depends on both the dispenser

geometry and material properties. The minimum time between the ejection of two consecutive droplets, or the maximum jetting frequency, can be calculated based on the following formulas:

$$t_{min} = \frac{\pi}{\varsigma\omega_n}, f_{max} = \frac{\varsigma\omega_n}{\pi}[61], \tag{4.1}$$

where $\varsigma = \frac{K}{2\sqrt{MC}}$ and $\omega_n = \sqrt{\frac{C}{M}}$ denote the damping ratio and the natural frequency of the system, respectively 4.1. One can solve equations 4.1 using geometry parameters of the channel; L - nozzle length, A - nozzle cross section area, V - volume of a chamber; liquid properties; $\rho$ - density, $\eta$ - dynamic viscosity, $c$ - speed of sound in the ink; and other fundamental dependencies, including $M = \rho AL$, $K = 8\pi\eta L$, $K_b = \rho c^2$, $C = \frac{K_b A^2}{V}$.

In our experiments, however, the dispensing devices feature more complex shapes, compared to the simplified model with the uniform diameter of the nozzle. Theoretically, one can assume the nozzle body diameter to be constant, and equal to the minimum diameter of the nozzle, namely 80 $\mu$m. Thus, the maximum frequency in case of the curing agent (30% wt. glutaraldehyde in water solution with 20 ppm isopropanol) and silicone base ($A_1A_2D_4$) is 9.16 kHz and 12.10 kHz, respectively. However, assuming there are no tapers and the diameter of the nozzle is equal to 500 $\mu$m, these two frequency values respectively reduce to 234.6 Hz and 309.8 Hz. The difference between results from both measurements are large and none of them determines the actual residual oscillation time in the used dispenser. To verify the results corresponding to low values of frequency, an experiment with $A_1A_2D_4$ and 30% wt. glutaraldehyde in water solution with 20 ppm IPA was carried out. In the experiment, only the ejection frequency increased every 50 Hz, starting from 50 Hz to 500 Hz, while the remaining parameters of the applied impulse were constant.

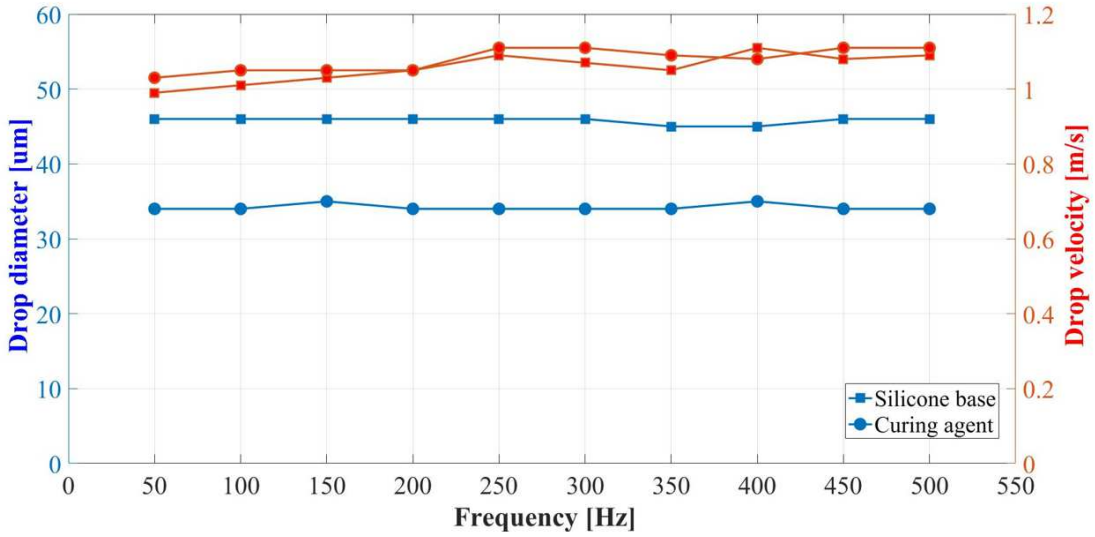


Figure 4.16: Measured diameter and velocity of an ejected drop for different values of jetting frequency.

Based on the results presented in Figure 4.16, one can observe that the diameters of droplets did not change significantly. They were approximately equal to 45.8 $\mu$m and 34.2$\mu$s for silicone base and curing agent, respectively, while their variations were noticed to be very small, 0.42$\mu$s for both the materials. The velocity also maintained a stable value 1.06 m/s for $A_1A_2D_4$ and 1.08 m/s for glutaraldehyde, with the deviation of 0.04 m/s and 0.03 m/s, respectively. Therefore, one can conclude that both the diameter and velocity of the ejected drop do not change if the frequency is less than 500 Hz. These results clearly show that the frequency calculated under the assumption of the diameter to be equal to 500 $\mu$m involve an error. However, since the second assumption, with the diameter equal to 80 $\mu$m, was not verified under the real condition, one cannot unambiguously assess these results. However, it is predicted that the maximum value of the frequency allowing to damp the residual oscillation is lower due to the changing geometry of the nozzle. Hence, the actual value of the residual oscillations time should be between the two calculated extrema.

## 4.4 Collision of Droplets

The next step after droplet generation is to enable intersection of the path of the silicone and the curing agent droplets and allow them to meet and merge with each other. The phenomenon of droplet in-flight collision is well-understood and its consequences are precisely described in the literature. In general, if two drops meet in free space, they can bounce, merge permanently, coalesce temporarily with disruption, or merge temporarily with fragmentation. There four scenarios are visualized in Figure 4.17.

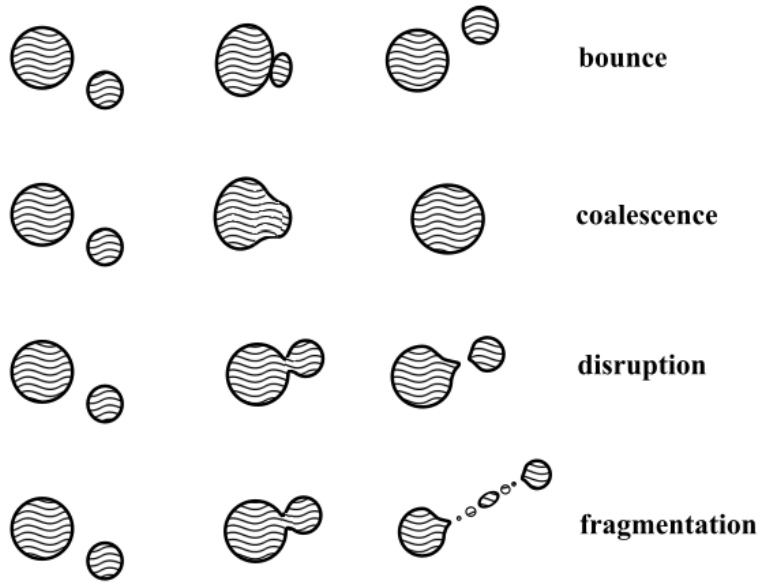


Figure 4.17: Four possible phenomena occurring after a collision of two droplets [62].

The result of the droplet collision depends on liquid properties (i.e.the viscosity and surface tension), viscosity and density of the surrounding gas, and the droplet aspect ratio. However, the most important factors influencing the collision mechanism are the Weber number (We), described by equation 3.5, and the parameter b, which is defined as the distance between the geometric centers of two drops with respect to

the vertical axis. The value of b can vary between 0 and the sum of the radii of two drops.

The bounce phenomena occur when the surfaces of two free-flying droplets do not contact with each other due to the presence of the intervening layer of a gas between them. It can happen when their velocities (or, equivalently, their kinetic energy) are very low. In the space between the drops, the pressure is built up, which leads to the flattening of the drop surface. Therefore, a fraction of the kinetic energy is expended in creating new surface and thus the impact kinematic energy decreases to the value, which is insufficient to overcome the gas barrier.

The permanent droplet coalescence is possible only when the Weber number is slightly larger compared to the previous case, and the kinetic energy of the droplets is sufficient to push the gas layer out of the space between them and merge. Subsequently, if the kinematic energy, is smaller than the surface energy of a newly created drop then the merged drop stays as one. Therefore, the merged drop, whose volume is equal to the sum of the volumes of pre-collision droplets, oscillates until a stable spherical shape is achieved.

There essentially exists two reasons for the temporary coalescence of a drop. First, when the kinetic energy exceeds the surface tension energy (We is high), and, simultaneously, the value of the parameter b is close to zero. In this case, after the collision, two droplets coalesce and start to oscillate. Due to the high inertial forces, the surface tension is not sufficient to suppress the oscillations and, therefore, the merged drop disintegrates into two smaller ones. Additionally, if the Weber number is high enough, the two resulting droplets are connected together by a filament, which eventually breaks and forms a few satellites. Second, if the parameter b is non-zero, a fraction of the kinematic energy is converted into rotational energy. Depending on the value of b, the contact area of the connected droplets changes.

The surface tension, resulting due to the interactions between molecules of the two substances, leads to the merging of droplets. However, the movement of the part of a droplet away from the contact surface is driven by the kinetic energy which causes the separation of the partially merged droplet. If the value of b increases, the separation forces prevail over coalescent forces, and, in consequence, the temporarily merged droplet breaks apart into two or more smaller drops [63].

In our experiments, the droplet collision is an even more complex phenomenon that the scenario described above as two chemically different substances interact and react with each other after contact. The materials have different physical properties, such as the surface tension and viscosity, and, therefore, it is required to adjust the parameters of electrical impulses separately for each of them, to ensure an efficient ejection. As a consequence, it is very difficult to jet two droplets having the same diameter and velocity. Nevertheless, the goal is to minimize the difference between the parameters of the drops by controlling the electrical signals, in order to mix them in the desired ratio of 1 to 1. Moreover, it is important that after the collision, the merged drop falls vertically down onto a substrate, thus the momenta (i.e. the velocity magnitude) of the two drops must be identical. What is more, the hydrophobic curing agent repel the hydrophilic silicone base which increases the probability of either bouncing or disruption after the collision. On the other hand, these two materials undergo very fast chemical reactions, which can facilitate merging.

In the experiments, 50% glutaraldehyde in water and DMS-A11 are utilized. Both droplets made of these materials were ejected with similar velocities, between 0.93 m/s and 1.07 m/s, and the diameters of the curing agent and silicone base were equal to 32 $\mu$m and 36 $\mu$m, respectively. Because the main focus here is the permanent droplet coalescence phenomenon, the relevant parameters (the velocity, droplet di-

ameter and parameter b) are set to be in the coalescence regime. Figure 4.18 shows different behaviors of merged droplets, depending on the parameter b, which varies between 0 $\mu$m and 34 $\mu$m, to enable the collision. In picture 4.18 (a), the value of b is almost zero and the two droplets approach each other centrally, and very quickly, after around 25$\mu$s from the contact, they form a stable spherical drop. However, in picture 4.18 (b), the distance between the centers of the drops equals 8 $\mu$m. Therefore, after the contact, the resulting droplet flattens and rotates by around 90° before it achieves the equilibrium state, which takes place after around 125$\mu$s. Snapshot 4.18 (c) visualizes the behavior of the merged droplet when the parameter b is increased to 26 $\mu$m, i.e. to the 76% of its maximum value. In this case, the coalescent drop spreads into a disc. The impact of inertia forces is more significant because the surface tension forces require more time (around 220$\mu$s) to contract back the disc towards the center of mass of the drop and form a spherical shape. Moreover, in this case a significant fraction of the impact kinetic energy is converted into the rotational energy, and, therefore, the coalescent drop rotates by 270°. If the parameter b is further increased to 32 $\mu$m, the impact of inertia forces on merged droplets is stronger, which is shown in picture 4.18 (d). The drop needs at least 500$\mu$s to form a stable droplet, and within this period of time it rotates by around 630°. Based on this experiment, one can infer that, despite different properties of the applied materials, the permanent coalescence occurs if b is in the range between 0 and 94% of its maximum value. Beyond this range, the merging droplets could not be observed.

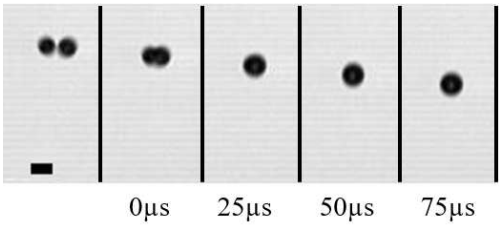


(a) b = 0 $\mu$m

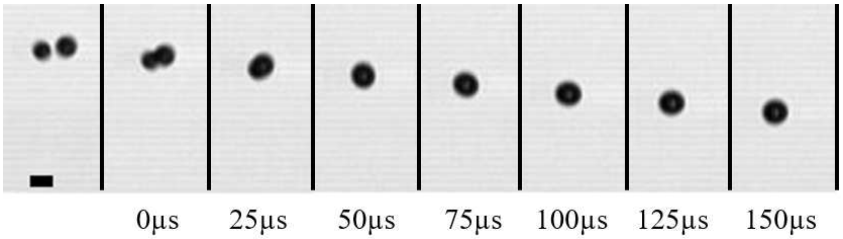


(b) b = 8 $\mu$m

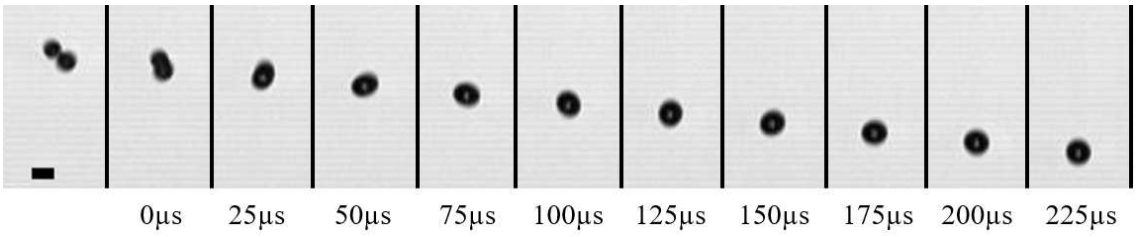


(c) b = 26 $\mu$m

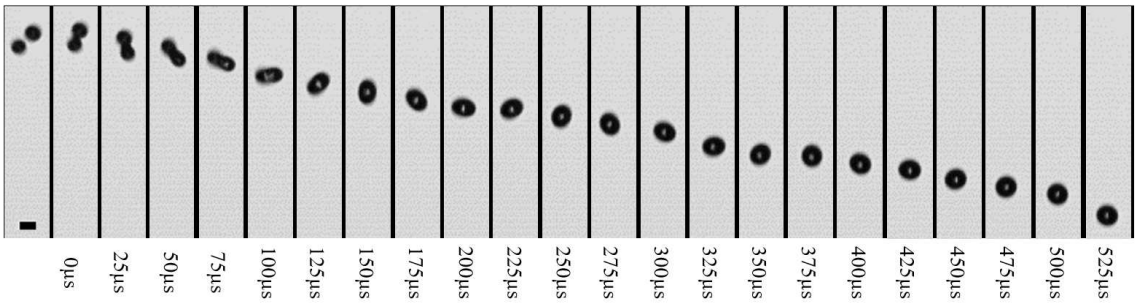


(d) b = 32 $\mu$m

Figure 4.18: Four scenarios of permanent droplet coalescence, depending on the b parameter: b = 0 $\mu$m (a), b = 8 $\mu$m (b), b = 26 $\mu$m (c), b = 32 $\mu$m (d). The diameter of the left-hand side drop (curing agent) is 32 $\mu$m, while the diameter of the right-hand side one (silicone base) is 36 $\mu$m, and their velocities vary from 0.93 m/s to 1.07 m/s. Scale bar = 50 $\mu$m.

## 4.5 Stability of printing process with the integrated free space droplet mixing approach

It is required that any modification of a 3D inkjet printer preserves the capability of long and stable printing. In the proposed method, a droplet mixing approach in free space between the dispensers and substrate is implemented and in the light of the above requirement, one must ensure that the droplet mixing process is stable. Indeed, the mixing is the most sensitive part in the whole printing process. It can be affected by many factors, for example, by a completely or partially clogged dispenser, which can either change the trajectory of droplets or stop the ejection. To eliminate this problem, the materials were filtered using a 5-micron pore size filter before use. Additionally, the dispensers were rigidly mounted to the holders which are set apart keeping a safe distance between them to avoid unintentional contact and reaction at the nozzle tips. Furthermore, the 3D printer was covered on 3 sides to minimize any convection of surrounding air and its impact on the droplet trajectories. It was also observed that the movement of the printhead had a significant effect on the accurate alignment between the two nozzles. The nozzles were spatially misaligned very quickly due to sudden changes in direction and speed as part of the printing process. Therefore, the printer was redesigned so that the printhead was made stationary and mechanically isolated from the movement of the stage.

To prove that the free space mixing approach does not hinder the printing process, an experiment with the modified 3D printer was carried out using both 50% glutaraldehyde in water and DMS-A11. During the printing, the XYZ positioner was placed in a relatively large distance from the dispensers to eliminate the potential influence of electrostatic forces and images of the droplets were recorded every five minutes for an hour using the camera ($Fastec\ Imaging\ TSHRMS$) high-speed

camera. Figure 4.19 shows the measured diameter and velocity of droplets of the base curing agent and PDMS over a period of 1 hour. The results are obtained from the measurements that were repeated five times separately for each material in each cycle, to ensure repeatability.

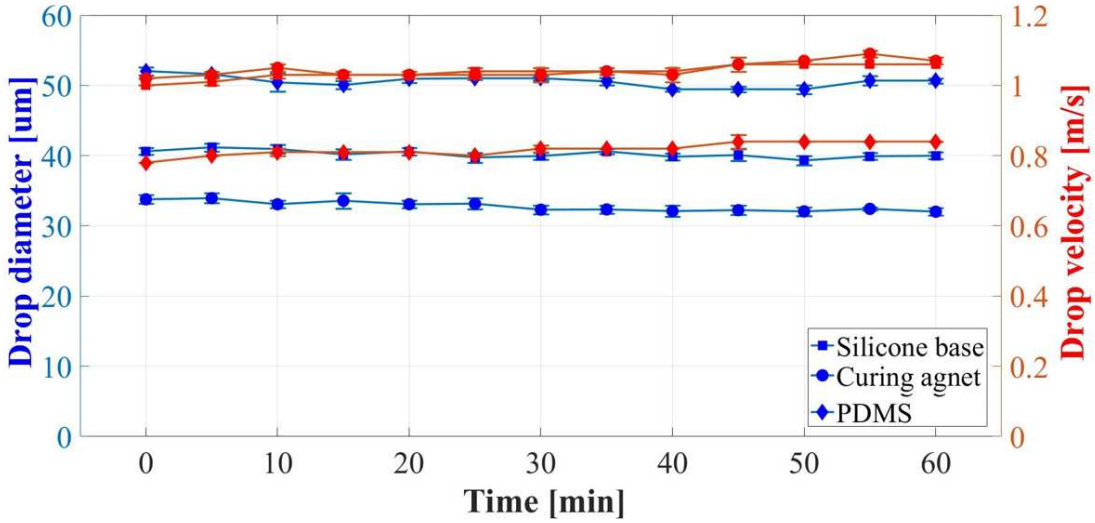


Figure 4.19: Diameter and velocity of drops made of the silicone base, curing agent, and PDMS as functions of the printing time.

The diameter of droplets of each material was stable and equal to 40.22 $\mu$m for silicone base, 32.78 $\mu$m for curing agent, and 50.57 $\mu$m for PDMS, and only a small change of 0.52 $\mu$m, 0.69 $\mu$m, and 0.81 $\mu$m, respectively, was observed. The velocity also maintained a stable value, 1.04 m/s for silicone base, 1.05 m/s for curing agent and 0.82 m/s for PDSM, with the unnoticeable variation of 0.02 m/s for each material. Based on Figure 4.19, one can conclude that both the parameters for each material remain constant for an hour. Moreover, in other experiment, that was carried out without a high-speed camera, stable mixing persists for more than four hours. Hence, both Figure 4.19 and observations from the experiments unambiguously prove that the free space mixing approach enables stable and long printing.

### 4.5.1 Impact of electrostatic forces on the mixing process

Since the dispensed droplets are very small, environmental conditions such as convection and even electrostatic interactions could have a significant effect on their trajectories. Droplet ejection process by itself is known to inject charges into the droplet. This is more prominent in dielectric materials such as silicones. Water based materials, on the other hand, are polarizable. Both these materials could be affected by any external electric field that may be present in the vicinity. Such electric field could be generated due to inadvertent charging of dielectric substrates (such as glass) on which printing is done.

To investigate the impact of such electrostatic forces arising from the substrate on the droplets during the mixing, a printing process with a charged substrate (glass) placed close to the merging site and far away from it was performed, and the characteristics of the droplet merging process were measured. In the experiment, when the distance between the dispensers and substrate was large (four centimeters), the influence of the electric field was negligible, and the droplet mixing was stable, as shown in Figure 4.20 (a). The left-hand side droplets, consisting of 50% glutaraldehyde in water, were dispensed with the speed of 0.83 m/s, and they are inclined at 30.25° with respect to the vertical axis. The other droplet, made of DMS-A11, has a velocity of 0.84 m/s and the angle 30.28°. When the distance between the dispensers and glass substrate is reduced to 6 mm, the charge on the substrate interact with those droplets and deflect their trajectory. This electrostatic interaction can even prevent the successful merging of the droplets, as visualized in Figure 4.20 (b). In this case, the silicone base droplets feature the same kinematic parameters, namely the velocity 0.84 m/s and angle 30.28°, while the drops of 50% glutaraldehyde in water exhibit a higher velocity, 0.93 m/s, and reduced angle, 28.72°. This effect can

be neutralized in two ways. The first approach is to connect the nozzles and the substrate electrically to the ground, to eliminate charging of the generated droplets and to secure stable mixing, as presented in Figure 4.20 (c). The second approach is to place a silicon wafer underneath the glass substrate and use it as a gate electrode to compensate for charges on the substrate. The effect of this approach is shown in Figure 4.20 (d). Both approaches were successful in eliminating the effect of electrostatic charging and produce stable droplet generation and merging.

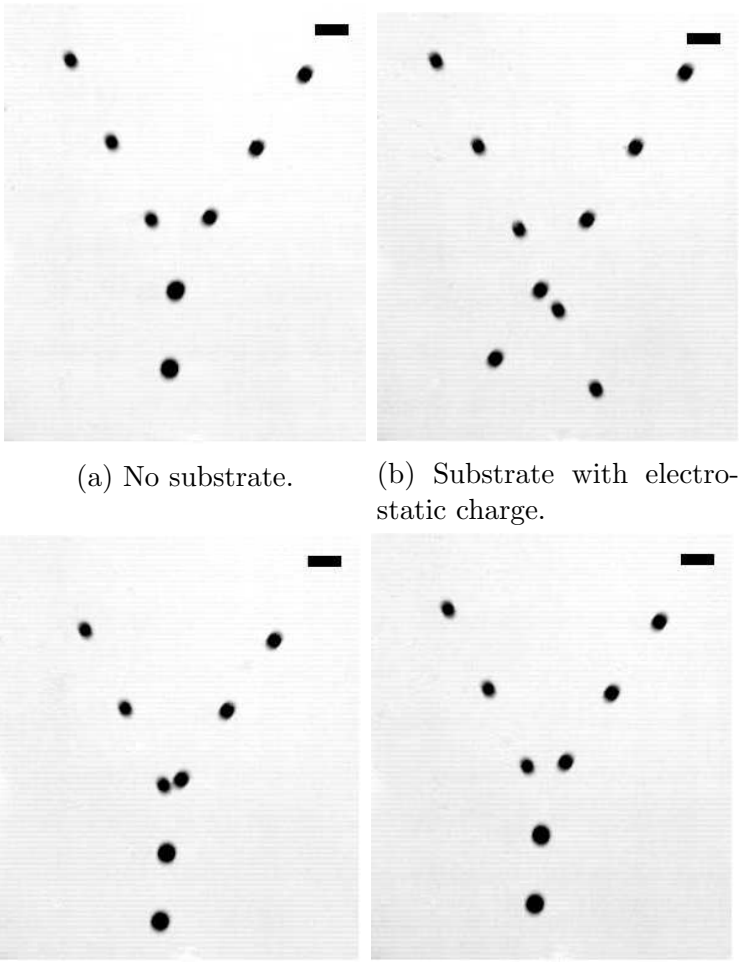

(a) No substrate.

(b) Substrate with electrostatic charge.

(c) Grounding the nozzle.

(d) Polarizing the print bed.

Figure 4.20: Impact of the electrostatic forces on the mixing process. Scale bar = 100 $\mu$m.

### 4.5.2 Impact of the substrate shape on the printing process

The inkjet printing approach belongs to the family of non-contact printing methods, and, therefore, an ejected droplet might be deposited even on a topographically complex surface. In the proposed method, once the electrostatic forces are neutralized by connecting the dispenser ejecting curing agent with the substrate, it was possible to stably deposit merged droplets on a flat substrate. However, due to the sensitivity of the free space mixing approaches, there was a concern that the mobile substrate with changing topography can cause air movement, which might eventually affect the droplet alignment and merging. To investigate if merged droplets could be printed on non-planar topography, the reactive inks, 50% glutaraldehyde in water and DMS-A11, were prepared, and the mixed material was deposited on a structured glass substrate with the size of 10 mm x 10 mm x 2.2 mm and step thickness of 1 mm, as visualized in Figure 4.21 (a). During the printing, two droplets collide with each other at the height of around 200 $\mu$m above the upper face, whereas the position of both the positioner and dispenser in the z direction remains unchanged. Moreover, the positioner moves with the velocity of 220 mm/min with respect to the x-axis. The experiment proves that the substrate with changing topography does not affect the stable mixing and deposition, which is visualized in Figure 4.21 (b). Clearly, one can also observe an advantage of inkjet printing over the extrusion methods. In the latter, a needle must precisely scan the profile of the substrate, which is very difficult when a material is being deposited on pre-fabricated objects.

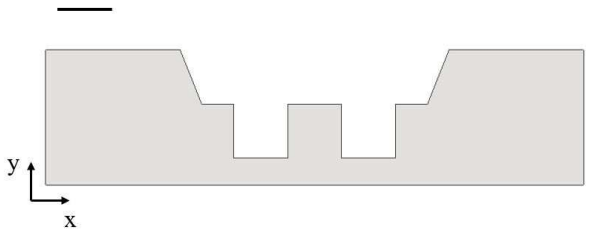


(a) Cross section of the surface with changing profile. Scale bar = 1 mm.

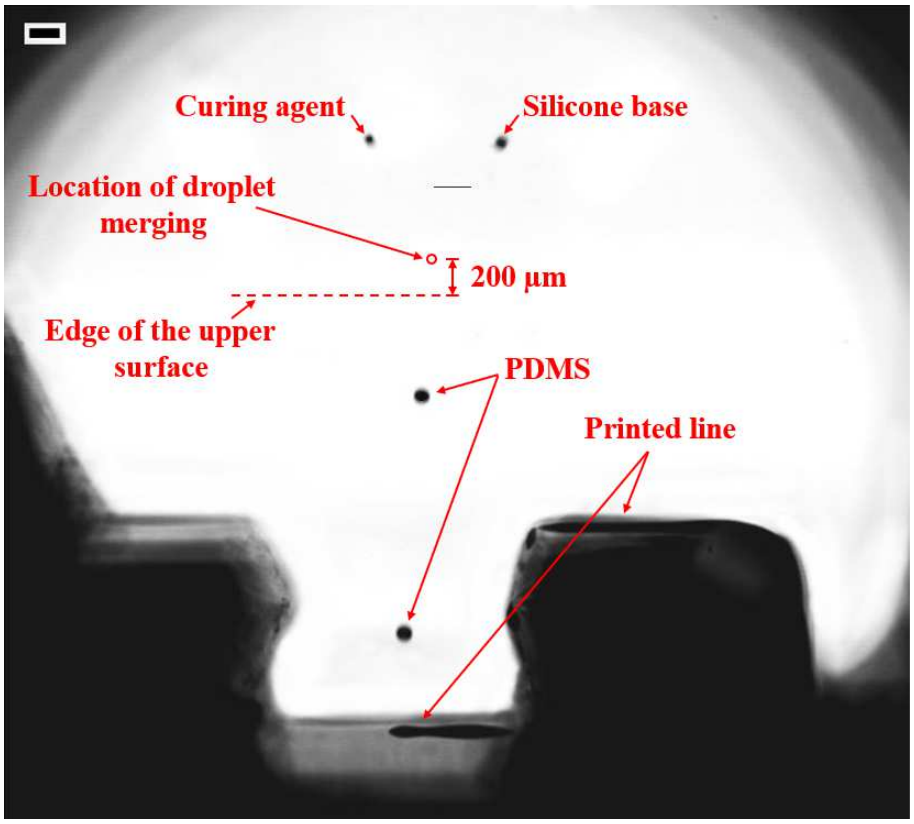


(b) Visualization of the droplet mixing and deposition on a nonuniform substrate. Scale bar = 100 $\mu$m.

Figure 4.21: Impact of a non-uniform surface on stable mixing.

## 4.6 Multiple start-stop cycles

An advantage of the DOD inkjet printing, compared to the continuous printing methods, is the possibility to eject a drop only when it is demanded, hence the droplet can be deposited with higher accuracy. Therefore, in the proposed method,

based on the free space mixing approach, it is very important to secure stable mixing of droplets every time when the system is being turned on, without further calibration. In the experiments, droplets consisting of DMS-A11 and 50% glutaraldehyde in water were ejected 5 cm above the substrate. In the calibration process, the trajectories and velocities of droplets were set so that the mixing process was stable. For this purpose, the following parameters of applied electrical impulses were used: the dwell time - 3$\mu$s, rise time - 7$\mu$s, fall time - 3$\mu$s, applied potential - 62 V, and frequency - 50 Hz for the curing agent, while for the silicone base the respective parameters were the following: 5$\mu$s, 10$\mu$s, 5$\mu$s, 92 V, and 50 Hz. The system was turned on for a few minutes, then turned off for thirty seconds, and turned on again. The behavior of droplets in a turn on/off/on cycle was observed using the (*Fastec Imaging TSHRMS*) high-speed camera, and the results were visualized in Figure 4.22.

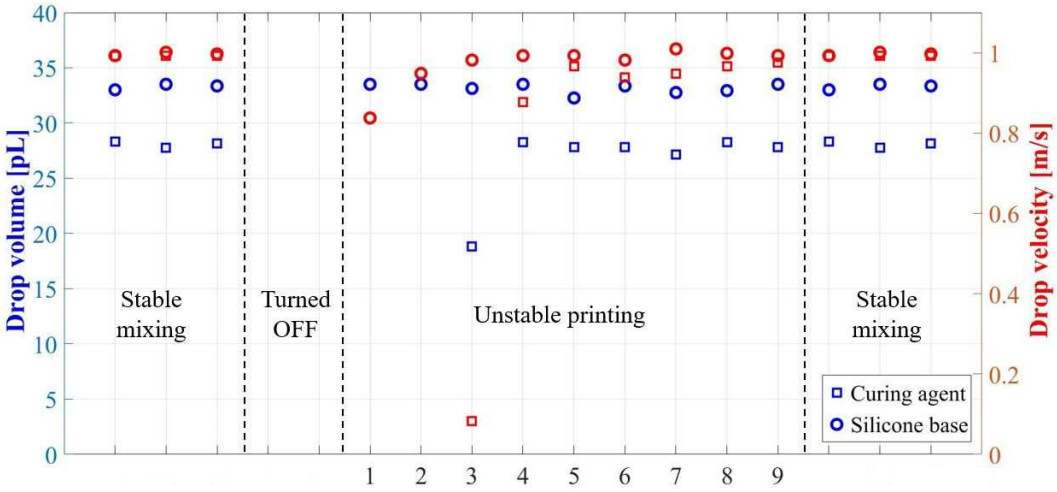


Figure 4.22: Stabilization of mixing process in multiple start-stop cycles.

At the beginning of this cycle, the droplets mix steadily, and they feature almost the same velocity, close to 1 m/s. However, their volumes differ, they equal to 33 pL and 28 pL in case of the silicone base and curing agent, respectively. Subsequently, the

droplet generation system is turned off for a few seconds and turned on again. In the second "on" stage of the cycle, one can distinguish two phases, namely unstable and stable mixing of droplets. In the former, the silicone base drops stabilize relatively quickly (their velocity remains constant), and their volume is equal approximately to 33 pL, with the standard deviation of 0.4 pL. Nevertheless, the velocity of the first three injected droplets increases to the value 1 m/s. In contrast, the droplet made of curing agent need more time to stabilize. It was observed that the ejection of the first drop is delayed, and it timely coincides with the generation of the third DMS-A11 droplet. Additionally, the first drop significantly differs from the others, because its trajectory is not aligned with the axis of the nozzle. One can deduce that the material contains small particles, which gather at the tip of the nozzle due to the sedimentation when the system was turned off. Therefore, the buildup pressure process was affected, and the ejection energy was sufficient to overcome the surface tension and push out the accumulated material only after the third electrical impulse was applied. Nonetheless, excluding the first drop (which has the volume 19 pL), all the droplets preserve the constant volume 28 pL, with the standard deviation of 0.4 pL, in the unstable stage. However, the velocity of subsequent droplets increases, for example, the velocity of the first drop equals to 0.08 m/s, 0.88 m/s in case of the second one, and, finally, 0.99 m/s in case of the last drop in this stage. Nevertheless, one can notice that the difference of velocities of two consecutive droplets decreases, which indicates that the printing process of the curing agent stabilizes. When the printing process of both substances is normalized, and both the droplets are ejected with similar velocities and the mixing of two droplets in free space occurs in a stable manner. The unstable printing stage is insignificantly short compared to the whole printing process, since it takes only 94ms. Additionally, the volume of the material that was lost in this phase is negligible, as its volume equals to 298.5 pL in case of

the DMS-A11, and 186 pL in case of the 50% glutaraldehyde in water. In conclusion, the merging process destabilizes within a short duration of time and start and stop operations do not consume significant time or material.

# 5 3D printing using printhead for reactive mixtures

The phenomena of generation and mixing of reactive droplets ejected using the proposed inkjet printing method with an integrated free space droplet module were carefully described in Chapter 4. In this section, however, special attention will be paid to the PDMS droplet deposition. Initially, the reaction between the deposited drop and different kinds of surfaces will be investigated. Subsequently, different examples of printed objects will be presented and extensively analyzed. They will include simple 1D and 2D parts, as well as more complex 3D structures, obtained using various printing parameters.

## 5.1 Droplets deposited on different surfaces

In many applications of the inkjet printing, the interaction between a liquid droplet and substrate is very important, as it determines the resolution of very first layer of the printed product. In a 3D printing approach, the deposited material transforms from a liquid to solid state. However, before the solidification, the deposited liquid needs to be stabilized. This step depends on many physical phenomena, which are driven by inertia forces, capillary forces, and to some extent, by gravity forces. At the beginning of the deposition, the drop movement is determined by its kinematic behavior which, after the collision with a substrate, changes into

impact-driven spreading and oscillation. Subsequently, this oscillation is damped by viscous forces. As the liquid spreads it loses momentum and the capillary forces become increasingly dominant and control the spreading until the equilibrium is achieved. Thus, the final diameter of the drop, which is called either the contact diameter ($d_{con}$) or footprint, depends on both its volume and the equilibrium contact angle between the material and substrate $\theta_{eqm}$. The relationship between the ejected droplet diameter ($d_0$) and the contact diameter can be determined using the following equation:

$$d_{con} = d_0 \sqrt[3]{\frac{8}{tan\frac{\theta_{eqm}}{2}}\left(3 + tan^2\frac{\theta_{eqm}}{2}\right)}[56]. \tag{5.1}$$

However, it was very difficult to measure the equilibrium contact angle of the combined reactive mixture, as the materials instantly react and solidify before contact angle measurements could be made. Furthermore, since one of the reactive components is hydrophilic and the other hydrophobic, it is difficult to deduce an approximate contact angle of the reactive droplet from these individual values. Instead the angle assumed by the crosslinked solid droplet was taken as the final contact angle of the liquid droplet before solidification and used as such.

In the experiments with 50% glutaraldehyde in water and DMS-A11, ten different surfaces were thoroughly analyzed. In the selection process, materials satisfying certain assumptions were considered. They had to be either commercially available, or easy to fabricate, and capable of maintaining constant physical parameters, such as contact angle, for a long time. The last characteristic is important to ensure the repeatability of the experiments. Therefore, various classes of materials, including polymers, metals and ceramics, were examined. During the experiments, the federate of the positioner was set to 1000 mm/min so that the generated droplets

will not overlap, thanks to which individually printed droplets could be visualized and compared against each other. The droplets were ejected with the frequency of 50 Hz, and the remaining parameters of applied impulses were set such that the velocity and diameter of both the reactive components were almost identical and equal to around 1 m/s and 40 $\mu$m, respectively. The droplets printed onto a polymeric substrate made of polyvinyl chloride (PVC), PDMS, and polytetrafluoroethylene (Teflon), are shown in Figure 5.1 (a-c), respectively. One can notice that the droplets deposited on PVC and PDMS have larger and more nonuniform shape compared to those deposited on Teflon. One can notice that the droplets printed onto a cleaned metallic surface, e.g. aluminium 5.1 (d) and cooper 5.1 (f), feature the largest spreading among all the results. However, the metallic surfaces, made of aluminium 5.1 (e) and cooper 5.1 (g) and coated by a hydrophobic nanostructure, prevent the droplets from spreading, and, therefore, the deposited droplets feature small contact diameters, similar to those on the Teflon substrate. Smaller sizes and more uniform shapes of droplets can be also observed on a surface made of silicon wafer 5.1 (h) or glass with hydrophobic nanocoating 5.1 (j). However, on a clean glass 5.1 (i), the deposited droplets slightly spread before the solidification. The measurements of the contact diameter are presented on the bar graph in Figure 5.2. Based on the first three bars, one can conclude that, among the polymer substrates, the contact diameter is the smallest for Teflon, 156.13 $\mu$m, while the standard deviation of all the measured values is very small, only 3.12 $\mu$m. The corresponding values obtained for PVC are 220.67 $\mu$m, 8.63 $\mu$m, whereas for PDMS 172.11 $\mu$m, 7.12 $\mu$m. However, it was noticed that between these materials and the dispenser an electrical field was created, which often disrupts the mixing process. Given the materials are nonconductive, it is very complicated to neutralize the charge on the entire surface. Therefore, it was decided to also consider conductive substrates, such

as those made of aluminium 5.1 (d) and cooper 5.1 (f), which do not exhibit such difficulties. After the measurement, it was observed that the droplets deposited on these substrates excessively spread, as they respectively achieved the contact diameter of 325.25 $\mu$m and 232.8 $\mu$m, while their measurement standard deviations are 9.52 $\mu$m and 11.97 $\mu$m. Therefore, their contact angle was increased by dipping them in a Drywired Textile Shield liquid, which generates a nanocoating on the surface making it both hydrophobic and oleophobic. Apparently, this treatment turns out to be effective, as shown in Figure 5.1 (e and g) for the aluminium and cooper, respectively. Based on the bar graph in 5.2, one can see that the contact diameter decreased in case of both the materials, and it equals to 134.97 $\mu$m and 148.05 $\mu$m for the coated aluminium and coated cooper, respectively. However, their standard deviations, 11.28 $\mu$m and 14.21 $\mu$m, is large compared to the previous results, because the metal surface is irregular and, therefore, it is not uniformly covered by the nonocoating. Another tested substrate is a silicon wafer, which is conductive, and also hydrophobic as long as its surface is not oxidized. According to the results presented in Figure 5.1 (h), one can read that the contact diameter on the silicon wafer is small, 131.05 $\mu$m, while the standard deviation is negligible, as it equals to 1.01 $\mu$m. Lastly, an experiment with a thin piece of glass (around 20 $\mu$m) was carried out. It is widely known that the glass is a nonconductive and hydrophilic material but, however, due to the uniformity of the surface, it is easy to evenly cover the surface by the nanocoating. Based on Figure 5.1 (i) and (j), one can compare the diameter of the droplets deposited on the clean and modified glass, respectively. In case of the former surface, the contact diameter is equal to 223.69 $\mu$m, and its standard deviation is around 8.9 $\mu$m. However, once it is coated by a hydrophobic and oleophobic liquid, the contact diameter is reduced to 123.58 $\mu$m, while the corresponding standard deviation is almost unnoticeable, 1.36 $\mu$m. Additionally, it

was noticed that, if the potential is applied to the conductor, e.g. silicon wafer, underneath it, on the upper surface of the glass substrate an equivalent charge is reflected. Thanks to this set up, the influence of electrostatic force was eliminated. In conclusion, one can say that the resolution of printed droplets is related to the hydrophobicity and oleophobicity of the substrate. If it is hydrophobic then contact diameter is smaller. In our experiments, the smallest diameter of droplets ejected from piezo dispensers with the orifice of 80 $\mu$m and mixed in free space, is equal to 123.58 $\mu$m.

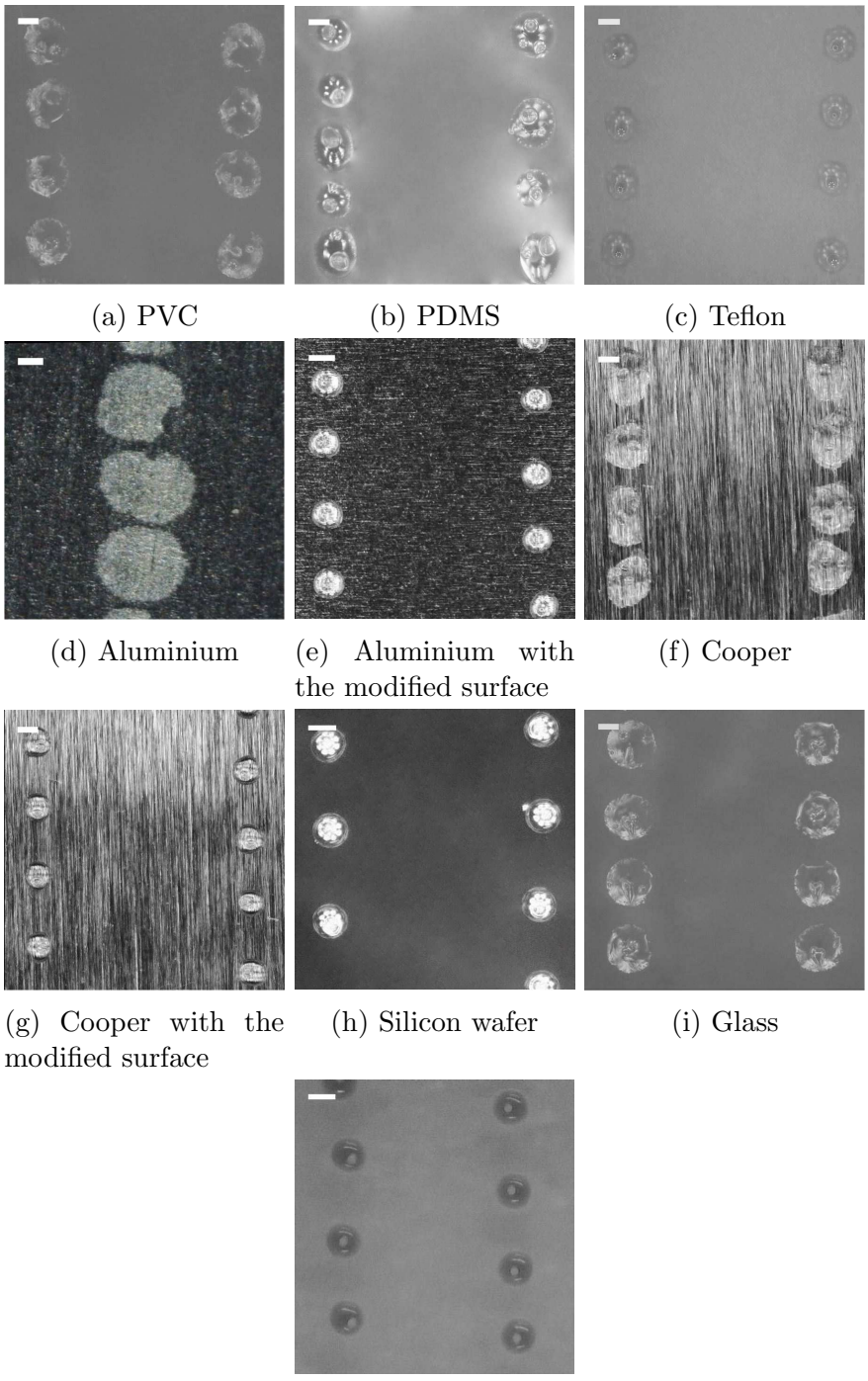

(a) PVC (b) PDMS (c) Teflon

(d) Aluminium (e) Aluminium with the modified surface (f) Cooper

(g) Cooper with the modified surface (h) Silicon wafer (i) Glass

(j) Glass with the modified surface

Figure 5.1: Impact of the surface on the droplet diameter. Scale bar = 100 $\mu$m.

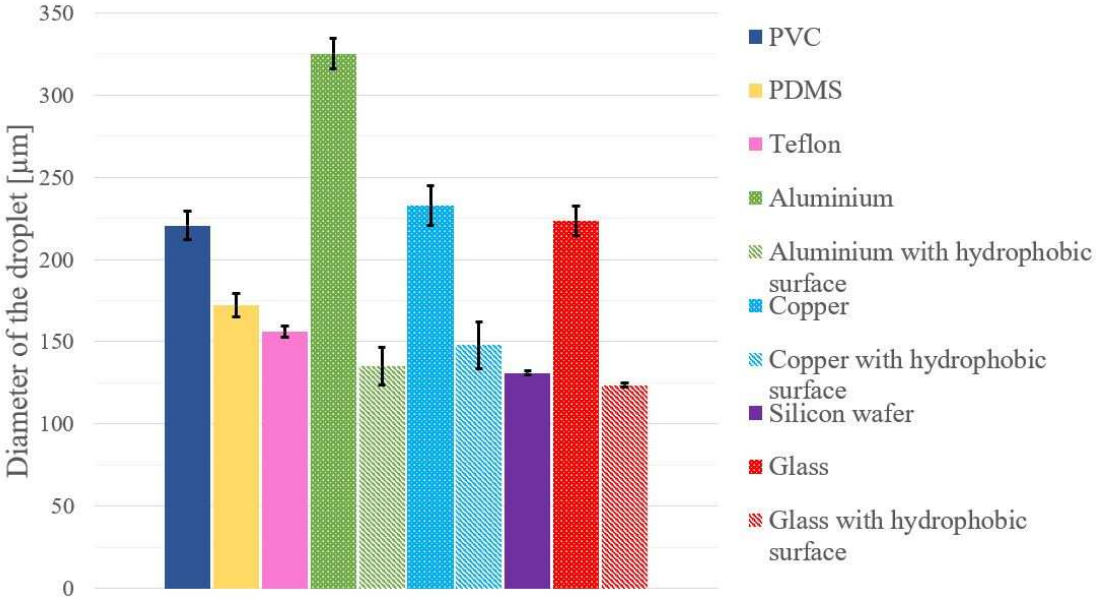


Figure 5.2: Diameter of the droplet on different surfaces.

The droplets made of solidified PDMS and printed on the modified glass substrate were precisely observed using the SEM microscope. Both their upper side and cross section are illustrated in Figure 5.3. Based on these pictures, one can infer that the glutaraldehyde and silicone base have mixed and diffused uniformly and, therefore, the resulting PDMS drop features a homogeneous structure. However, at the center of the drop, one can notice a cavity, which is empty space left by the evaporated water. The water is a substrate of the crosslinker and also by-product of the chemical reaction, and, since it does not mix with the silicone, it congregates at the center of the drop, and eventually evaporates. Due to the presence of the cavity, the printed object may feature porous structure, which will be described in the subsections below.

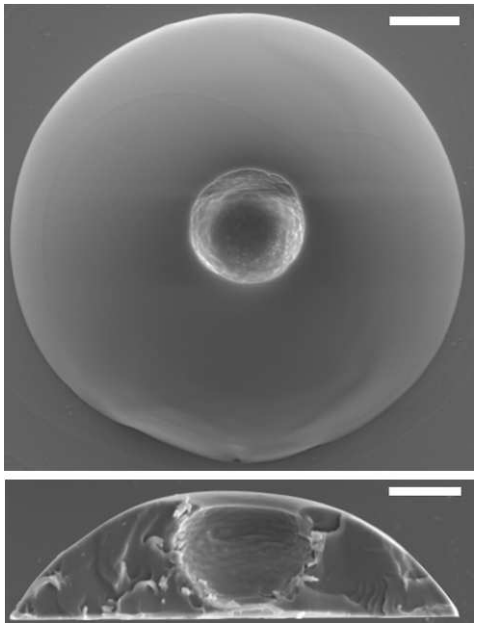

Figure 5.3: Top side and cross section of PDMS droplets. Scale bar = 20 $\mu$m.

## 5.2 Printing Stability - Straight Line

Inkjet printing is utilized in many applications, which require the dispensed droplets to overlap, in order to create a continuous line, 2D pattern, or 3D structure. Therefore, the capability of forming continuous lines is an essential building block in fabrication of more complex 3D structures. Droplets deposited in a linear fashion tend to merge and form a continuous line, provided the distance between the consecutive droplets is smaller than their contact diameter. After the deposition, the surface energy of the substrate affects the spreading behavior, which largely determines the width of the printed line. If the surface energy is low, the spreading phenomenon is suppressed, and, a high-resolution line can be printed. In this case, however, hydrodynamic instability can occur which might affect the shape of the deposited pattern. Additionally, the mechanism controlling the line formation depends on both the droplet spacing and time duration between consecutive droplet landings. If the

distance between the deposited drops is comparable to the contact diameter and the capillary spreading is slow, then the curvature of the liquid-air interface of the deposited droplet is larger on the side away from the previously printed line than it is on the side which connect to it. Therefore, the Laplace pressure gradient between two sides of the droplet pushes the liquid towards the line [56]. These phenomena can be visualized in Figure 5.4. The mixed PDMS droplet, with the diameter of 47 $\mu$m, is deposited within a distance of 47 $\mu$m from the previous one. One can observe that at the moment of contact with the glass substrate, the drop forms a spherical shape with the right-hand side of it connected to the previously printed line through a neck. The subsequent snapshots, which are taken every 0.1ms, show how the neck increases due to the pressure-driven flow, which eventually results in the movement of the liquid towards the area of lower pressure rather than allowing its spreading, until the equilibrium state is achieved.

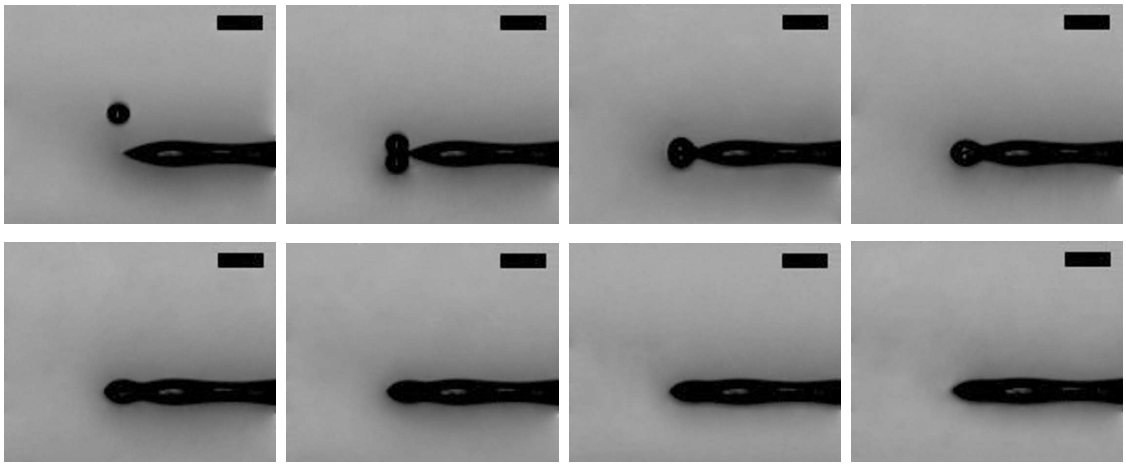

Figure 5.4: Formation of a continuous line. Scale bar = 100 $\mu$m.

### 5.2.1 Effect of droplets spacing on a continuous line formation

The line formation process is dependent upon three factors, namely the surface energy of the substrate, time, and distance between the consecutive droplets. In the

experiments, however, only the effect of droplets spacing was investigated. The coalescent PDMS droplets, which feature the diameter of 47 $\mu$m, were ejected onto a glass surface, and their deposition was recorded using the high-speed camera. Four different values of droplets spacing were considered, and their values varied from 0,2x to 1,4x of the contact diameter, which is equal to 123 $\mu$m. The distance between consecutive drops was regulated by choosing an appropriate feed rate of the positioner from the range between 80 mm/min and 500 mm/min, while the ejection frequency was set to a constant value, 50 Hz. The patterns of the deposited droplets are presented in Figure 5.5; these results demonstrate that reductions of the federate lead to the formation of different droplet configurations. If the value of droplet spacing is much larger than the contact diameter, for example 167 $\mu$m, the droplets cannot overlap and, in consequence, they form a sequence of equispaced dots, which is presented in Figure 5.5 (a). Subsequently, the feed rate of the positioner was decreased and, in Figure 5.5 (b), one can observe the behavior of the deposited material in the case when the droplet spacing is reduced to 81 $\mu$m. Because the gap is smaller than the contact diameter, 123 $\mu$m, a few deposited droplets coalesce and establish an unstable straight segment, in which the material is pushed to the right due to the presence of pressure gradient. When the newly formed droplet is not in contact with the preexisting one a new segment is created again. Another issue that hinders the formation of a continuous line are the vibrations of the positioner. Nevertheless, if the drop spacing is smaller, for example 73 $\mu$m, the deposited droplets form a continuous and smooth line, as presented in Figure 5.5 (c). However, if the gap between the droplets is further reduced, for instance to the value of 28 $\mu$m, the bulging instability occurs which is illustrated in Figure 5.5 (d). This phenomenon, which is similar to the one observed in the second scenario, leads to the formation of equispaced bulges along the printed liquid, without free space separating the line.

One can also observe this behavior if the time between the deposition of consecutive droplets is smaller than the time period for the droplet to contact the as printed line and equilibrate.

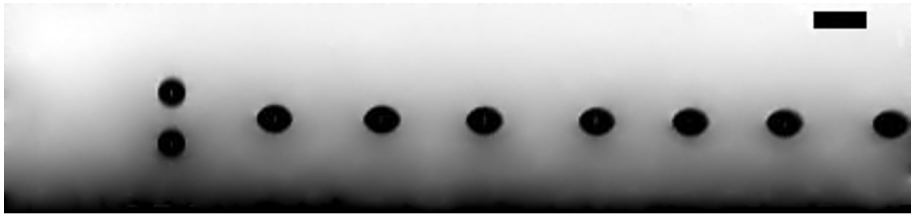

(a) Size of the gap between the deposited droplets = 167 $\mu$m.

(b) Size of the gap between the deposited droplets = 81 $\mu$m.

(c) Size of the gap between the deposited droplets = 73 $\mu$m.

(d) Size of the gap between the deposited droplets = 28 $\mu$m.

Figure 5.5: Printed line with different gaps between the deposited droplets on the glass surface. Scale bar = 100 $\mu$m.

From the previous experiments, it is known that the individual droplets feature the diameter of 123 $\mu$m, however, to accurately measure the width of the continuous and bulging lines, their top view pictures were required, as presented in Figure 5.6. Based on Figure 5.6 (a), one can notice the influence of vibrations introduced by

the movement of the XYZ positioner, which is reflected by non-uniform width of the line, whose average width is 120 $\mu$m. Additionally, one can observe that in most cases the water, which is both a substrate of the crosslinker and by-product of the polymerisation reaction, accumulates creating larger bubbles, which eventually evaporate and form cavities in a recurring fashion. In case of the line printed with droplet spacing of 28 $\mu$m, the formed shape features periodic pools of accumulated material that were connected by thin lines, as shown in Figure 5.6 (b). However, the accumulation spots of water are not periodic. The average width of the necking is equal to 119 $\mu$m, and maximum value achieves even 302 $\mu$m. One can infer that by choosing the optimal values of both the ejection frequency and feed rate of the positioner, the created pattern can be accurately controlled. Higher values of the federate allow the deposition of individual droplets, while a slow movement of the positioner guarantees the formation of a line with periodically accumulated spots of a material. In both cases, the distance between the deposited droplets, or the material spots, should be unchanged for the same federate. In the experiments, however, the influence of the vibration was significant, and, therefore, the gaps between droplets and spots slightly vary. This imperfection is also visible in case of the line consisting of irregular segments (Figure 5.5 (b)).

(a) Size of the gap between the deposited droplets = 73 $\mu$m.

(b) Size of the gap between the deposited droplets = 28 $\mu$m.

Figure 5.6: Top view of the printed line with different gaps between the deposited droplets. Scale bar = 100 $\mu$m.

### 5.2.2 Geometry of the lines depending on the number of layers

In the context of AM, a multiple-layer structure is more significant than a single-line object. Therefore, to present the capabilities of the proposed method, lines involving multiple layers were printed. Coalescent droplets of PDMS were deposited on the clean glass substrate, while the positioner was moved with the feed rate of 220 mm/min, and line with increasing number of layers from 2 - 10 were printed. The printed lines are illustrated in Figure 5.7, in which the lines are ordered from the top to the bottom with respect to the increasing number of layers.

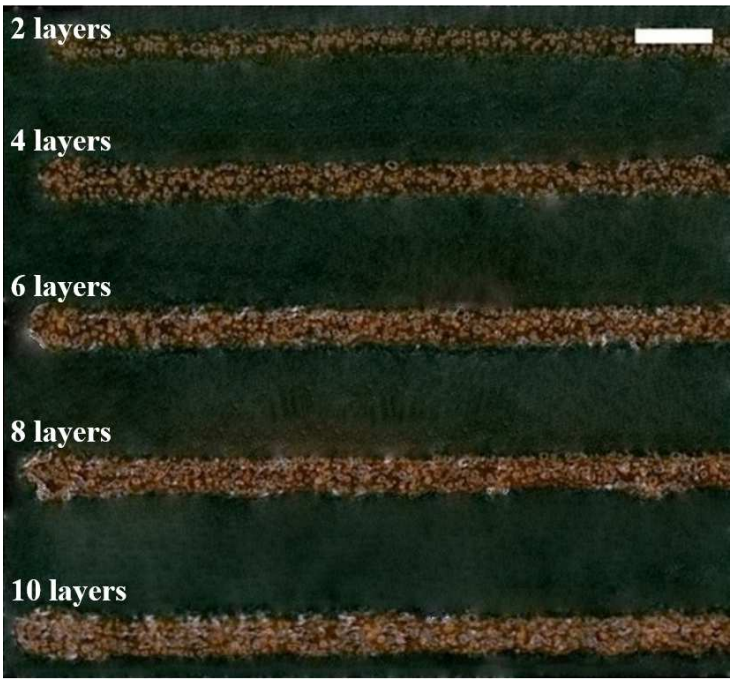


Figure 5.7: Printed lines involving different number of layers, 2,4,6,8 and 10. Scale bar = 1 mm.

The experiment was repeated five times, and each line width and thickness were measured three times, at the center and both ends, using a digital microscope (Keyence). The width was measured at the height midpoint of the line, and the results are shown on the bar plot illustrated in Figure 5.8 (a). It was observed that as the number of layers increases, the width also increases, from 281.58 $\mu$m, to 367.22 $\mu$m, 428.48 $\mu$m, 458.68 $\mu$m, and 492.5 $\mu$m, for two, four, six, eight, and ten layers, respectively. Based on this data, one can estimate that each layer is 16.1 $\mu$m wider with the respect to the previous one. In Figure 5.8 (b), one can notice that the lines thickness gradually grows achieving respectively 22.55 $\mu$m, 37.77 $\mu$m, 58.72 $\mu$m, 83.17 $\mu$m, and 108.78 $\mu$m. Additionally, based on the difference in thickness between the consecutive measurements, one can calculate that for the first four measurements, the gradient value linearly increases every 5 $\mu$m. However, the thickness of the ten-layer line is measured to be the same as the one of the eight-layer case. Therefore, one

can infer that at least eight layers are needed to eliminate the impact of the surface, and also that the growth in thickness in every two layers is between 24 $\mu$m and 27 $\mu$m. However, the above plots do not present the optimal resolution of the printed line, since the material was deposited on a clean glass substrate with the contact diameter of a single droplet around 224 $\mu$m. What is more, the nonuniformity in width and thickness was amplified by relatively strong vibrations of the positioner which hinders the accurate repetition of desired patterns.

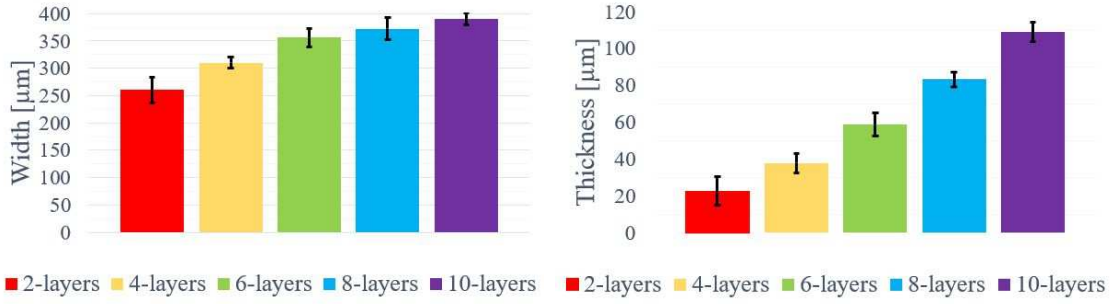


(a) (b)

Figure 5.8: Width (a) and thickness (b) depend on the number of layers.

## 5.3 Printing of 2D structures

Having demonstrated that lines can be stacked on top of one another, the next step is the printing of 2D surfaces. In general, the surface can be fabricated in two different modes, vertically and horizontally, and in both the cases different parameters controlling the movement of the positioner should be taken into account.

### 5.3.1 Vertically printed structure

#### 5.3.1.1 Effect of the positioner federate on the surface quality

In case of a structure printed vertically, two parameters are considered, namely the z-offset, which defines the distance between the upper boundary of the object and the point of mixing, as well as the feed rate of the positioner. Based on the previous experiment, it was calculated that the thickness of the line consisting of two layers achieves a value between 24 $\mu$m and 27 $\mu$m. However, during the calibration of the positioner, it was observed that the smallest offset along the z-axis cannot be lower than 39.2 $\mu$m. Therefore, it was decided that after the calibration of the first continuous layer on the substrate, the positioner will be lowered after each four layers by 58.8 $\mu$m. As of the positioner velocity, in the experiment, three different values of feed rate were tested, namely 200 mm/min, 220 mm/min, and 240 mm/min, while the ejection frequency was equal to 50 Hz in each experiment and the drop of PDMS features the diameter of 47 $\mu$m. After the fabrication of three different walls consisting of 200 layers, their central part was analyzed using the SEM. As seen Figure 5.9, all of the conditions produce surfaces that are undulating and not flat. They also consist of a number of pores indicating accumulated and subsequently evaporated water droplets. The undulation patterns are a result of the vibrations of the print bed introduced by the stepper motors, as well as the material accumulation when a too large volume is deposited on a small surface area. The 2D surface fabricated with the feed rate 200 mm/min, as illustrated in Figure 5.9 (a), features the largest and irregular undulating features. It is a consequence of the vibration and a small distance, 67 $\mu$m, between deposited droplets, as the material spreads sideways. Additionally, due to the large amount of deposited PDMS, there is a relatively large volume of water, which cumulates and creates many large cavities.

On the other hand, when the feed rate was changed to 240 mm/min the drop spacing increased to, 80 $\mu$m, as presented in Figure 5.9 (c). In this case, some irregular bulges appear, however, their dimension is smaller compared to the previous example. One can also observe that the total number of cavities is significant, however, they feature smaller sizes. Lastly, Figure 5.9 (b) shows a surface of the wall printed with the feed rate of 220 mm/min, which corresponds to the gap 73 $\mu$m between the droplets. Based on this picture, one can observe a more regular surface, on which the printed lines can be distinguished. Moreover, the quality of the printed structure is thought to have an impact on the amount of small empty spaces left by the evaporated water. Based on the above three pictures, one can infer that the droplet spacing 73 $\mu$m guarantees the best printing results out of the considered ones.

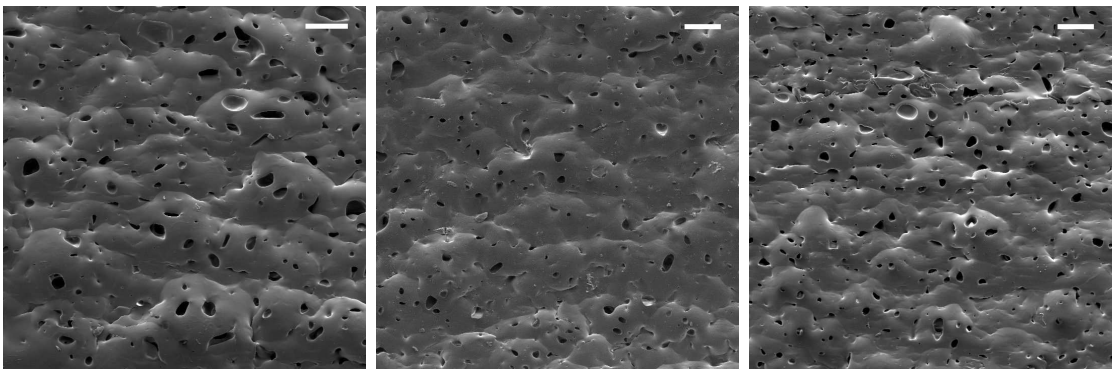

(a) 200 mm/min (b) 220 mm/min (c) 240 mm/min

Figure 5.9: SEM pictures of vertically printed structures with different feed rates: 200 mm/min (a), 220 mm/min (b), and 240 mm/min (c). Scale bar = 200 $\mu$m.

To better explain how the irregular structure is fabricated, a part of the printing process, during which the positioner moves towards the right, was recorded using a high-speed camera, and the resulting snapshots are presented in Figure 5.10. The mechanism controlling the deposited liquid behavior is identical to the one described in the Printed Line Stability subsection. Thus, one can observe in Figure 5.10 (a), that if the distance between consecutive droplets is small, for example 67 $\mu$m, the

drop deposited on the uncured polymer, due to the pressure-driven flow, is pushed to the right and it successively spreads out. The ejected droplets move around as long as the pressure gradient is sufficient to transport the droplet mass, otherwise the material starts to accumulate in another place, and, consequently a new bulge is created. However, during the deposition of the next layer, the material accumulates in the dimple leading to the formation of another bulge, due to the influence of the gravitational force. This mechanism explains the irregularities of the structure. Figure 5.10 (b) illustrates a uniform wall printed under optimal condition. If the drop spacing achieves the value of 73 $\mu$m, the pressure forces are balanced by contact forces, occurring between the liquid and solidified substrate, which, in consequence, leads to the creation of a uniform layer by the subsequent droplets. However, due to the vibration, the continuous line features a wavy pattern instead of a straight and flat structure. In Figure 5.10 (c), it has been shown that larger values of the droplet spacing, for instance 80 $\mu$m, lead to the repetitive aggregation of the material. Due to the influence of pressure forces, the deposited material is moved towards the earlier ejected liquid, but due to the relatively large gap between droplets, one can observe that sometimes the deposited droplets have no contact with the already transported material, and, therefore, another bulge is created. Moreover, similarly to the case when the gap is too small, the material that constitutes the consecutive layer is cumulated in a dimple, which ultimately leads to irregularities in shape.

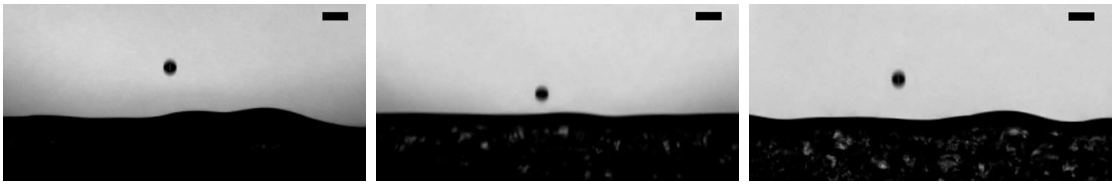

(a) 200 mm/min (b) 220 mm/min (c) 240 mm/min

Figure 5.10: High-speed camera pictures of vertically printed structures with different feed rates: 200 mm/min (a), 220 mm/min (b), and 240 mm/min (c). Scale bar = 100 $\mu$m.

Based on the results obtained with the SEM and high-speed camera, one can conclude that the correlation between the ejection frequency, droplet diameter and feed rate of the positioner determines the surface quality. If the federate is either too slow or too fast, an irregular surface with a wavy shape is created due to the cumulation of materials. However, the surface roughness can be minimized by the proper selection of the printing parameters. In the experiments, the irregularity of the shape was also caused by the vibration coming from the positioner, and, therefore, the printing of a smooth surface was hardly possible.

#### 5.3.1.2 High aspect ratio wall.

The above calibration allows to fabricate a high aspect ratio vertical structure under the optimal conditions (federate - 220 mm/min, ejection frequency - 50 Hz), as visualized in Figure 5.11 (a). The wall consisting of 1560 layers features the height around 17 mm, width 9.5 mm, and thickness 330 $\mu$m. Its aspect ratio (AR), therefore, is larger than 50. The thickness as well as the wavy pattern are precisely shown in the SEM image in Figure 5.11 (b). One can observe that the cross section of the surface exhibits a homogenous layer with some cavities created by evaporated water, which cumulates close to the edge. Despite the large value of AR, the thickness of the layer was uniform throughout its entire height indicating a very stable printing process. Therefore, one can infer that the reaction time is quick enough to successfully solidify and immobilize the object. Since a low frequency of 50 Hz was chosen to increase the time between the deposition of consecutive droplets and enable adequate time for reaction, the total printing time was about 40 minutes. This time can be reduced by increasing the frequency of printing.

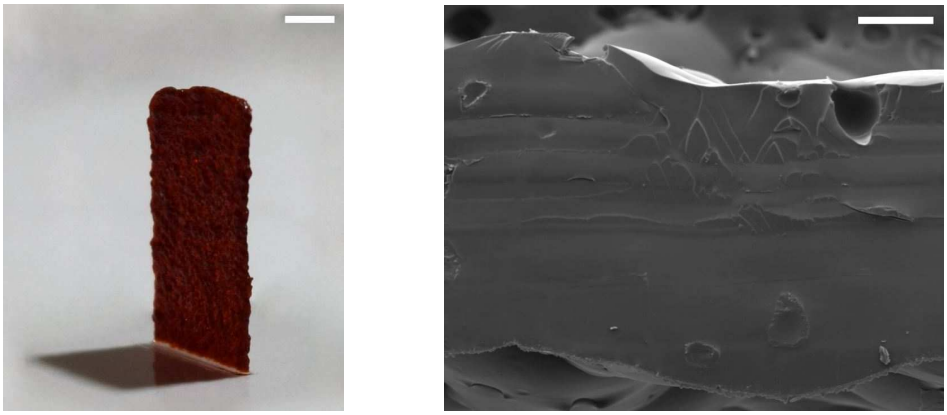

(a) Wall. Scale bar = 5 mm. (b) SEM image of a cross section of the wall. Scale bar = 100 $\mu$m.

Figure 5.11: High aspect ratio wall.

### 5.3.2 Horizontally printed structure

2D surfaces can also be printed horizontally. In this case, the critical printing parameters are: the distance between the stripes, which constitute the surface, and z-offset, whose value can be larger compared to the one for the single line printing. Therefore, two separate experiments were conducted to characterize and determine the optimal range of these parameters, to facilitate accurate reproduction of the design.

#### 5.3.2.1 2D filling structure

The effect of the line spacing was analyzed based on the structure consisting of one layer. In the experiments, the PDMS droplets were deposited on a clear glass substrate, while the feed rate of the positioner (220 mm/min) was coordinated with the frequency of ejection (50 Hz), to print a continuous line. In the experiments, three values of line spacing, 40 $\mu$m, 70 $\mu$m, and 100 $\mu$m, were tested. The printed surfaces were analyzed using the SEM, and the results are presented in Figure 5.12

(a-c). Based on the comparison of these pictures, one can observe the distance between the strip influences the surface porosity. In Figure 5.12 (a), which presents the surface fabricated with 40 $\mu$m line spacing, one can see relatively large cavities. This happens since the consecutive lines overlap, which means that the material accumulates, and, in addition, more water is deposited. As shown in Figure 5.3, the volume of water compared to the volume of PDMS is small, and, hence, the water moves in the direction of the open surface and evaporates. However, if the material accumulates, the transported bubbles meet, merge, and, consequently, form larger structures, which can move until the polymerization process is completed. This explains the large pores, that can be seen in Figure 5.12 (a), which take around 12.6% of the total area. To measure of the percentage content of pores, the ImageJ software was utilized. If the space between the lines is increased to 70 $\mu$m, the printed surface, illustrated in Figure 5.12 (b), has pores, which exhibit significantly smaller diameters and they occupy 9.4% of the total area. The further growth of the spacing, to 100 $\mu$m, enables the fabrication of a flat structure, as visualized in Figure 5.12 (c), in which the size and total number of pores remain almost unchanged (they constitute 9.3% of the total area) compared to the previous one.

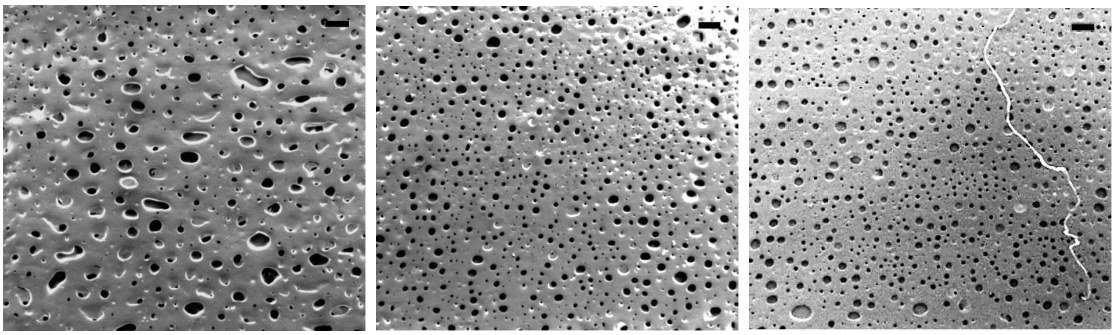

(a) 40 $\mu$m (b) 70 $\mu$m (c) 100 $\mu$m

Figure 5.12: SEM pictures of surfaces printed with different gaps between the lines (a) 40 $\mu$m, (b) 70 $\mu$m, and (c) 100 $\mu$m. Scale bar = 200 $\mu$m.

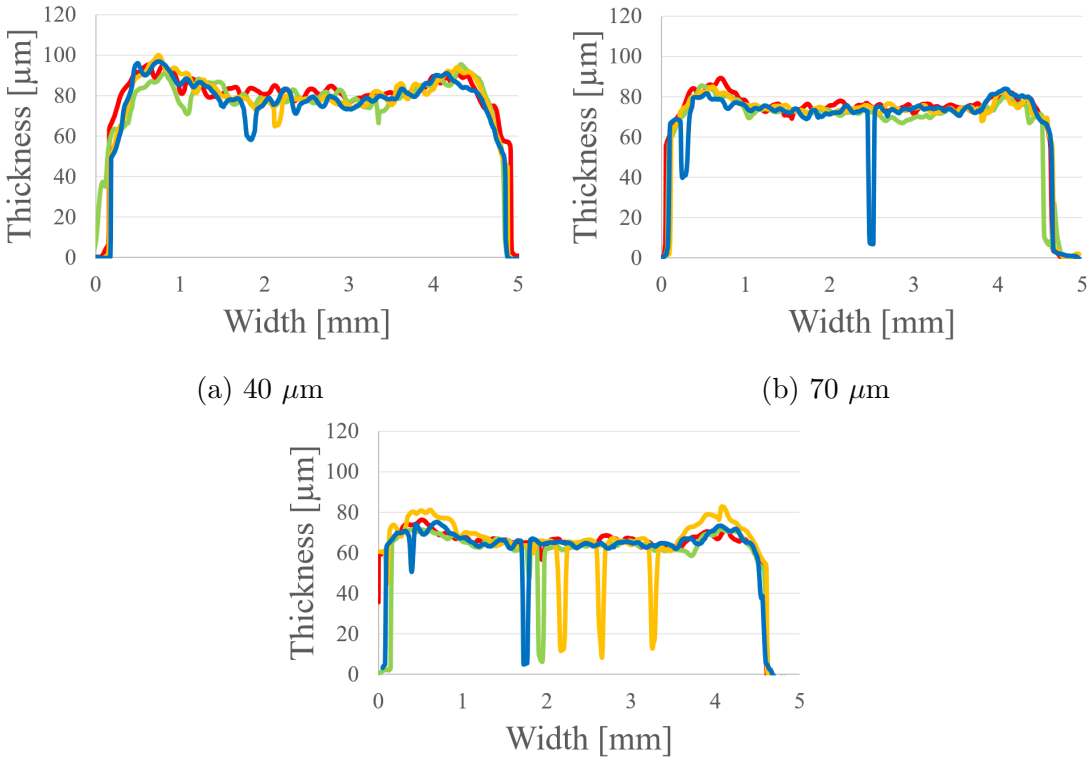


(a) 40 $\mu$m

(b) 70 $\mu$m

(c) 100 $\mu$m

Figure 5.13: Surface profiles printed with different line spacing: (a) 40 $\mu$m, (b) 70 $\mu$m, and (c) 100 $\mu$m.

Another analysis of the surface was carried out using the optical microscope, which enables a detailed inspection of the surface profile. The measurement was repeated fourteen times along different lines parallel to either the X-or Y-axis, however only four of them are presented in Figure 5.13, to make it more intelligible. Based on them, one can notice that once the line spacing decreases, the thickness of the surfaces also decreases, namely it is equal to 85 $\mu$m, 73 $\mu$m, and 65 $\mu$m if the distance between the lines is respectively 40 $\mu$m, 70 $\mu$m, and 100 $\mu$m. Additionally, the thickness of the surface presented in Figure 5.13 (a) varies by 22 $\mu$m, however the two remaining surfaces, in Figure 5.13 (b) and (c), feature the same thickness span, which is equal to 14 $\mu$m. Moreover, it was observed that in the surface printed with

the spacing of 100 $\mu$m there are many pores, whose depth is similar to the thickness of the surface, while in case of the spacing of 40 $\mu$m and 70 $\mu$m, the depth of pores is smaller, and it very rarely equals to the thickness of the surface.

In conclusion, based on these data, it was observed that the best results are achieved for the spacing 70 $\mu$m. Compared to the case with the spacing of 100 $\mu$m, the size of pores and their number is almost identical. In the former case, however, the pores are shallower and do not cover the entire thickness of a layer. The surface printed with the gap of 40 $\mu$m between the lines exhibits pores that cover a larger area, and the thickness variation is also larger.

#### 5.3.2.2 3D printing of a solid structure

The z-offset used for printing can also influence the topography of the printed layer. Therefore, the effect of z-offset on the printed surface was characterized by printing multiple layers one on top of another, and measuring their thickness values for comparison purposes.

Rectangular structures with the dimension of 9.55 mm by 3.63 mm were printed with back and forth line patterns along the X axis with the line spacing of 70 $\mu$m in Y direction. In this experiment, the positioner moved with the federate of 200 mm/min. The droplets were generated with the constant frequency 50 Hz, and the substrate was lowered by 58.8 $\mu$m every two printed layers. Different cuboids consisting of 2 - 10 layers were successfully printed, and an example of a two-layer structure is presented in Figure 5.14, which shows the top view in the left-hand side picture, and the thickness of the bent surface in the right one.

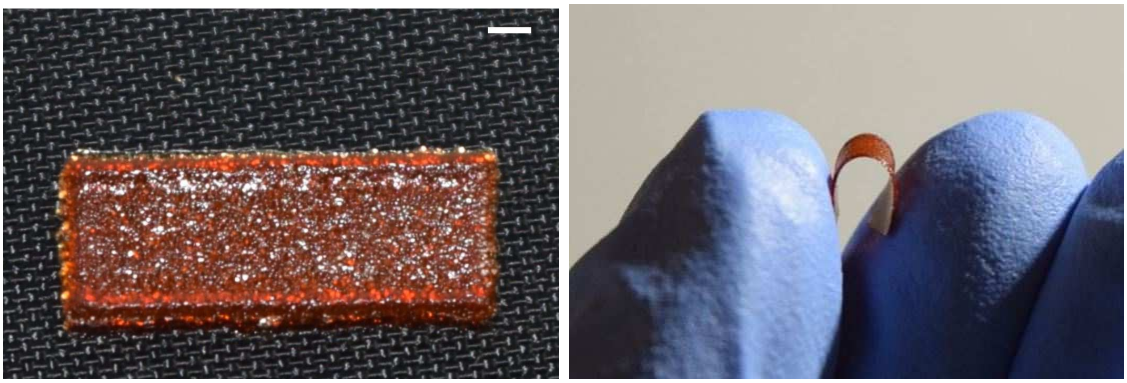

Figure 5.14: Two-layer surfaces. Scale bar = 1 mm.

The printed structure as presented in Figure 5.14 shows a uniform printed thickness at the central part with an elevated lip at the edges. Analysis of the printed structure using an optical microscope (Keyence), provides a quantification of the surface profile as shown in in Figure 5.15. Figures 5.15, show that the edges of the printed structure are elevated from the central part by 163 $\mu$m in the X direction and by 318 $\mu$m along the Y axis. It also shows that the thickness of the printed structure at the center was 570 $\mu$m. This corresponds to an average thickness of $\sim$ 57 $\mu$m /layer which is almost twice more than the observations of the printed line in section Geometry of the lines depending on the number of layers. The variation in thickness along the X direction, as shown in Figure 5.15 (a), can be explained based on the tool path. During the printing process, the droplets are constantly ejected with the same frequency, independent of the substrate position. During printing of a turn, the positioned slows down to a stop and turns around which results in a larger residence time at that location compared to those where the velocity of the positioned is constant. This results in deposition of 29% more material at the edges where the path turns as compared to the central part of the printed structure. Usually, to eliminate this problem, one can design rounded corners instead of square ones, thanks to which the motors will be working together in the same time without

stopping, and the corner will be printed with a constant feed rate. However, to follow the shape of the rounded corners, a high accuracy positioner adapted for an inkjet printing method is required. On the other hand, if the ejection and positioner systems are synchronized, one can overcome the problem by reducing the ejection frequency as it approaches the turn. Whereas the change of the profile along the X-axis can be logically explained, the shape variation along the Y direction, which is presented in Figure 5.15 (b), was surprising. It was expected that in this direction the surface will be flat, because the positioner should gradually move with the same velocity covering the same distance. However, the graph shows that around 56% more material is deposited at the surface boundaries, compared to the central part. Based on this observation, one can infer that the positioner movement in the Y direction is blocked at the beginning of the printing process of each layer. From the practical point of view, it means that the printing of the very first line of the surface is repeated a few times before the substrate changes the position along the Y-axis. Because the new printing of a new surface was initiated in the place where the previous one had been finished, the elevated edges are observed on both sides.

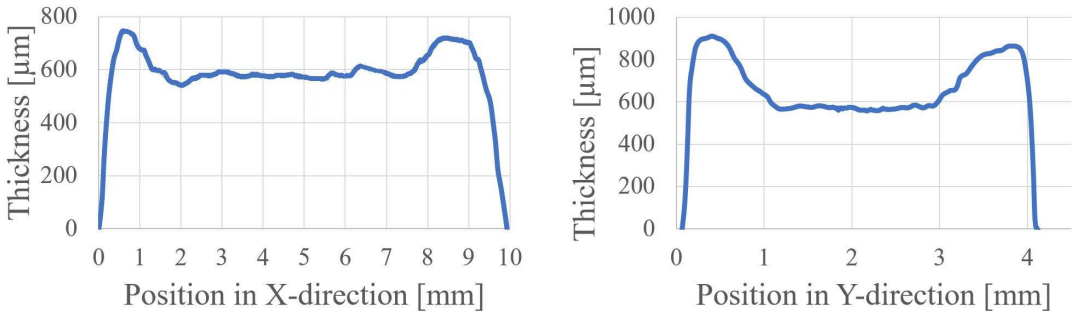


(a) (b)

Figure 5.15: Ten-layer surface profiles measured in X and Y directions.

Subsequently, in order to determine the difference in the structure thickness with respect to the number of layers, profile diagrams were prepared for other cuboid

structures, consisting of two, four, six, and eight layers. The thickness of each surface was measured in five different places and determined based on the value at the plateau part of the corresponding profile. Using the data from Figure 5.16 (a)), one can conclude that the thickness values are the following: 130.8 $\mu$m, 265.0 $\mu$m, 375.6 $\mu$m, 465.1 $\mu$m, 570.2 $\mu$m, for the two-, four-, six-, eight- and ten-layer surface, respectively. Moreover, one can notice that the difference between the consecutive graph bars, excluding the first one, is the same and equals to 101.7 $\mu$m. Hence, the thickness increases by 50.9 $\mu$m with the addition of each layer. For comparison purposes, more surfaces with both the same number of layers and printing parameters were fabricated using a different printing pattern. In this case, one layer was created by printing lines in the X direction, and next was formed with the printing lines along the Y axis, which resulted in a checked pattern. The measurement of the thickness was analogous to the previous one, and its results are illustrated in Figure 5.16 (b), which shows that the thickness of surfaces consisting of two, four, six, eight, and ten layers are the following: 165.88 $\mu$m, 329.94 $\mu$m, 439.02 $\mu$m, 562.63 $\mu$m, and 675.8 $\mu$m, respectively. In addition, based on these data, excluding the first bar, one can observe that the thickness value gradually increases by 57.5 $\mu$m per layer. One can notice that the surface printed using the checked pattern features a thickness larger by 18.5% compared to the corresponding surface created with the line pattern. Since the printing parameters were identical in both cases, the difference can only be attributed to the differences in the movement of the positioner, between these directions.

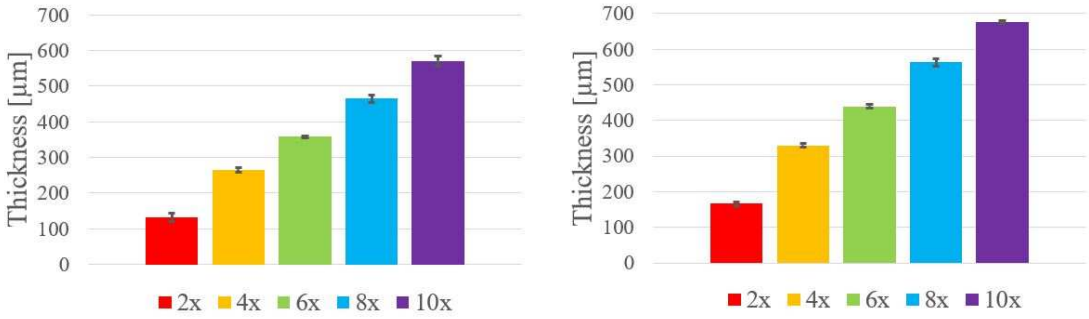


(a) Strip pattern.

(b) Checked pattern.

Figure 5.16: Relationship between the number of layers and the thickness of surface for different printing patterns.

## 5.4 Programmable shape

### 5.4.1 Hollow objects

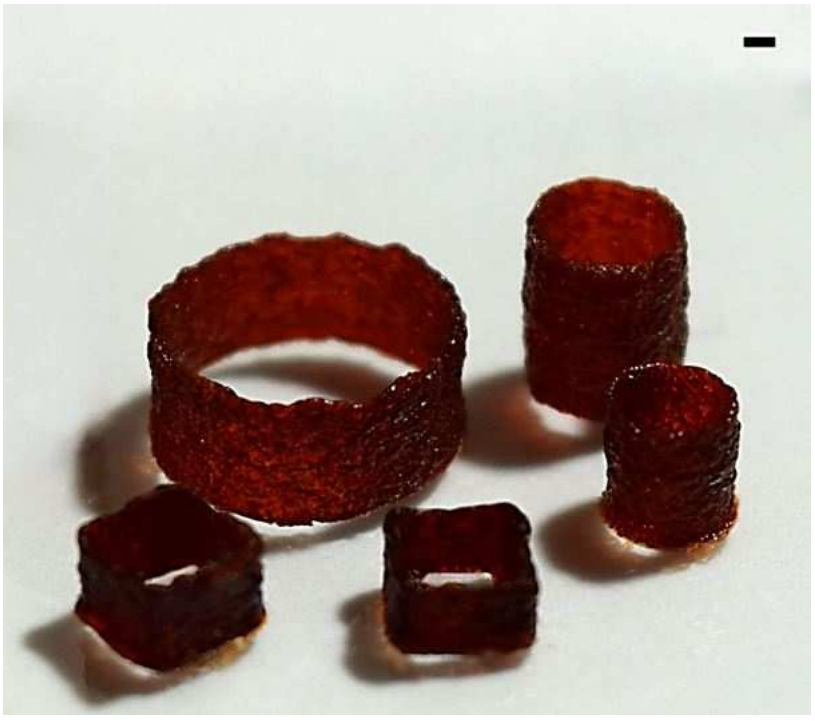

Figure 5.17: Examples of printed frames and tubes. Scale bar = 1 mm.

In order to present the capabilities of the new printer, and inspect the dimension accuracy of a more complicated printed object, hollow structures were printed. Proper calibration of the positioner and droplet generation system enables printing arbitrary shapes, such as frames or tubes, as presented in Figure 5.17.

#### 5.4.1.1 Frames

Using the Cartesian coordinates, the frames were designed with a circular corner to eliminate the cumulation of materials when the positioner changes its direction. A more precise description of the frame structures is based on the example included in Figure 5.18 (a). During the printing process, the positioner follows the path of a rectangular with the dimension 3.82 mm by 3.67 mm - with the velocity 220 mm/min, and reduces its altitude by 59 $\mu$m after every two layers. The printer was programmed to fabricate a frame consisting of 200 layers with the total height of 2.5 mm, and the droplets were generated with the frequency of 50 Hz. Based on the measurement, curried out using optical microscope, the frame features the size 4.14 mm and 4.0 mm in the X and Y direction, respectively, and it is 2.43 mm high. This compares favorably with the designed dimensions and results in error of 0.9%, 1.1%, and 2.8% along these directions. In order to obtain cross-sectional profile, the printed structure was frozen in liquid nitrogen, cut, and imaged using the SEM. The cross section, which is presented in Figure 5.18 (b), shows a uniform thickness of 290 $\mu$m throughout the entire height of the printed structure. Due to the slow movement of the positioner, low ejection frequency, and relatively large dimension of the object, the frame was printed within 7 minutes.

In conclusion, one can notice that the relative difference between the programmed and obtained dimensions is very small and reaches around 1% in XY plane and 3% along the Z-direction. Although the cross section structure is uneven due to the

printer vibrations, one can infer that the thickness is independent of the attitude of the object. It is an advantage of chemically-initiated silicones, whose reaction time is unchanged provided the temperature is constant, over thermally-initiated ones printed without a support material [41]. Moreover, the properties of the applied materials (50% glutaraldehyde in water and DMS-A11) allow to use a dispenser with an orifice diameter smaller than 80 $\mu$m, which could potentially improve the resolution of the printed structure further. In comparison, an alternative inkjet printing method for silicones utilized by the Wacker Chemie, has a resolution of $\sim$600 $\mu$m [42].

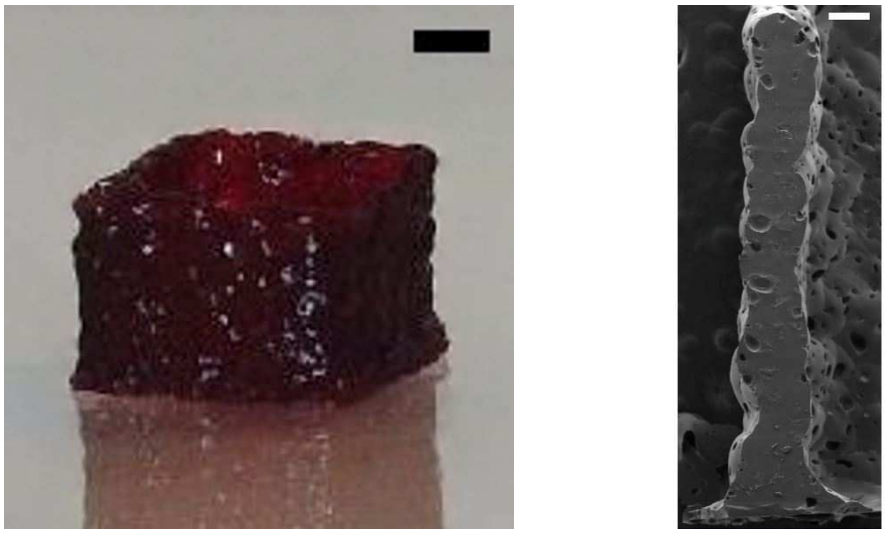

(a) Frame. Scale bar = 1 mm.

(b) Cross section of the frame. Scale bar = 200 $\mu$m.

Figure 5.18: Example of the frame and its cross section.

#### 5.4.1.2 Tubes

The fabrication of a tube requires further modifications of the positioner device. To facilitate printing of such structures, a gear motor was added to the existing setup. In this framework, the positioner controls the movement only in the Z direction, and

the substrate attached to the motor rotates with the constant angular velocity of 20 RPM. Due to the constant speed, the dimension and quality of the fabricated object were dependent on and regulated by both the frequency of the generated droplets and distance between the dispensers and central point of the motor. Figure 5.19 presents an example of a tube features the outer diameter of 4.55 mm, height of 5.2 mm and wall around 300 $\mu$m thick. Despite the influence of the positioner vibrations, one can notice only a subtle change in the tube structure, which maintains an almost uniform wall thickness, while its height is limited only by the printer capabilities. The dimension of the fabricated object directly affects the printing time, which, in this particular case, was equal to 34 minutes.

(a) Scale bar = 1 mm. (b) Scale bar = 300 $\mu$m.

Figure 5.19: Side and top views of the tube.

### 5.4.2 Filled objects

In order to further examine the accuracy of the designed printer, a filled object, such as cuboids illustrated in Figure 5.20, were fabricated Depending on the positioner movement, one can regulate the size of the printed object. In the experiments, however, the cuboid base remains constant, 2.87 mm and 2.71 mm with respect

to the X and Y axis, while its height changes. Applying the checked pattern, the printed objects consist of 40, 28, 24 and 12 layers, counting from the left in Figure 5.20. The feed rate of the positioner was equal to 220 mm/min, and it descents by 118 $\mu$m after every two layers. The z-offset is twice the value calculated for the multiple-layer structure printed using the checked pattern. Nevertheless, the earlier computation was performed for larger surfaces consisting of fewer layers. This time, due to the reduction of the surface size, the impact of the accumulation of materials is noticeable on the whole surface, not only at the edges, as it was the case in the previous experiments. The printing time is dependent on both the size of fabricated components and the positioner velocity. In this case, it took 43.5min, 30.5min, 26min and 13min for the structures consisting of 40, 28, 24 and 12 layers, respectively. Therefore, one can conclude that each layer is fabricated within 65s, hence the printing time is proportional to the number of layers.

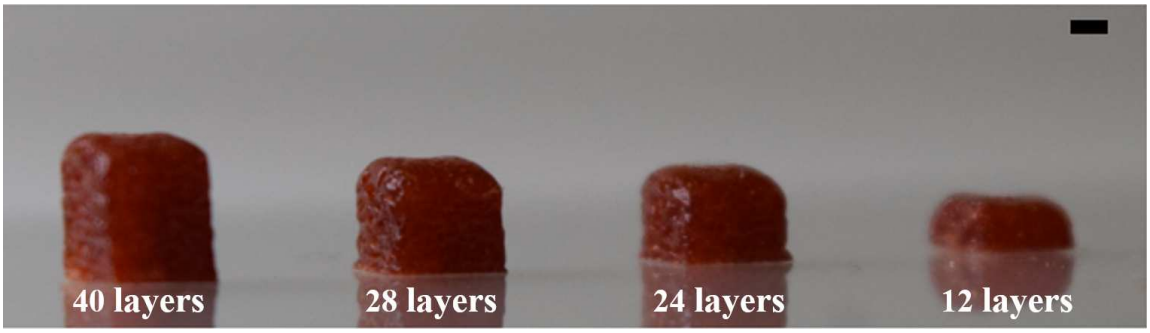


Figure 5.20: Cuboids with different heights. Scale bar = 1 mm.

The printing accuracy is meticulously analyzed for the 24-layer-cuboid, whose top view is illustrated in Figure 5.21 (a). Using the optical microscope, the object profile was scanned along the colorful virtual lines, and the resulting pictures are included in Figure 5.21 (b) and (c). Based on these results, one can observe that the vertical walls are straight, if viewed from the front (Figure 5.21 (b) and (c)), and slightly undulated from the top (Figure 5.21 (a)). Moreover, the upper surface does

not exhibit elevated edges but, it is not perfectly flat. In Figure 5.21 (b) and (c) one can notice that the cuboid edges are rounded with the radius around 0.5 mm. Additionally, based on the plots (b) and (c) in 5.21, the actual size of the object can be determined, thanks to which the average dimension measured along the X and Y-axis was computed to be 2.98 mm and 2.84 mm, respectively. Therefore, the actual size compared to the required dimension was respectively larger by 115 $\mu$m (4% of the programmed dimension) and 133 $\mu$m (4.9%). These deviations are acceptable, because the droplets slightly spread after the deposition, and, therefore, the printed object size is increased by this value. In addition, the left-hand side profile ends in Figure 5.21 (b), and the right-hand side ones in 5.21 (c), which respectively correspond to the right and bottom sides presented in Figure 5.21 (a), are slightly lowered with respect to the remaining edges. This is a consequence of both the positioner inaccuracy and the applied printing pattern. All the surfaces were printed starting from the top or left-hand side edges and, therefore, due to the inaccuracy of the device, some of the printed lines at the bottom and right-hand side walls were not deposited at the end of every cycle. To eliminate this problem, the printing process should be initiated from each side alternately.

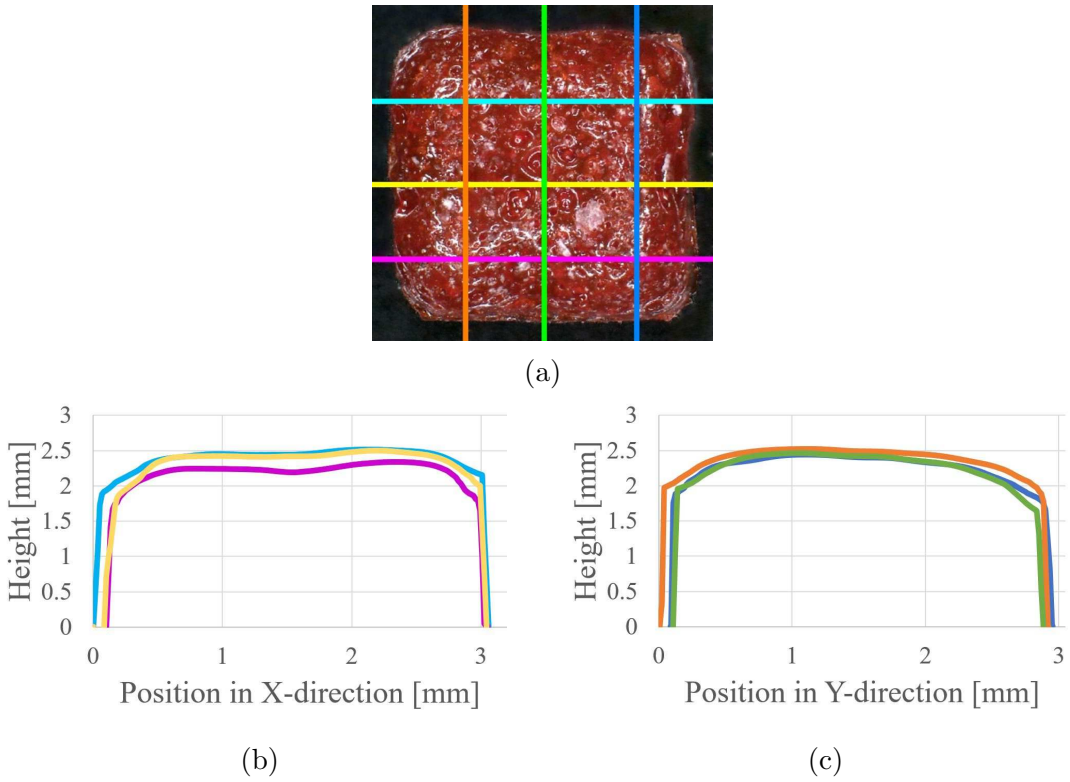


Figure 5.21: Top view of a 24-layers cuboid (a), and its profiles along the X (b) and Y (c) axis.

The cross section of the cuboid, presented in Figure 5.22, was also observed using the SEM. The picture, however, does not illustrate the entire cross section of the object but only a part of it as the printed object fractured when immersed in liquid nitrogen. This cross-sectional image shows that the two components of PDMS were mixed to a homogeneous material, however, is embedded with pores. These cavities are unevenly distributed on the whole volume, with the ones at the central part of the cross section feature smaller diameters compared to those located close to the edges, as shown in the two magnified pictures with red and green frames in Figure 5.22. This may be because there is enough time for the material in the central part to partially polymerize and spatially constrain water bubbles before another is printed. In the vicinity of the edge, however, the time between the depositions of

two consecutive layers is shorter, and, therefore, mobile water bubbles can merge and occupy a larger volume. Additionally, the evaporated water migrates in the direction of the open surface until the solidification is completed. Thus, due to the vapor movement, some bubbles can increase in size by merging with other ones, which can also explain the fact that the cavities close to the edge are bigger that those at the center. However, one can also observe four particularly large pores, whose size noticeably differs from the remaining ones. One of them is placed on the left-hand side, while the others are located at the upper-right corner. Since it is impossible to create that large cavities by merging a few small bubbles of water, one can infer that in those places two or three (this is a rough estimate based on the size of the pores) improperly mixed droplets were deposited. It may be considered as an error in the printing, but its impact on the whole structure is not significant.

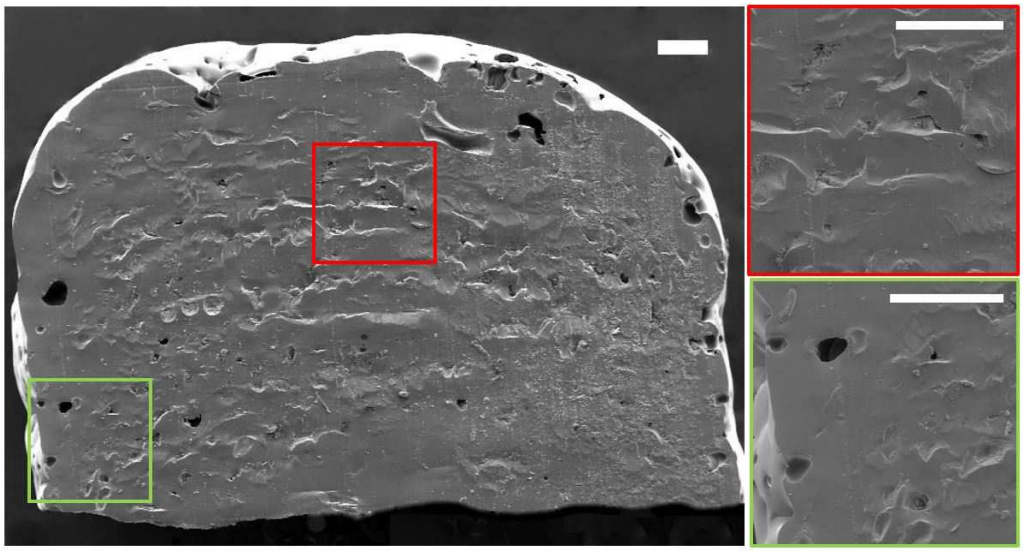

Figure 5.22: Cross section of the box. Scale bar = 200 $\mu$m.

## 5.5 Unsupported structure printing

The proposed inkjet printing method for highly reactive materials with an integrated free space droplet mixing module stands out form other 3D printing methods, be-

cause it can allow enables free-space printing. Thanks to this method, both components of PDMS are delivered in the same time and properly mixed, and, therefore, deposited droplet can quickly polymerize and attached to the substrate even if it is only tangentially connected to the already printed part. Additionally, due to the short reaction time, the mixed material solidifies very quickly and then becomes a substrate for the subsequent droplets. Hence, the partially overlapping droplets can form any 3D structure in free space without using any support materials.

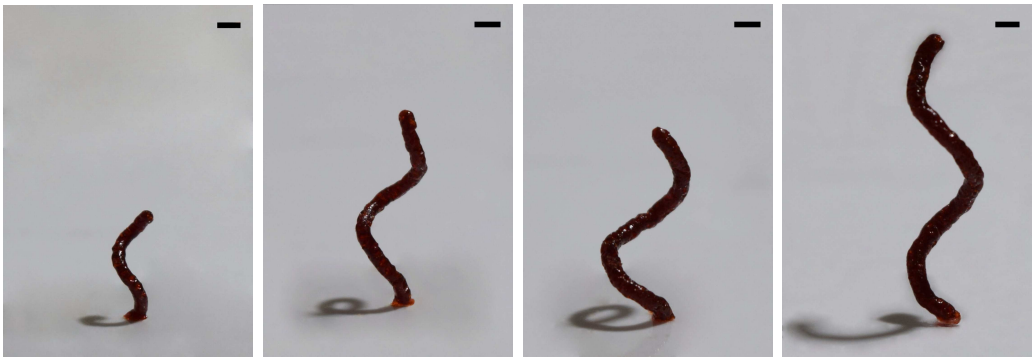

(a) (b) (c) (d)

Figure 5.23: Coil springs printed with different frequencies. Scale bar = 2 mm.

In order to demonstrate the capability of free space printing, micro coil spring objects were printed, as shown in Figure 5.23. During the fabrication process, the glass substrate attached to a gearmotor rotates with the constant speed 0.5 RPM, and its vertical position was regulated step wise, where the height was decreased by $\Delta$ = 1 mm after different time steps. Additionally, the frequency of droplet generation was also changed during the experiments. The coil springs, presented in Figure 5.23 (a-d), were printed with the following frequencies: 155 Hz, 200 Hz, 300 Hz, and 400 Hz, whereas $\Delta$Z decreased after the time intervals of 28s, 25s, 20s, and 15s, respectively. The changed parameters between consecutive printing cycles influence the coil diameter, which is respectively equal to 1.05 mm, 1.10 mm, 1.27 mm, and 1.43 mm. Based on these pictures, one can infer that it is possible to decrease

the spring stroke by reducing the time step. What is more, the diameter of the coil changes, depending on the chosen frequency. It was observed that the higher the frequency, the more material is deposited and the bigger the coil diameter. Additionally, the length of the coil springs is controlled by changing the printing time, whereas their diameters can be regulated by setting the distance between the droplet mixing point and center of the gearmotor.

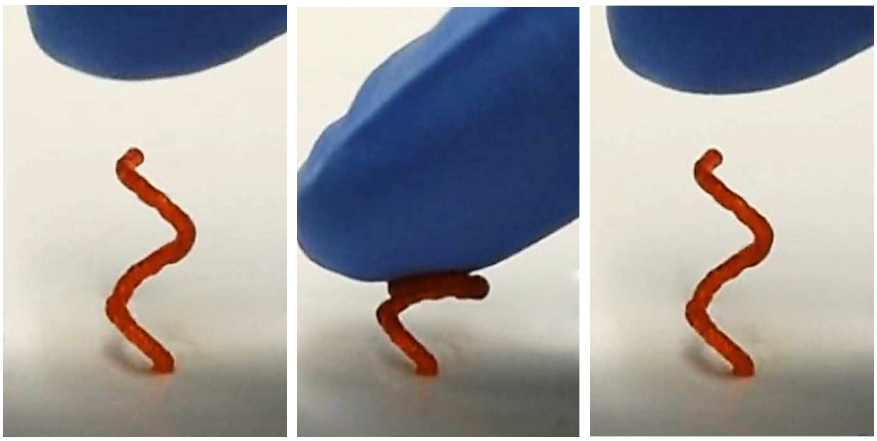

(a) (b) (c)

Figure 5.24: Coil spring subjected to a tensile force. Scale bar = 2 mm.

It is interesting how the printed coil springs behave when subjected to tensile forces. For this purpose, an experiment, utilizing the coil spring presented in Figure 5.23 (c), was carried out, and its results are illustrated in Figure 5.24 (a-c). In picture 5.24 (a) one can see an undeformed coil spring, which consists of one and half of a coil. Nevertheless, if a compressing force is vertically applied to the object, one coil decreases its stroke to the minimum, while the remaining half, which is connected to the glass substrate, stays unchanged, as shown in picture 5.24 (b). Subsequently, once the force is eliminated, the coil spring returns to its original shape, which in illustrated in picture 5.24 (c).

# 6 Conclusions and Future Work

## 6.1 Conclusions

Due to their physical and chemical properties, low viscous and highly reactive materials are difficult to use in 3D printing applications. The well-known methods of AM used for the fabrication of silicones, such as stereolithography and extrusion-based printing, are not adapted for this kind of materials. They crosslink through direct (dark) chemical reactions and require low volumes of separately deposited materials to ensure homogeneous mixing. In this context, the inkjet printing seems to be a suitable method, because it can eject small volumes of liquids from two (or more) separate dispensers leading to their polymerization outside the dispensing system. Therefore, low viscous and highly reactive materials require modifications of the traditional inkjet printing techniques, in order to improve the mixing of components and minimize the time between their ejection.

For this purpose, a new inkjet printing approach involving an integrated free space mixing module was proposed. Thanks to this modification, two reactive droplets are ejected simultaneously, merged and mixed together in free space outside the nozzles, and deposited as one drop in a patterned format on a substrate. To demonstrate the proposed method, an innovative 3D printer was also developed. Its crucial part is a printhead consisting of two dispensers and a holder, which is responsible for maintaining the dispenser in a stable position during the printing process, and also for adjusting the droplets trajectory to enable their stable mixing in free space. The printhead and other sub-assemblies, such as the XYZ positioner, material chambers, electronic control system for dispensers, or vacuum pressure system, were adapted to the proposed method, and assembled into the new 3D printer. Additionally, a

selection of proper silicone materials was carried out which enabled the calibration of the printer in the further work. Both families of the chosen materials, namely silicone bases and curing agents, were printed using a wide spectrum of impulse parameters, in order to find the suitable parameters guaranteeing stable droplet ejection. Subsequently, the droplet coalescence, mixing in free space, as well as deposition phenomena were carefully analyzed. Although the inkjet printing technique and droplet mixing phenomena are well-known and extensively described in literature, the combination of both has never been applied together. Therefore, due to the shortage of relevant data regarding 3D printing techniques for highly reactive materials, different factors, that can affect the stable mixing and droplet deposition during the printing process, were experimentally investigated and meticulously documented using a high-speed camera.

Thanks to this effort, the proposed method was shown to allow stable mixing and deposition of droplets for the period exceeding 4 hours. Additionally, the impact of electrostatic forces on the ejected materials, as well as a method suitable for eliminating these undesired effects, were presented. Moreover, the influence of substrate topology was carefully verified, and based on the experiments, it was demonstrated that the droplet mixing process is independent from the substrate shape. Furthermore, the behavior of droplets in multiple start-stop cycle was tested. It was shown that the instability period, occurring between the initiation of the droplets generation system and the stable mixing regime, features short duration - 94ms, and low material loss - less than 300 pL. Thus, the proposed method allows printing on demand. In the second part of the thesis, large emphasis was put on the characterization and optimization of the fabrication process which was carried out based on the experiments involving one-dimensional dots, two-dimensional structures, and three-dimensional printed objects. The main conclusions from the experimental studies

are essentially three-fold. First, both the PDMS components mix uniformly, which results in the formation of a homogeneous object. Second, the method facilitates the fabrication of any programmable shape, in particular, high aspect ratio (AR > 50) structures featuring the wall thickness of around 300 $\mu$m. Lastly, the new 3D printer is capable of printing in free space, which distinguishes the proposed method among all well-known AM techniques.

The contributions of this thesis involve the design and characterization of a novel 3D printer for highly reactive and low viscous silicones which can be applied also for other chemically reactive materials, e.g. epoxies. Additionally, this research has shown that droplet mixing modules can be integrated with a 3D printing method maintaining stable deposition process, which radically widens the capabilities of a traditional printer.

## 6.2 Future work

Despite of the significant capabilities of the proposed 3D printing method, the new printer as well as the materials can be further modified, in order to improve some important features.

**XYZ positioning device:** The biggest limitation of the current 3D printer is low quality of the XYZ positioning system that was used. It led to artifacts in the printing and significant loss of accuracy. Therefore, use of a more accurate positioner combined with a vibration damping system will ensure a very high quality of printing.

**Materials:** Although the materials used in the presented work meet the requirements in terms of viscosity, surface tension, and reaction time, the printed structures

were found to be porous. The presence of pores can be advantageous, since if they are distributed evenly, the printing of membranes or light-weight objects can be facilitated. On the other hand, the fabrication of a surface featuring good finish, i.e. with low roughness, might not be possible. Therefore, one should eliminate the water, which is both a substrate and by-product of the chemical reaction. In particular, one could prepare a new curing agent, which completely reacts with the silicone base without releasing any by-products, or, alternatively, one may consider replacing the water in the curing agent with a non-evaporating substance. Considering the fact that in many applications it is desirable to print transparent objects, one could utilize a formaldehyde instead of glutaraldehyde in water, which ensures not only transparency, but also better stretchability of the polymerized silicone. Although this material easily evaporates during the fabrication process and it is potentially dangerous to health, it could be handled in a well-ventilated environment. What is more, the proposed method can be utilized for other reactive materials, which do not belong to the family of silicones.

**Multi-material printing:** Multi-material printing techniques have recently become more popular in different applications. The system designed here can also be developed in this direction by an appropriate modification of the printhead. One possibility is to design a holder, featuring the shape of a circular frame, in which an arbitrary number of dispensing devices could be placed at its edge. The ejected droplets would be merged at the center of the circular frame. In this design, an arbitrary number of droplets made of various substances could be mixed together and deposited in one printing cycle.

**Printing objects with gradient properties:** Many objects of practical use require different mechanical properties in different regions. For instance, an ear

implant would have to be stiff in some regions and soft in others. The fabrication of such objects in one printing cycle can be performed in two different ways. Firstly, one could use an array of dispensers, that should be mounted in the holder described above, featuring orifices with different diameters. In this project, one of the largest commercially available dispensers, with the orifice 80 $\mu$m, was used, however there are smaller dispensers available,whose size can be as small as 5 $\mu$m. Therefore, by using dispensers of different sizes, one can regulate the volumetric ratio of two or more reactive PDMS components. If the amount of the curing agent is larger than the amount of the silicone base, the fabricated object will be stiffer, otherwise the resulting structure will be softer. As an alternative to the previous solution, one could consider a different approach, which is based on the regulation of the diameter of ejected droplets by controlling the actuating waveforms. It has been shown that by changing the trapezoidal (unipolar) waveform first to bipolar, then to M-shaped, and, finally, to W-shaped waveform, one can gradually reduce the droplet volume [64]. Therefore, the number of needed dispensers will be determined only by the number of utilized materials.

**Development of the free space printing:** In subsection Coil spring printed in free space, it was mentioned that the proposed method enables the free space printing of highly reactive materials. However, based on the description, one can expect that the synchronization of the droplet generation system with the positioning device would allow printing an arbitrary line in 3D space without any support materials, which means that the printing of complex structures would be possible. This printing approach is unique and distinguishes the presented method amongst all known AM techniques, therefore it is worth the further development.

# A Dispenser maintenance

Due to the small orifice and fragile glass tip of the dispensing device, its maintenance might be problematic. Any contamination exceeding 5 $\mu$m can affect its proper functioning or even completely clog the nozzle. Thus, a clean working environment as well as appropriate dispensing materials are strongly required.

The dispensers, tubing and syringes cannot be stored or used in a dusty area. Moreover, before they are used, they must be washed out of manufacturing contamination and dust. Therefore, a high wettability solvent, such as isopropyl alcohol, is applied and, subsequently, dried with pressurized air. Any liquid used in the cleaning process or during the experiment should be tested with both the tubing and tank to avoid their dissolution, and also to prevent the dissolved material from congregating at the glass tip. What is more, extra filtering of the liquids is strongly recommended to minimize the amount of particles smaller than 5 $\mu$m. At the end of the preliminary stage, the glass tip of the dispensing device should be carefully inspected using a microscope.

Once the experiments are finished, all the dispensers should be cleaned which requires a good amount of precise work. Firstly, the external surface, consisting of a metal part and glass tip, is carefully wiped. Secondly, the internal glass surface is flushed using a 2% water solution of $Micro-90$ solvent whose temperature does not exceed 50°C. The solvent is a powerful cleaner, consisting of chelants, ionic and non-ionic ingredients, which perfectly removes oil, wax, and particulates. The flushing and suction process should be repeated a few times if there are any residues at the tip. In the case of clogging, the device can be cleaned using a low power ultrasonic cleaner with 2% water solution of Micro-90. The ultrasounds should be applied at the glass tip no longer than one minute, otherwise the glass part can be broken. If

the dispenser remains clogged even after the cleaning procedure, the glass tip should be submerged in a 5% water solution of Micro-90 in the temperature below 80°C for 24 hours. One should ensure that the upper part of the dispenser is placed above the liquid surface because the solvent can damage the epoxy and nickel protection of the piezoelectric element. Subsequently, both the flushing and backflushing processes should be repeated to remove all the left-overs inside the dispenser. However, for some type of materials, such as polymerized PDMS, the chemical and ultrasonic approach is not efficient, therefore the cleaning process requires extra mechanical treatments. For example, low-scratch tube brushes are used to remove the material attached to the inner glass tube. Moreover, a metal wire with the diameter slightly smaller than the diameter of the orifice is pulled through the device to unclog the opening. Unfortunately, the mechanical method requires special attention since the glass tip is very fragile and the cleaning process is done using a microscope. Lastly, if the orifice does not contain any residuals, the dispensing device is washed out with DI water and isopropanol. At the end, the remaining liquid should be sucked out, while the dispensing device dried in an oven at 50°C for 30 minutes.

# B Properties of the Materials Utilized in Experiments

| **Substance name** | **Density** $\left[\frac{kg}{m^3}\right]$ | **Viscosity** $[mPa \cdot m]$ | **Surface tension** $\left[\frac{mN}{m}\right]$ | **pH [-]** |
|---|---|---|---|---|
| 38% wt. Glu. | 1060 | 19.86 | 89.33 | 4 |
| 30% wt. Glu. | 1110 | 18.40 | 81.78 | 4 |
| 30% wt. Glu.+100 ppm MeOH | 1072 | 4.25 | 63.30 | 3.5 |
| 30% wt. Glu.+50 ppm MeOH | 1083 | 4.62 | 67.97 | 3.5 |
| 30% wt. Glu.+20 ppm IPA | 1002 | 11.54 | 35.00 | 3.5 |
| 50% wt. Glu.+25 ppm IPA | 1082 | 19.38 | 42.65 | 5 |
| 50% wt. Glu.+25 ppm IPA (filtered) | 1074 | 9.06 | 42.43 | 5 |
| 50% wt. Glu.+10 ppm IPA | 1082 | 11.40 | 45.96 | 4 |
| 40% wt. Glu.+10 ppm IPA | 1090 | 11.24 | 47.77 | 4 |
| 50% wt. Glu.+5 ppm IPA | 1139 | 19.42 | 47.42 | 3.5 |
| 40% wt. Glu.+5 ppm IPA | 1085 | 12.83 | 46.95 | 3.5 |
| 50% wt. Glu.+5 ppm IPA+ surfactant | 1049 | 20.19 | 43.77 | 3.5 |
| 40% wt. Glu.+5 ppm IPA+ surfactant | 1078 | 13.82 | 44.98 | 3.5 |
| 50% wt. Glu. | 1198 | 17.42 | 65.32 | 4 |
| 40% wt. Glu. | 1072 | 7.87 | 64.96 | 4 |
| $A_1A_2D$ | 984 | 35.23 | 24.57 | 6 |
| $A_1A_2D_4$ | 978 | 14.43 | 26.30 | 10 |
| DMS-A11 | 939 | 17.86 | 41.55 | 10.5 |

Table B.1: Selected properties of the applied materials.

# C Refiling time

Every droplet dispensed from the nozzle leaves behind an empty space with the volume equal to the droplet bulk. To ensure stable and uniform droplet generation, this space must be filled, and moreover, the ink must return to its equilibrium state, and form a stable meniscus before the following ejection. This process is called the refilling and its duration constraints the maximum ejection frequency.

Inside the nozzle, the refilling phenomenon is driven by capillary forces. The capillary under pressure both pushes the ink until a flat meniscus at the rim of the nozzle is formed and balances other sources of pressure, coming from the mass of the material or external pressurized systems. The formula for the refiling time is as follows

$$T_{refill} = \sqrt{\frac{\rho L D_d^3}{3\sigma d}}[65], \tag{C.1}$$

where $d$ and $D_d$ denote the diameters of the orifice and droplet, respectively, $\rho$ and $\sigma$ are the density and surface tension of the ink, while $L$ is the transition position of the meniscus.

Nevertheless, the small dimension of the dispenser also requires the consideration of viscous effects. Thus, the balance of forces can be written as

$$\text{Net force} = \text{capillary force}(F_c) - \text{viscous force}(F_\nu) + \text{gravity force}(F_{g)}[66], \tag{C.2}$$

The capillary force in the circular tube is defined by the Young-Laplace equation,

$$F_c = 2\pi r \sigma cos(\Theta), \tag{C.3}$$

where $r$ is the radius of the nozzle, whereas $\Theta$ denotes the contact angle of the ink. The viscous force, based on the analytic result for the Hagen-Poiseuille flow, can be expressed as

$$F_\nu = 8\pi\eta v L_t, \tag{C.4}$$

where $\eta$, $v$, and $L_t$ denote the dynamic viscosity of the liquid, velocity of the ink, and the length of the tube, respectively. The last component in equation (C.2) is the gravity force, which affects the refilling process. Its significance is determined by the value of the Bond number, which is defined as

$$B_o = \frac{\rho g r^2}{\sigma}. \tag{C.5}$$

Because the Bond number is smaller than 1 in our case, the gravitational forces are small compared to the capillary forces and, therefore,one can neglect them in our analysis. Therefore, incorporating formulas (C.3) and (C.4), equation (C.2) can be rewritten to

$$\frac{d}{dt}\left(\rho\pi r^2 \frac{dL_t}{dt} L_t\right) = 2\pi r\sigma cos(\Theta) - 8\pi\eta v L_t, \tag{C.6}$$

where $t$ denotes the refilling time. One can solve equation (C.6) for $t$ assuming a complicated geometry of the nozzle, which is described in [66].

For both the silicone base ($A_1A_2D_4$) and curing agent (30% wt. glutaraldehyde in water solution with 20 ppm IPA), the refilling time was calculated twice, using two different equations, (C.1) and (C.6). The results obtained from the latter equation involve an error, because the exact geometry of the dispenser is not taken into account in our calculations. The refill time of the silicone base is equal to 0.187ms, if considering only the capillary forces, or 3.657ms, if including both the capillary and

viscosity forces in the calculation. Therefore, the maximum frequency should not exceed the threshold of 5347.6 Hz and 273.4 Hz, respectively. In case of the curing agent, the respective results are the following: 0.166ms, 2.95ms, and 6024.1 Hz, 339 Hz. By comparing these results, one can conclude that the viscous forces lead to a significant increase of the refilling time. Therefore,in the context of the refilling phenomenon, the viscous effects are critical in our analysis and cannot be ignored. The refiling time values computed considering both the capillary and viscosity forces are approximate, and, moreover, the corresponding values of the frequency are surprisingly low (around 300 Hz). Based on the results of experiments with $A_1A_2D_4$ and 30% wt. glutaraldehyde in water solution with 20 ppm IPA dispensed with different frequencies, as presented in Figure 4.16, one can conclude that both the diameter and velocity of the ejected drop do not change if the frequency is less than 500Hz. Hence, one can infer that the results calculated based on C.6 equation, which involves the impact of the capillary and viscosity forces are underestimated, due to the insufficient knowledge about the exact geometry of the dispenser. As was the case with the results involving residual oscillation, the high values of frequency, calculated using only capillary forces, were not verified in real conditions. However, one can expect that the maximum value of frequency allowing a proper refilling is lower, because the viscosity of the ink cannot be neglected when the small diameter of the nozzle is used.

# References

[1] A. Mata, A. J. Fleischman, S. Roy, "Characterization of Polydimethylsiloxane (PDMS) Properties for Biomedical Micro/Nanosystems.," *Biomedical Microdevices*, 7 (4), 281-293, 2005.

[2] P. C. Nicolson, J. Vogt, "Soft contact lens polymers: an evolution.," *Biomaterials*, 22 (24), 3273-3283, 2001.

[3] R. N. Palchesko, L. Zhang, Y. Sun, A. W. Feinberg, "Development of Polydimethylsiloxane Substrates with Tunable Elastic Modulus to Study Cell Mechanobiology in Muscle and Nerve.," *PLoS One*, 7, e51499, 2012.

[4] Y. Sun, Q. Jallerat,J. M. Szymanski, A. W. Feinberg, "Conformal nanopatterning of extracellular matrix proteins onto topographically complex surfaces.," *Nature Methods*, 12 (2), 134-136, 2015.

[5] J. C. McDonald, D. C. Duffy, J. R. Anderson, D. T. Chiu, et al, "Fabrication of microfluidic systems in poly(dimethylsiloxane).." *Electrophoresis*, 21 (1), 27-40, 2000.

[6] C. Liu, "Recent Developments in Polymer MEMS.," *Advanced Materials*, 19 (22), 3783-3790, 2007.

[7] K. K. Sadasivuni, D. Ponnamma, J. J. Cabibihan, M. AA. AlMa'adeed, "Electronic Applications of Polydimethylsiloxane and Its Composites.," Flexible and Stretchable Electronic Composites. Ed. D. Ponnamma et al, *Springer Series on Polymer and Composite Materials*, Springer, Cham., 2016.

[8] H. Takaoa, K. Miyamurab, H. Ebib, M. Ashikia, et al, "A MEMS microvalve with PDMS diaphragm and two-chamber configuration of thermo-pneumatic actuator

for integrated blood test system on silicon.," *Sensors and Actuators A: Physical*, 119 (2), 468-475, 2005.

[9] S. J. Choi, T. H. Kwon, H. Im, D. I. Moon, et al, "A polydimethylsiloxane (PDMS) sponge for the selective absorption of oil from water.," *ACS Applied Materials & Interfaces*, 3 (12), 4552-4556, 2011.

[10] A. L. Thangawng, S. S. Ruoff, M. A. Swartz, et al., "An ultra-thin PDMS membrane as a bio/micro-nano interface: fabrication and characterization.." *Biomedical Microdevices*, 9, 587-95, 2007.

[11] (2018, September 10), *Projected global additive manufacturing market size in 2015 and 2018 (in billion U.S. dollars)*, Retrieved from https://www.statista.com/statistics/284863/additive-manufacturing-projected-global-market-size/.

[12] W. E. King, A. T. Anderson, R. M. Ferencz, N. E. Hodge, et al, "Laser powder bed fusion additive manufacturing of metals; physics, computational, and materials challenges.," *Applied Physics Reviews*, 2 (4), 2015.

[13] A. Locker, (2018, July 20), *2018 Metal 3D Printer Guide - All About Metal 3D Printing*, Retrieved from https://all3dp.com/1/3d-metal-3d-printer-metal-3d-printing/.

[14] I. Gibson, D. Rosen, B. Stucker, *Additive Manufacturing Technologies*. New York, NY: Springer., 2015.

[15] D. I. Wimpenny, B. Bryden, I. R. Pashby, "Rapid laminated tooling.," *Journal of Materials Processing Technology*, 138 (1), 214-218, 2003.

[16] C. K. Chua, K. F. Leong, C.S. Lim, "Rapid Prototyping: Principles And Applications (3rd Edition)". Singapore: *World Scientific Publishing Co. Pte. Ltd*, 2010.

[17] T. J. Hinton, A. Hudson, K. Pusch, A. Lee, A. W. Feinberg, "3D Printing PDMS Elastomer in a Hydrophilic Support Bath via Freeform Reversible Embedding.," *ACS Biomaterials Science & Engineering*, 2 (10), 1781-1786, 2016.

[18] P. Rezai, W.I. Wu, P.R. Selvaganapathy, "Microfabrication of polymers for bioMEMS.", MEMS for Biomedical Applications, Ed. Bhansali S., Vasudev A., 2012, 3-45.

[19] K. Ikuta, K. Hirowatari, T. Ogata, "Ultra High Resolution Stereolithography for Three Dimensional Microfabrication.," Proceedings of the Fifth International Conference on Rapid Prototyping - 1994, University of Dayton, Dayton, Ohio, 1994.

[20] X. Zhang, "Dynamic mask projection stereo micro lithography." U.S. Patent 7088432B2, issued September 27, 2001.

[21] F. Burmeister, S. Steenhusen, R. Houbertz, et al. "Two-photon polymerization of inorganic-organic polymers for biomedical and microoptical applications.," Optically Induced Nanostructures: Biomedical and Technical Applications, Ed. K. Konig, A. Ostendorf, Berlin: De Gruyter; 2015. Chapter 5. Available from: https://www.ncbi.nlm.nih.gov/books/NBK321726/.

[22] Hull, C. (UVP, Inc.), "Apparatus for Production of Three-Dimensional Objects by Stereolithography." U.S. Patent 4575330, issued August 08, 1986.

[23] R. Felzmann, S. Gruber, G. Mitteramskogler, P. Tesavibul, "Lithography-Based Additive Manufacturing of Cellular Ceramic Structures.," *Advanced Engineering Materials*, 14 (12) , 1052-1058, 2012.

[24] J. R. Tumbleston, D. Shirvanyants, N. Ermoshkin, R. Janusziewicz, et al., "Continuous Liquid Interface Production of 3D Objects.," *Material Science*, 347 (6228), 1349-1352, 2015.

[25] E. LeProust, J. P. Pellois, P. Yu, H. Zhang, X. Gao, "Digital Light-Directed Synthesis. A Microarray Platform That Permits Rapid Reaction Optimization on a Combinatorial Basis.," *ACS Combinatorial Science*, 2 (4), 349-354, 2000.

[26] S. D. Hoath, "Fundamentals of Inkjet Printing: The Science of Inkjet and Droplets". John Wiley and Sons, 2015.

[27] Bournias-Varotsis, (2018), Introduction to Material Jetting 3D Printing, Retrieved from: https://www.3dhubs.com/knowledge-base/introduction-material-jetting-3d-printing#author

[28] W. Byeong, k. Kukjoo, l. Heejoo, k. So-Yun, et al, "High-Resolution Printing of 3D Structures Using an Electrohydrodynamic Inkjet with Multiple Functional Inks.," *Advanced Materials*, 27 (29), 4322-4328, 2015.

[29] B. Khoshnevis, "Automated Construction by Contour Crafting-Related Robotics and Information Technologies.," *Automation in Construction*, 13 (1), 5-19, 2004.

[30] P. Li, S. Mellor, J. Griffin, C. Waelde, et al, "Intellectual property and 3D printing: a case study on 3D chocolate printing." *Intellectual Property Law & Practice*, 9 (4), 322-332, 2014.

[31] J. Plott, A. Shih, "The extrusion-based additive manufacturing of moisture-cured silicone elastomer with minimal void for pneumatic actuators.," *Additive Manufacturing*, 17, 1-14, 2017.

[32] Fripp T., Frewer N., Green L. Method and apparatus for additive manufacturing, US 2016/0263827, 2016.

[33] J. O. Hardin, T. J. Ober, A. D. Valentine, J. A. Lewis, "Microfluidic Printheads for Multimaterial 3D Printing of Viscoelastic Inks.," *Advanced Materials*, 27, 3279-3284, 2015.

[34] F. Liravi, R. Darleux, E. Toyserkani, "Nozzle dispensing additive manufacturing of polysiloxane: dimensional control.," *International Journal of Rapid Manufacturing*, 5 (1), 20-43, 2015.

[35] K. Tian, J. Bae, S. E. Bakarich, C. Yang, et al, "3D Printing of Transparent and Conductive Heterogeneous Hydrogel-Elastomer Systems.," *Advanced Materials*, 29 (10), 2017.

[36] C. S. O'Bryan, T. Bhattacharjee, S. Hart, C. P. Kabb, et al, "Self-assembled micro-organogels for 3D printing silicone structures.," *Science Advances*, 3 (5), 2017.

[37] S. Rekstyte, M. Malinauskas, S. Juodkazis, "Three-dimensional laser micro-sculpturing of silicone: towards bio-compatible scaffolds .," *Optics Express*, 21 (14), 17028-17041, 2013.

[38] C. A. Coenjarts, C. K. Ober, "Two-Photon Three-Dimensional Microfabrication of Poly(Dimethylsiloxane) Elastomers.," *Chemistry of Materials*, 16 (26), 5556-5558, 2004,

[39] T. Femmer, A. J. C. Kuehne, M. Wessling, "Print your own membrane: direct rapid prototyping of polydimethylsiloxane.," *Lab Chip*, 14 (15), 2610, 2014.

[40] N. Bhattacharjee, C. Parra-Cabrera, Y. T. Kim, A. P. Kuo, A. Folch, "Desktop-Stereolithography 3D-Printing of a Poly(dimethylsiloxane)-Based Material with Sylgard-184 Properties.," *Advanced Materials*, 30 (22), 2018.

[41] C. Sturgess, J. Tuck, I. A. Ashcroft, R. D. Wildman, "3D reactive inkjet printing of polydimethylsiloxane.," *Journal of Materials Chemistry C*, 5, 9733, 2017

[42] Wacker Chemie. (2015). Q2 Interim Report January-June 2015, Germany, Retrieved from: https:// www.wacker.com/cms/media/en/documents/investor-relations/quarterly_report_1502.pdf.

[43] ACEO. "ACEO Open Print Lab: Experience 3D Printing with Silicones." YouTube, 7 Jun. 2017, https://www.youtube.com/watch?time_continue=3&v=x66yrACVXGE.

[44] T. Boland, X. Tao, B. J. Damon, B. Manle, et al, "Drop-on-demand printing of cells and materials for designer tissue constructs.," *Materials Science and Engineering C*, 27 (3), 372-376, 2007.

[45] Z.-C. Kao, Y.-H. Hung, Y.-C Liao, "Formation of conductive silver films via inkjet reaction system .," *Journal of Materials Chemistry*, 21, 18799-18803, 2011.

[46] K. Goto, "Effect of pH on Polymerization of Silicic Acid.," *The Journal of Physical Chemistry*, 60 (7), 1007-1008, 1956.

[47] R. S. Porter, J. F. Johnson, "Non-Newtonian Viscosity of Polymers.," *Journal of Applied Physics*, 32 (11), 2326, 1961.

[48] A. Daerr, A. Mogne, "Pendent Drop: An ImageJ Plugin to Measure the Surface Tension from an Image of a Pendent Drop.," *Journal of Open Research Software*, 4 (1), e3, 2016.

[49] D. Xu, V.Sanchez-Romaguera, S. Barbosa, W. Travis, et al, "Inkjet printing of polymer solutions and the role of chain entanglement .," *Journal of Materials Chemistry*, 17, 4902-4907, 2017.

[50] J. E. Fromm, "Numerical-calculation of the fluid-dynamics of drop-on-demand jets.," *IBM Journal of Research and Development*, 28 (3), 322-333, 1984.

[51] N. Reis, B. Derby, "Ink jet deposition of ceramic suspensions: modelling and experiments of droplet formation.," *Materials Development for Direct Write Technologies*, 624, 117-122, 2000.

[52] P.C. Duineveld, M.A. de KoK, M. Buechel, A. H. Sempel, et al, "Ink-jet printing of polymer light-emitting devices.," *Proceeding Conferences Organic Light Emitting Materials and Devices*, 4464, 59-67, 2001.

[53] C. D. Stow, M. G. Hadfield, "An experimental investigation of fluid-flow resulting from the impact of a water drop with an unyielding dry surface.," *Proceeding of the Royal Society of London A*, 373 (1755), 419-441, 1981.

[54] R. Bhola, S. Chandra, "Parameters controlling solidification of molten wax droplets falling on a solid surface.," *Journal of Materials Science*, 34 (19), 4883-4894, 1999.

[55] C. Mundo, M. Sommerfield, C. Tropea, "Droplet-wall collisions: Experimental studies of the deformation and breakup process.," *International Journal of Multiphase Flow*, 21 (2), 151-173, 1995.

[56] B. Derby, "Inkjet Printing of Functional and Structural Materials: Fluid Property Requirements, Feature Stability, and Resolution.," *Annual Review of Materials Research*, 40, 395-414, 2010.

[57] D. B. Bogy, F. E. Talke, "Experimental and Theoretical Study of Wave Propagation Phenomena in Drop-on-Demand Ink Jet Devices.," *IBM Journal of Research and Development*, 28 (3), 1984.

[58] H. Dong, W. W. Carr, J. F. Morris, "An experimental study of drop-on-demand drop formation.," *Physics of Fluids*, 18, 072102, 2006.

[59] H. J. Shore, G. M. Harrison, "The effect of added polymers on the formation of drops ejected from a nozzle.," *Physics of Fluids*, 17, 033104, 2005.

[60] D. Cibis, k. Kruger, "Optimization of a DoD Print Head Signal for the Ink-Jetting of Conductive Circuits.," *International Conference on Non-Impact Printing*, NIP24, Pittsburgh, USA, 125-128, 2008.

[61] Hutchings, I. M., Martin G. D., Inkjet Technology for Digital Fabrication. John Wiley and Sons: 2013.

[62] Abbott C. E., Review of Geophysics and Space Physics, 15 (3), 363-374, (1977).

[63] M. Orme, "Experiments on Droplet Collisions, Bounce, Coalescence and Disruption.," *Progress in Energy and Combustion Science*, 23, 65-79, 1997.

[64] H. Y. Gan, X. Shan, T. Eriksson, B. K. Lok, Y. C. Lam, "Reduction of droplet volume by controlling actuating waveforms in inkjet printing for micro-pattern formation.," *Journal of Micromechanics and Microengineering*, 19, 055010, 2009.

[65] R. D. Carnaham, S. L. Hou, "Ink Jet Technology.," *IEEE Transitions on Industry Application*, 1A-13 (1), 1977.

[66] K. S. Moon, J. H. Choi, et al, " A new method for analysing the refill process and fabrication of a piezoelectric inkjet printing head for LCD color filter manufacturing.," *Journal of Micromechanics and Microengineering*, 18 125011, 2008.